Investigation of Photonic Crystal Components for Integrated Devices in the Visible

Masterarbeit

zur Erlangung des akademischen Grades
Master of Science (M. Sc.)
im Fach Physik

eingereicht an der
Mathematisch-Naturwissenschaftlichen Fakultät I
Institut für Physik
Humboldt-Universität zu Berlin

von
B. Sc. Carlo Barth
geboren am 08.10.1987 in Dessau

Betreuung:

1. Prof. Dr. Oliver Benson
2. Prof. Dr. Kurt Busch

Abstract

Integrated photonic devices operating with visible light are potential solutions for future ultra-fast and resource-friendly photonic computers. A promising candidate for the dielectric environment in which such networks could be implemented are photonic crystal slabs – photonic bandgap materials which are easy to produce and offer a multitude of applications based on defects for light guidance, confinement or filtering. However, since light sources and detectors are typically not integrated into such dielectric structures, a vertical scatterer is needed for in- and outcoupling of light.

Consequently, the intention of this thesis is to investigate the tunability, directivity and efficiency of a specific double-ring grating coupler for out-of-plane scattering from photonic crystal waveguides. To this end, numerical and experimental methods have been utilized to study the involved components such as the L3-cavity, the W1-waveguide and mainly the grating coupler itself. In computer simulations, frequency domain eigensolver techniques and the finite-difference time-domain method have been used to find an experimentally accessible chip design and to produce numeric reference data for transmissions and efficiencies. Experimentally, transmission measurements and a back-focal plane analysis were applied to study the components in detail.

With the help of these techniques, an in-gap coupling efficiency on the order of 20 % was achieved – numerically even up to 40 % seem possible if optimizations are considered. The tunability of the grating was demonstrated in view of its directivity, exhibiting advantages over an omitted coupling structure of roughly 30 %. Hence, it was shown that the coupling structure indeed offers the desired functionality, although improvements are necessary on the road towards single-photon devices. Moreover, an in-depth analysis of the W1-waveguide's mode structure, propagation loss and absolute transmission was carried out to gain further insight into the physical effects of the system. The results – and especially the developed numerical methods – contribute to the development of efficient vertical coupler structures for photonic crystal structures.

Contents

1 Introduction

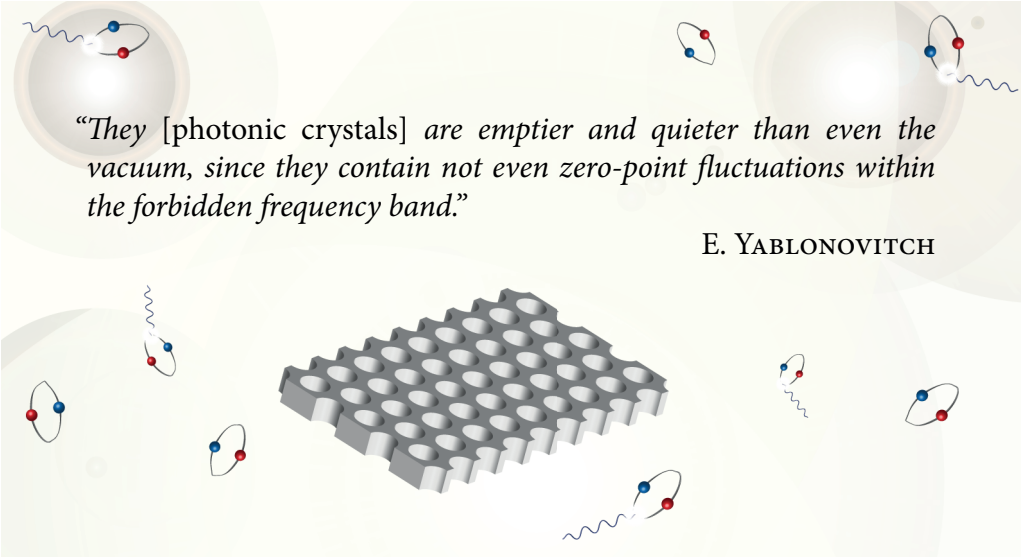

Figure 1.1 | Yablonovitch's quotation about photonic crystals. Artwork; vacuum fluctuations outside a photonic crystal slab surrounding the famous quotation about the "quietness" of photonic crystals inside the forbidden frequency band (Yablonovitch 1992).

The words quoted above are taken from an article of Eli Yablonovitch (1992), published five years after his pioneering publication on *Inhibited spontaneous emission in solid-state physics and electronics* (Yablonovitch 1987), which forms the foundation for the entire field of *photonic crystals*. Photonic crystals are dielectric materials with an artificially modulated index of refraction, providing a periodic potential for photons on a length scale of the photon wavelength. Their "quietness" stems from the absence of quantum mechanical states in the frequency range of the *photonic bandgap* – the optical analog of the electronic bandgap as known from semiconductor physics. Yablonovitch understood, that this specific property of these novel materials offers completely new ways for light-matter interaction as well as for light guidance and confinement on a *nanometer scale*.

Probably the most promising application of photonic crystal structures is in future computer chips, since the technical development of conventional computers is still driven by miniaturization in order to keep up with Moore's law (Moore 1965). In the current purely electronic chip designs higher integration densities are limited by two factors: power dissipation and sensitivity to signal synchronization. The energy problem in particular is an issue of supercomputers, which consume enormous quantities of electricity. For example, the current fastest supercomputer Tianhe-2 in China has a total power consumption of 24 MW (including cooling) and a performance of 33.86 petaflops (quadrillion floating point operations per second), as reported by Dongarra (2013). For comparison, in 2009 a US person had an average energy consumption of about 10 kW (source: *U.S. Energy In-*

formation Administration). The Tianhe-2 thus has a power consumption comparable to a US-city with a population of 2400 people, revealing that future supercomputers achieving exaflops would need amounts of energy in the scale of megacities. Obviously, alternative concepts have to be found for such machines.

An obvious idea is to exploit *photons* rather than electrons for signal processing. Light features several advantages over electrons: it can transmit considerably larger amounts of information with a higher *speed*, since the speed of light is much higher than that of an electric impulse and dielectric materials offer a significantly larger *bandwidth* in the scale of terahertz, compared to a few hundred megahertz for electronic systems (modern ethernet). In addition, there is an essentially weaker interaction between photons than between electrons, which is desirable regarding energy dissipation (Joannopoulos and Villeneuve 1997). The corresponding rapidly developing field is referred to as *nanophotonics*. When nanophotonic devices succeed to operate coherently on the single-photon level, they might even serve to build quantum computers (Benson 2011). Anyhow, no matter if operated classically or in the quantum regime, single photon computers would not just open new dimensions of computing speed, they would also solve the energetic problems. For the ideal case, a power of 100 W could generate about $2.5 \cdot 10^{20}$ photons with a wavelength of 500 nm per second – supplying clock frequencies in the scale of hundreds of exahertz, if only single photons are needed for floating point operations.

On the road towards such integrated photonic technologies several fundamental photonic crystal applications have been investigated. Today, low-loss waveguides and high-quality resonators are well understood and can be manufactured even for *visible light*. Accordingly, first successful approaches towards integrated all-optical devices and its components have been realized (for example Asakawa et al. 2006, Englund et al. 2007, Faraon et al. 2011).

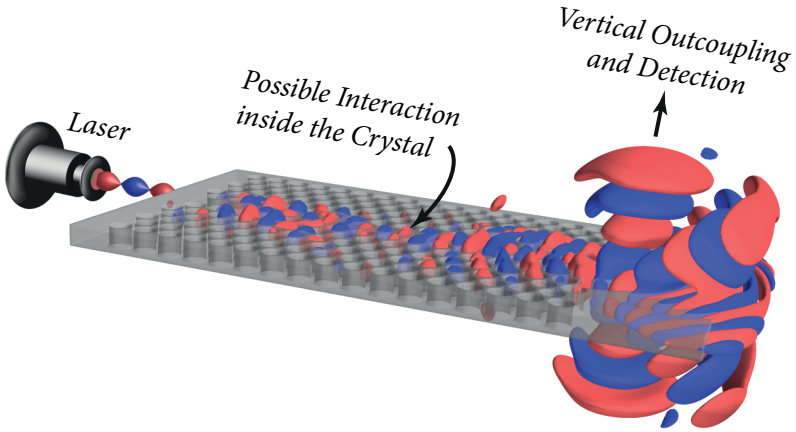

Figure 1.2 | Artistic depiction of the vertical outcoupling process. The grating coupler terminating the photonic crystal waveguide vertically scatters the incoming light, potentially produced by a laser source. Inside the photonic crystal waveguide, interactions with resonators and/or single two-level dipole emitters are possible. The shown fields inside the photonic crystal are numerically computed isosurfaces of the E_y-field component during the outcoupling process, depicting positive (red) and negative (blue) field values of identical amplitude.

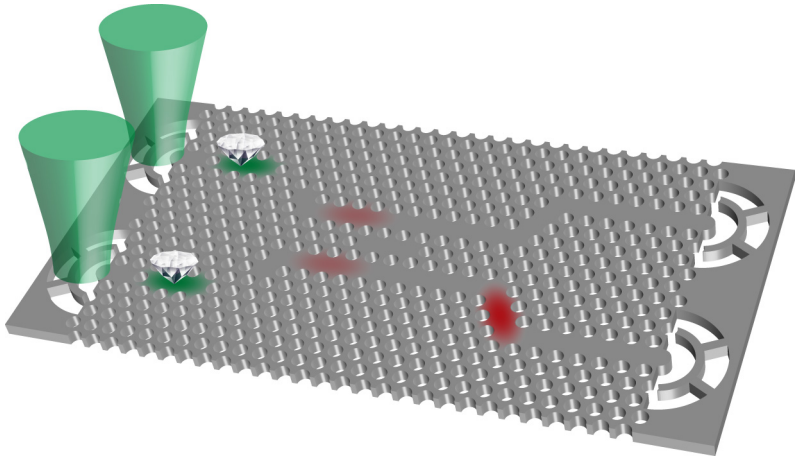

Figure 1.3 | Visualization of a possible on-chip Hong-Ou-Mandel experiment. Nitrogen-vacancy centers (diamonds) inside photonic crystal cavities could be excited using laser beams directed on grating couplers, which are coupled to waveguides for their part. Emitted identical single photons are brought to interference using coupled waveguides, leading to geminate occurrence of the photons at one output port at a time.

However, in many cases there is the demand to effectively in- or outcouple light into or out of a photonic crystal in the *vertical direction*. This way, it is avoided to guide light over long distances on the chip and instead directly insert it at the desired position. Also, vertical outcoupling is needed to read-out the information, since on-chip detection is still a challenging task (although already implemented by Reithmaier et al. (2013)). An example is shown in figure 1.2, where laser radiation is directly inserted into a photonic crystal slab-type waveguide terminated by a grating outcoupler. The grating vertically scatters a portion of the light, facilitating to capture it with a detector located above it. Inside the crystal, interactions with quantum mechanical systems like nitrogen-vacancy centers or quantum dots may take place.

Further applications of nanophotonic devices along with the ultimate goal of a working single photon computer are imaginable in *basic research*, as well. One example would be an on-chip *Hong-Ou-Mandel experiment* (Hong et al. 1987), as illustrated in figure 1.3. In this experiment, two identical photons are made to interfere in a specific region of space. As depicted, a laser beam split into two identical fractions could be directed onto grating couplers on a photonic crystal chip. The couplers scatter the light into a photonic crystal waveguide (very short in the figure), coupled to a resonator in which nitrogen-vacancy centers are placed. Consequently, these (quasi) two-level systems are excited and can emit identical single photons into a guided mode of subsequent waveguides, which then converge and are coupled to each other using another cavity. If the photons are coincident at the region of interference, the *Hong-Ou-Mandel effect* occurs: after the interaction, the photons will be observed in pairs at one of the output ports at a time. The detection could again be afforded using grating outcouplers, as indicated.

To contribute to the development of future integrated nanophotonic devices operating in the visible frequency range, this thesis engages in the investigation of photonic crys-

tal components meeting these demands. To this end, numerical techniques are applied to study elements such as cavities, waveguides and outcouplers and to design a chip suitable for the characterization of their parameters with the help of experimental methods. A chip designed in this fashion was produced and the photonic crystal samples contained herein are investigated by means of transmission spectra measurements and a back focal plane analysis. The primary focus is on the validation of the functionalities of a grating-structure presented by Faraon et al. (2007), for which physical characteristics such as the efficiency and the directivity are studied. After the theoretical fundamentals and the numerical methods have been explained in chapter 2, the results will be presented in chapters 3 and 4 – split into a numerical and an experimental part. A detailed discussion is then given in chapter 5, followed by concluding remarks in chapter 6.

2 Theory and Numerical Methods

Photonic crystals – at least two- and three-dimensional ones – are a rather new field in physics. They were firstly understood as an independent sort of material by Yablonovitch (1987), one hundred years after Lord Rayleigh explored the one dimensional version – the Bragg mirror. The theoretical fundamentals were already well-known at that time, formed from the Maxwellian electromagnetism. Fortunately, the late exploration of photonic crystals as they are known today led to the fact, that their theoretical description could largely benefit from results of solid state physics.

In the present chapter, the essentials of electromagnetism for photonic crystals will be explained and a more modern view using symmetries will be used to derive the theoretical origin of basic photonic crystal properties. This foundation will then be used to describe two computational methods, which were of great significance for the results of this thesis.

2.1 Electromagnetism regarding Photonic Crystals

Photonic crystals manifest a close similarity to solid state crystals, in which the special properties are caused by the interaction between electronic waves and their spatially symmetrical, atomic environment. The theoretical basis of such quantum mechanical systems is formed by the Schrödinger equation, describing the propagation of electrons as particle waves through a symmetrical potential. Analogously, photonic crystals can be interpreted as electromagnetic waves traveling through a dielectric environment which offers translational symmetry.

However, the propagation of light through dielectric materials is described by the Maxwell equations. Starting from the very general case, an expression similar to the Schrödinger equation will be derived, clarifying the relation between photonic and solid state crystals. With the scale invariance of the Maxwell equations, a fundamental and important difference between both systems will be presented. From this foundation, the important properties of photonic crystals will be derived from symmetry considerations.

2.1.1 Wave Equations

Considering the universal case of a space in which *absorbing materials* and *sources of electromagnetic energy* may exist, the light propagation is described in SI-units by the macroscopic Maxwell equations (Jackson 1998)

$$\vec{\nabla} \cdot \vec{B} = 0, \qquad \vec{\nabla} \cdot \vec{D} = \rho, \qquad \vec{\nabla} \times \vec{E} + \frac{\partial \vec{B}}{\partial t} = -\vec{M}, \qquad \vec{\nabla} \times \vec{H} - \frac{\partial \vec{D}}{\partial t} = \vec{J}. \tag{2.1}$$

Here, $\vec{E}$ and $\vec{H}$ are the electric and magnetic fields, $\vec{D}$ and $\vec{B}$ the electric and magnetic flux densities and $\vec{J}$ and $\vec{M}$ the electric and equivalent magnetic current densities, respectively. For the studied cases, one can assume that the electric and magnetic properties of involved materials are independent of field, direction and frequency. These materials are referred to as *linear*, *isotropic* and *nondispersive* – exhibiting simple relations between fields and flux densities

$$\vec{D} = \epsilon\vec{E} = \epsilon_r\epsilon_0\vec{E} \quad \text{and} \quad \vec{B} = \mu\vec{H} = \mu_r\mu_0\vec{H}, \tag{2.2}$$

where ϵ is the electrical permittivity, composed of relative and free-space permittivity ϵ_r and $\epsilon_0 \approx 8.854 \cdot 10^{-12}\,\mathrm{F\,m^{-1}}$ and μ is the magnetic permeability, equivalently composed of relative and free-space permeabilities μ_r and $\mu_0 = 4\pi \cdot 10^{-7}\,\mathrm{H\,m^{-1}}$. Additionally, $\epsilon_r(\vec{r})$ is a purely real and positive quantity when dealing with *transparent materials* (Joannopoulos et al. 2008). The current densities $\vec{J}$ and $\vec{M}$ can act as *independent sources* of electric and magnetic energy, $\vec{J}_{\text{source}}$ and $\vec{M}_{\text{source}}$ (Taflove and Hagness 2005). When applying finite-difference time-domain (FDTD) simulations (section 2.2.3), one additionally needs to allow materials with isotropic, nondispersive (ohmic) electric and magnetic losses for the attenuation of the E- and H-fields, yielding

$$\vec{J} = \vec{J}_{\text{source}} + \sigma\vec{E} \quad \text{and} \quad \vec{M} = \vec{M}_{\text{source}} + \sigma^*\vec{H}, \tag{2.3}$$

where σ and σ^* are electric and equivalent magnetic conductivities. It might be noted, that $\vec{M}_{\text{source}}$ and σ^* do not have any physical equivalent. Nevertheless, they are useful for the implementation of sources and artificial materials which are of great importance in numerical techniques like FDTD.

For the following analytical treatment all sources of light will be omitted, thus allowing to set

$$\rho = 0 \quad \text{and} \quad \vec{J} = 0. \tag{2.4}$$

Due to the linearity of the Maxwell equations, a separation of spatial and time-dependence is possible by expanding the E- and H-fields into a set of *harmonic modes*

$$\vec{E}(\vec{r}, t) = \vec{E}(\vec{r})\mathrm{e}^{\mathrm{i}\omega t}, \quad \vec{H}(\vec{r}, t) = \vec{H}(\vec{r})\mathrm{e}^{\mathrm{i}\omega t} \tag{2.5}$$

with ω as the *mode frequency*. Together with the equations (2.2) and (2.4), the curl equations of (2.1) can thus be combined to yield the *wave equations*

$$\frac{1}{\epsilon_r(\vec{r})}\vec{\nabla} \times \left[\vec{\nabla} \times \vec{E}(\vec{r})\right] = \left(\frac{\omega}{c}\right)^2 \vec{E}(\vec{r}), \tag{2.6a}$$

$$\vec{\nabla} \times \left[\frac{1}{\epsilon_r(\vec{r})}\vec{\nabla} \times \vec{H}(\vec{r})\right] = \left(\frac{\omega}{c}\right)^2 \vec{H}(\vec{r}), \tag{2.6b}$$

where the vacuum speed of light $c = 1/\sqrt{\epsilon_0\mu_0}$ has been introduced. If for any t_0 in a homogeneous material the condition $\vec{\nabla} \cdot \vec{D}(\vec{r}, t_0) = \vec{\nabla} \cdot \vec{B}(\vec{r}, t_0)$ is fulfilled, then $\vec{\nabla} \cdot \vec{D}(\vec{r}, t) = \vec{\nabla} \cdot \vec{B}(\vec{r}, t)$ holds for all times $t > t_0$. Then, the remaining two divergence Maxwell equations

$$\vec{\nabla} \cdot \vec{D}(\vec{r}, t) = 0 \quad \text{and} \quad \vec{\nabla} \cdot \vec{B}(\vec{r}, t) = 0 \tag{2.7}$$

need only be satisfied for $t = 0$ and the system will be completely determined by the equations (2.6). Actually, even one of these two equations is sufficient, since the missing field can always be expressed by means of the known one, using one of the equations

$$\vec{E}(\vec{r}) = \frac{\mathrm{i}}{\epsilon(\vec{r})\omega}\vec{\nabla} \times \vec{H}(\vec{r}), \tag{2.8a}$$

$$\vec{H}(\vec{r}) = -\frac{\mathrm{i}}{\mu\omega}\vec{\nabla} \times \vec{E}(\vec{r}). \tag{2.8b}$$

2.1.2 The Wave Equation as an Eigenvalue Problem

Both of the wave equations (2.6) can be regarded as *eigenvalue problems* of the form $\hat{\Theta}\mathcal{F} = a\mathcal{F}$, consisting of an operator $\hat{\Theta}$, a field function $\mathcal{F}$ and a scalar eigenvalue a. However, the transversality requirement for the E-field $\vec{\nabla} \cdot \epsilon_r\vec{E} = 0$, which has to be considered for calculations, has an additional ϵ-dependency. This is not true for the H-field, since one most often deals with non-magnetic materials for which μ_r is very close to unity (Joannopoulos et al. 2008). Thus, equation (2.6a) needs to be rewritten for the D-field to solve this problem, but this introduces additional prefactors in the eigenvalue problem again.

Consequently, it is convenient to use the H-field eigenvalue problem for calculations. From now on, ϵ_r will be abbreviated as ϵ and $\mu_r = 1$ will be assumed. The eigenvalue problem can thus be written as

$$\hat{\Theta}\vec{H}(\vec{r}) = \left(\frac{\omega}{c}\right)^2 \vec{H}(\vec{r}), \tag{2.9}$$

with the *linear*, *hermitian*, *positive semi-definite* operator defined by the equation

$$\hat{\Theta}\mathcal{F}(\vec{r}) := \vec{\nabla} \times \left[\frac{1}{\epsilon(\vec{r})}\vec{\nabla} \times \mathcal{F}(\vec{r})\right], \tag{2.10}$$

having non-negative eigenvalues ω^2/c^2 and thus ω is *real*. This equation is pretty similar to the Schrödinger equation, where the Hamiltonian – a linear, hermitian operator – acts on the wave function ψ to result in the energy eigenvalue multiplied by the wave function again. In the photonic case, the eigenfunctions $\vec{H}(\vec{r})$ correspond to the *spatial patterns of the harmonic modes* and the eigenvalues are proportional to the *mode frequency* ω (Joannopoulos et al. 2008).

As for quantum mechanics, a *variational principle* (Sakurai and Napolitano 2011) also holds for electrodynamics – the *electromagnetic variational theorem*. From this theorem, expressions for several physical quantities can be derived. The *time-averaged physical energy* stored in the E- and H- fields, for example, is given by

$$U_E := \frac{\epsilon_0}{4}\int \mathrm{d}^3\vec{r}\,\epsilon(\vec{r})\left|\vec{E}(\vec{r})\right|^2, \tag{2.11a}$$

$$U_H := \frac{\mu_0}{4}\int \mathrm{d}^3\vec{r}\,\left|\vec{H}(\vec{r})\right|^2, \tag{2.11b}$$

and the rate of energy transport is given by the *Poynting vector*

$$\vec{S} := \frac{1}{2}\Re\left(\vec{E}^* \times \vec{H}\right), \tag{2.12}$$

where $\Re$ is the real part and the asterisk denotes complex conjugation (compare to Joannopoulos et al. (2008)). The Poynting vector includes the information about the direction and the intensity of the propagating light and accordingly is important for the computation of fluxes (section 2.2.3).

2.1.3 Scale Invariance

Apart from the similarities to quantum mechanics and hence solid state physics, an important difference has already been mentioned: the *scale invariance* of the Maxwell equations. Quantum mechanical effects appear strange to human beings, since they exclusively occur on a nanoscopic scale. The *classical limit* or *correspondence principle* – as proven by the Ehrenfest theorem (Ehrenfest 1927) – explains that classical physics are an approximation of quantum mechanics on a large scale. But as a consequence, these effects are never recognized without microscopic observation.

For electrodynamics, the case is fundamentally different. The wave equation (2.6b) describes the propagation of electromagnetic radiation through the considered materials entirely. Using a transform of variables $\vec{r}' = s\vec{r}$ and $\vec{\nabla}' = \vec{\nabla}/s$ for a scaling factor $s \in \mathbb{R}$, one can easily find the wave equation for a scaled dielectric environment $\epsilon'(\vec{r}) = \epsilon(\vec{r}/s)$

$$s\vec{\nabla}' \times \left(\frac{1}{\epsilon(\vec{r}'/s)} s\vec{\nabla}' \times \vec{H}(\vec{r}'/s)\right) = \left(\frac{\omega}{c}\right)^2 \vec{H}(\vec{r}'/s). \tag{2.13}$$

Identifying $\epsilon(\vec{r}'/s) = \epsilon'(\vec{r}')$ leads to

$$\vec{\nabla}' \times \left(\frac{1}{\epsilon'(\vec{r}')} \vec{\nabla}' \times \vec{H}(\vec{r}'/s)\right) = \left(\frac{\omega}{cs}\right)^2 \vec{H}(\vec{r}'/s), \tag{2.14}$$

which is the wave equation for a scaled mode profile $\vec{H}'(\vec{r}') = \vec{H}(\vec{r}'/s)$ and a scaled frequency $\omega' = \omega/s$ (Joannopoulos et al. 2008).

For that reason, no fundamental length scale exists for electrodynamics – leading to the two useful consequences, that

1. complicated nano-fabrication can be avoided for testing, since larger sized systems reveal the same properties for appropriately sized wavelength (e.g. microwaves) and
2. numerical investigations can be carried out using *dimensionless units* (section 2.2.1), producing results independent of a fixed length scale.

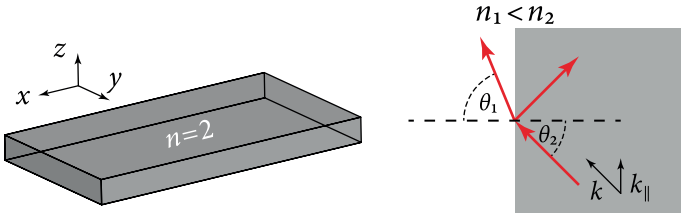

Figure 2.1 | The dielectric slab and index-guiding. The left hand side illustrates the dielectric slab – a plane of dielectric material which is comparatively small in one direction and infinitely large in the remaining directions, e.g. $\Delta z \ll \Delta x, \Delta y$. Rays crossing interfaces from higher to lower n are split into a reflected and a refracted ray, described by Snell's law (right hand side). For certain angles of incidence θ_1, total internal reflection occurs.

2.1.4 Continuous Translational Symmetry

The operator formalism for electrodynamics will not be covered any further. However, some results regarding *symmetries* are of great importance for the studied systems. Two important types of symmetries are

1. continuous translational symmetry and
2. discrete translational symmetry

of the dielectric function $\epsilon(\vec{r})$. In the case of *continuous translational symmetry*, the dielectric function fulfills the condition

$$\epsilon(\vec{r} - \vec{d}) = \epsilon(\vec{r}), \tag{2.15}$$

in which $\vec{d}$ is a displacement vector of real-valued constants $\vec{d} = (x, y, z)$, with $\{x, y, z\} \in \mathbb{R}$, in general. In *free space*, $\epsilon(\vec{r}) \equiv 1$ is independent of the position and consequently has translational symmetry in all three directions. In this case, the solutions of the wave equation (2.6b) are given by *plane waves*

$$\vec{H}_{\vec{k}}(\vec{r}) = \vec{H}_0 \mathrm{e}^{\mathrm{i}\vec{k}\cdot\vec{r}}, \tag{2.16}$$

where the *wave vector* $\vec{k}$ was introduced and $\vec{H}_0$ is a constant vector determining the direction of polarization (compare to Joannopoulos et al. (2008)). A system of more relevance, anyhow, is the *infinite dielectric slab*, depicted at the left hand side of figure 2.1. For the slab, the dielectric function is z-dependent exclusively – i.e. $\epsilon(\vec{r}) = \epsilon(z)$ – and the modes are classified by their in-plane wave vectors

$$\vec{k}_{\text{plane}} = k_x \hat{e}_x + k_y \hat{e}_y, \tag{2.17}$$

where $\hat{e}$ denotes the unity vector in the particular direction. The solutions are again plane waves, but $\vec{r}$ is replaced by a vector confined to the x-y-plane, yielding

$$\vec{H}_{n,\vec{k}}(\vec{r}) = \vec{H}'_{n,\vec{k}} \exp\left(\mathrm{i}\vec{k}_{\text{plane}} \cdot (x\hat{e}_x + y\hat{e}_y)\right). \tag{2.18}$$

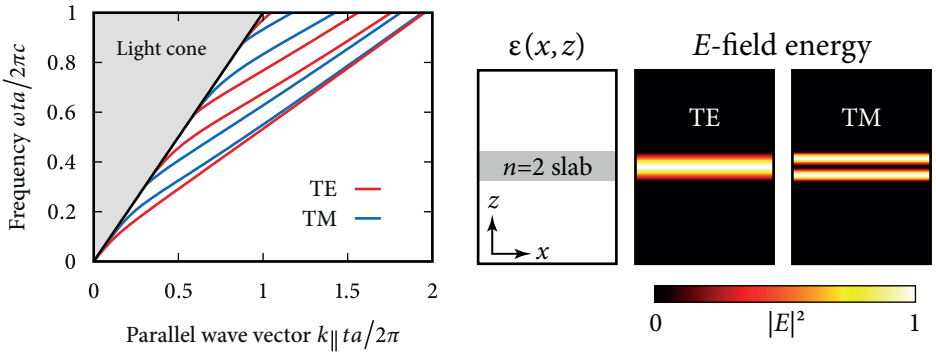

Figure 2.2 | Band structure and electric field distributions of the slab waveguide. The left hand plot depicts the dispersion relation for a dielectric slab of thickness t and $n = 2$ (Si_3N_4) as computed by *MIT Photonic Bands* (MPB). Red and blue lines correspond to TE- and TM-modes, respectively. The gray continuum shows the light cone, in which all modes are unconfined. On the right hand side, the dielectric and the electric field energy distributions of a TE- and a TM-mode are shown in the x-z-plane.

The polarization vector $\vec{H}'_{n,\vec{k}}$ is now $\vec{k}$-dependent as well. For a given value of $\vec{k}$, an infinite number of (mostly) *discrete* solutions exists which are numbered in order of increasing frequency by the *band number* n. From that point of view, the solutions are a set of *continuous functions* $\omega_n(\vec{k})$ referred to as *bands*, each one corresponding to a specific band number n. The sum of all those bands is called *band structure* or *dispersion relation*.

The system offers mirror symmetry with respect to the x-y-plane and thus a differentiation can be made between *even* and *odd* modes. For a two-dimensional membrane with vanishing extension in z-direction, the Maxwell curl equations decouple into two independent sets of equations: one set for the (H_x, H_y, E_z)-components and one for the (E_x, E_y, H_z)-components. The former set is referred to as *transversal magnetic (TM)*, the latter as *transversal electric (TE)*; a conventional labeling which is not unambiguous, but will be used to ensure comparability to other publications of the field. The mathematical derivation is shown explicitly in appendix A.1. For non-vanishing z-dimension, as for the slab, this differentiation only holds in the center of the slab – the plane of mirror symmetry. However, if the z-extension is smaller than the desired wavelength, one can still divide into *TM-like* and *TE-like*, for which the non-involved components are nearly zero. In most cases, TE-modes have a maximum in the center of a slab waveguide, while TM-modes have a node (Wolters 2013).

For a silicon nitride (Si_3N_4, $\epsilon \approx 4$) dielectric slab of thickness t, the band structure is shown in figure 2.2 (left). Red lines depict TE-modes and blue lines TM-modes. The structure was obtained by solving the wave equation (2.6b) numerically, using the open-source software package *MIT Photonic Bands* (MPB). A detailed description of the method will be given in section 2.2.2. On the right hand side, x-z-plane views of the dielectric distribution and the electric field energy $|\vec{E}|^2$ for a TE- and a TM-mode are shown. It is clearly visible, that the TE-mode exhibits a maximum in the center of the slab, while the TM-mode has a minimum – as expected.

Index Guiding

The reader may have noticed, that the band structure of figure 2.2 has not been explained entirely until now. The x-axes is labeled using $k_\parallel$, which is the wave vector *parallel* to the interface between the high index material and air, as illustrated at the right hand side of figure 2.1. Due to the continuous translational symmetry along that direction, $k_\parallel$ is a conserved quantity. The wave vector can be separated into fractions parallel and perpendicular to the interface, $k_\parallel$ and $k_\perp$. Since $k_\parallel = n\omega/c \cdot \sin(\theta)$ is conserved, one obtains *Snell's law*

$$n_1 \sin\theta_1 = n_2 \sin\theta_2 \tag{2.19}$$

by setting $k_\parallel$ equal on both sides of the interface (Joannopoulos et al. 2008), which reveals a critical angle

$$\theta_c = \frac{1}{\sin(n_1/n_2)}, \quad \text{if } n_2 > n_1. \tag{2.20}$$

For rays which are incident with angles larger than θ_c, *total internal reflection* occurs.

The black line in the band structure is the *light line* $\omega = ck_\parallel$. The gray region above it – the *light cone* – corresponds to solutions of Snell's law for angles smaller than θ_c. These modes extend to infinity and are thus not confined to the dielectric slab. The discrete bands $\omega_n(k_\parallel)$ below the light line are *index-guided* modes, which are bound to the dielectric slab.

2.1.5 Discrete Translational Symmetry: Photonic Crystal Slabs

The structures of interest for this thesis are *photonic crystal slabs*: thin membranes of dielectric material surrounded by air, for which the continuous translational symmetry is broken by periodically aligned holes. These membranes have a lot in common with dielectric slabs – the modes form a band structure and can be classified by TE and TM. Anyhow, due to the holes, only *discrete translational symmetry* occurs in x- and y-direction. Thus the dielectric function fulfills the condition

$$\epsilon(\vec{r} + \vec{R}) = \epsilon(\vec{r}) \quad \text{with} \quad \vec{R} = \sum_i m_i \vec{a}_i, \quad m_i \in \mathbb{Z}, \tag{2.21}$$

where $\vec{R}$ is an arbitrary lattice vector – a superposition of the *primitive lattice vectors* $\vec{a}_i$ (Barth 2010). A prominent structure used throughout this thesis is the *triangular lattice*, depicted in figure 2.3a. Each hole has six nearest neighbors with a center-to-center distance a, the *lattice constant*. The slab is composed of dielectric material and the holes with radius r consist of air.

The discrete translational symmetry is the property which reveals the strong similarities to solid state physics, where this symmetry is provided by the periodically aligned atoms. Therefore, the *Bloch-Floquet theorem* can be applied, which is well-known from solid state physics (Ashcroft and Mermin 1976). As a consequence, the solutions to the wave equation (2.6b) can be written as *Bloch waves*

$$\vec{H}_{n,\vec{k}}(\vec{r}) = \vec{u}_{n,\vec{k}}(\vec{r}) e^{i\vec{k}\cdot\vec{r}}, \quad n \in \mathbb{N}, \tag{2.22}$$

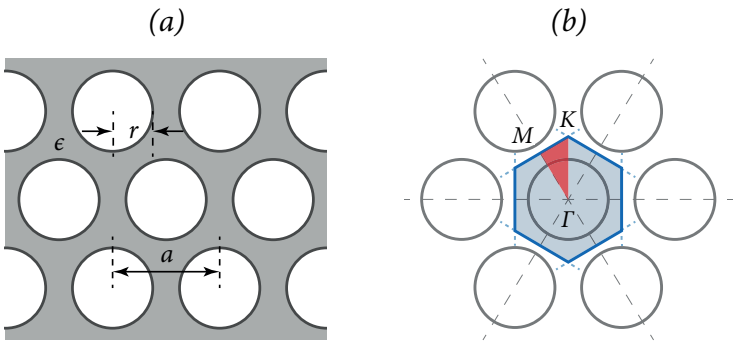

Figure 2.3 | The triangular lattice. (a) Outline of the triangular lattice with lattice constant a, hole radius r and relative permittivity of the material $\epsilon = n^2$. (b) Construction of the resulting 1. Brillouin zone (blue) and irreducible Brillouin zone (red) with its high symmetry points Γ, M, and K.

hence a product of plane waves and a function

$$\vec{u}_{n,\vec{k}}(\vec{r}) = \vec{u}_{n,\vec{k}}(\vec{r} + \vec{R}), \quad \forall \vec{R} \tag{2.23}$$

with the same periodicity as the lattice (see figure 2.4). In this case, $\vec{k}$ is the *Bloch wave vector*

$$\vec{k} = k_1\vec{b}_1 + k_2\vec{b}_2 + k_2\vec{b}_2 \quad \text{with} \quad a_i \cdot b_j = 2\pi\delta_{ij}, \quad k_1, k_2, k_3 \in \mathbb{C}, \tag{2.24}$$

where b_j are the *primitive reciprocal lattice vectors* and δ_{ij} denotes the Kronecker delta. The modes (2.22) are invariant under translations of the Bloch wave vector $\vec{k}$ by arbitrary reciprocal lattice vectors $\vec{G} = \sum_i m_i\vec{b}_i$.

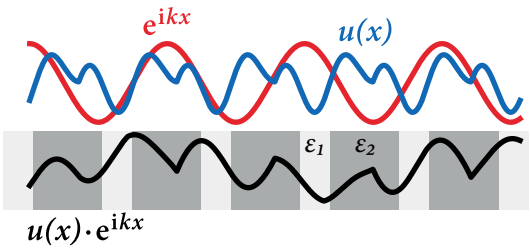

Figure 2.4 | Bloch-Floquet theorem. For a system with discrete translational symmetry in x-direction, The Bloch wave (black) can be decomposed into a plane wave $\exp(\mathrm{i}kx)$ (red) modulated by a lattice periodic function $u(x)$ (blue).

The primitive reciprocal lattice vectors are spanning their own lattice, which is shown in figure 2.3b for the triangular case. The blue region is known as the *first Brillouin zone* – only inside this zone nonredundant values for $\vec{k}$ exist. The bands $\omega_n(\vec{k})$ are only different for wave vectors that lie in the *irreducible Brillouin* (red triangle in the figure). Consequently, the band structure for such a system must only be considered for $\vec{k}$-values lying in this zone. The corners of the irreducible Brillouin zone are referred to as high symmetry points Γ, M and K.

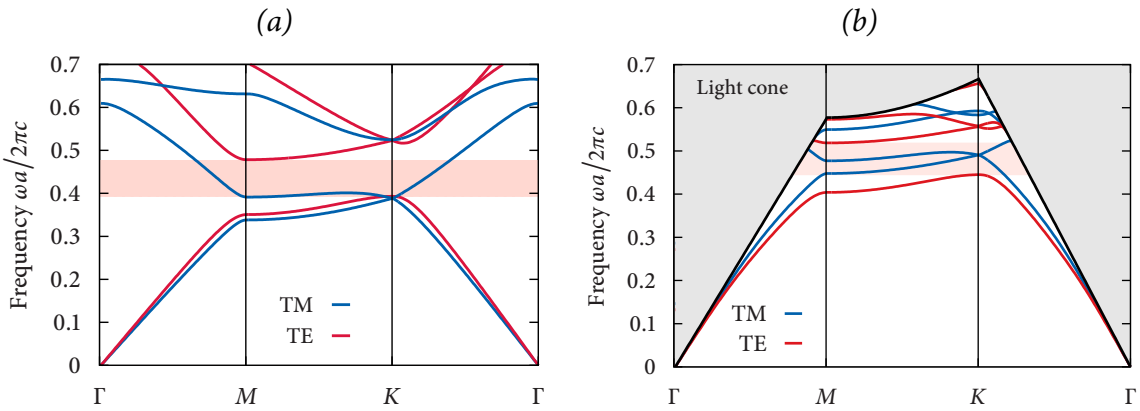

Figure 2.5 | Complete and incomplete bandgaps. Shown are band structures for a 2d photonic crystal (a) and a photonic crystal slab (b) with $n = 2$. Blue lines correspond to TM-modes, red lines to TE-modes. The bandgap is highlighted in light red. The 2d-system has a complete bandgap, while for the slab only an incomplete gap occurs – due to the light cone. Both structures are obtained using calculations with MPB (section 2.2.2), with parameters $r = 0.383$ for (a) and $r = 0.375$, $t = 0.8$ for (b).

2.1.6 Photonic Bandgaps

The mentioned properties of discrete translational symmetry systems can lead to a novel phenomenon, which is absent for the case of dielectric slabs (section 2.1.4) – the so-called *photonic bandgap*. Bandgaps are frequency ranges in the band structure for which no solution to the wave equation exists, at least for one of the two polarizations, TE or TM.

One has to distinguish between *complete* and *incomplete* bandgaps. Figure 2.5a shows an example of a complete bandgap. Plotted is the band structure $\omega_n(\vec{k})$ for a two-dimensional triangular photonic crystal with $n = 2$ and hole radius $r = 0.383a$ – a real 2d-system without expansion in z-direction. The x-axes transitions through Bloch wave vectors along the outline of the irreducible Brillouin zone (figure 2.3b), TE-modes are shown in red, TM-modes in blue. In the frequency range $f = 0.391c/a$ to $f = 0.477c/a$ no solutions for the TE-polarization exists – a complete photonic bandgap (highlighted in light red). Since TE- and TM-modes are eigenfunctions to a mirror reflection operator (which causes a mirror reflection on the plane of mirror symmetry) with different eigenvalues, they represent *orthogonal states* and thus do not couple. Accordingly, both polarizations can be treated separately (Joannopoulos et al. 2008).

Figure 2.5b shows the band structure for a photonic crystal slab of the same material, thickness $t = 0.8a$ and a hole radius of $r = 0.375a$. As for the dielectric slab, the interface between high index material and air introduces a light cone (gray region) that represents extended states. These states prevent the occurrence of a frequency range for which no solution exists and hence only allow incomplete bandgaps. For both kinds of bandgaps, light propagating with a combination of wave vector $\vec{k}$ and frequency ω that lies inside the photonic bandgap cannot penetrate into the structure. However, when dealing with defects in section 3.2, it will be shown that incomplete bandgaps have disadvantages when confining or guiding light.

2.2 Computational Electrodynamics

In section 2.1, the theoretical fundamentals necessary for the description of important phenomena occurring in photonic crystals have been presented. Using the Maxwell equations (2.1) or the derived wave equation (2.6b), the propagation of light through photonic crystals and hence the origin of the photonic bandgap can be understood.

In practice, these equations have to be solved for rather complicated structures, making it inevitable to apply numerical methods in the general case. From the huge quantity of available techniques, only those will be presented of which use has been made to generate results for this thesis. In fact, these are frequency-domain eigensolver techniques for the computation of band structures (section 2.2.2) and the finite-difference time-domain method (FDTD, section 2.2.3), mainly for the computation of transmission spectra. As an important insertion, before dealing with the two used methods *dimensionless units* will be discussed, as they are used by all utilized software packages.

It is a much-discussed question, which of the various numerical methods is favorable for a specific task and it strongly depends on the investigated structure, the quantities of interest and the personal taste. The well-known and easy to implement *beam propagation method* for example, is not well suited for photonic crystal slabs as it is only accurate for systems with a slowly varying dielectric distribution along the direction of propagation. Other techniques, such as finite-element or finite-volume methods, can reach considerably higher accuracies than the FDTD-method accompanying with a reasonable computational effort. Anyway, the disadvantage of these methods is comparative inflexibility when applying changes on the investigated structure, due to rather complicated meshing algorithms.

2.2.1 Dimensionless Units

As the Maxwell equations (2.1) have been proven to be scale invariant (section 2.1.3), a number of photonics-related software packages are using *dimensionless units*, understandably. Consequently, most numerical results that are presented in this thesis use these units as well, making it reasonable to give a summary at this point.

The basic unit length is chosen to be a dimensionless number a, defaulting to $a = 1$ in the simulations. The speed of light c, the vacuum permittivity ϵ_0 and hence the vacuum permeability $\mu_0 = 1/(\epsilon_0 c^2)$ are chosen to be unity

$$c \equiv 1, \quad \epsilon_0 \equiv 1, \quad \mu_0 \equiv 1, \tag{2.25}$$

as well. For that reason, the units of time $[t]$, frequency $[f]$ and velocity $[v]$ are given by

$$[t] = \frac{a}{c}, \quad [f] = \frac{c}{a} \quad \text{and} \quad [v] = c. \tag{2.26}$$

Appropriate expressions can be found for all other quantities of interest, such as mass or current.

In the simulations, a is typically chosen to be the *lattice constant* of the photonic crystal. The transformation to SI-units is done by setting a to the real (possibly measured) lattice constant and all other constants to their default SI-values.

2.2.2 Band Structure Calculation using Frequency-Domain Eigensolver Techniques

A theoretical explanation of the photonic band structure was given in section 2.1.5, and figure 2.5 already showed two examples of numerically computed band diagrams. In this section, the basic computational method of such calculations will be discussed in brief. Actually, the presented method is only suitable for *infinitely periodic systems*. It should be noted, anyway, that the method can also be applied to photonic crystal slabs when a supercell is introduced, even if they contain *defects*. Defects are any perturbations in the otherwise perfect crystal lattice – they are dealt with in section 3.2.

The propagation of light through such infinitely periodic systems was given by the wave equation (2.6b), which is repeated at this point

$$\vec{\nabla} \times \left[\frac{1}{\epsilon_r(\vec{r})} \vec{\nabla} \times \vec{H}(\vec{r}) \right] = \left(\frac{\omega}{c} \right)^2 \vec{H}(\vec{r}), \qquad \text{(2.6b revisited)}$$

together with the transversality requirement $\vec{\nabla} \cdot \vec{H}(\vec{r}) = 0$. The dielectric function was said to be lattice-periodic (equation (2.21)) and thus independent with respect to translations of arbitrary lattice vectors $\vec{R} = \sum_i m_i \vec{a}_i$ ($m_i \in \mathbb{Z}$). In reciprocal space, accordingly, the dielectric function is periodic in matters of the reciprocal lattice $\mathcal{G}$, spanned by the vectors $\vec{G} = \sum_i m_i \vec{b}_i$ (equation (2.24)). Hence, one can expand ϵ using a Fourier series (John and Busch 1999) or equivalently do the same for the *inverse dielectric function*

$$\frac{1}{\epsilon(\vec{r})} =: \eta(\vec{r}) = \sum_{\vec{G} \in \mathcal{G}} \eta_{\vec{G}} \mathrm{e}^{\mathrm{i}\vec{G}\cdot\vec{r}}, \qquad (2.27)$$

where the Fourier coefficients are given by

$$\eta_{\vec{G}} = \frac{1}{\Omega} \int_{1.\mathrm{BZ}} \mathrm{d}^3 r \, \frac{1}{\epsilon(\vec{r})} \mathrm{e}^{-\mathrm{i}\vec{G}\cdot\vec{r}}. \qquad (2.28)$$

In this equation, the integration is carried out over the complete first Brillouin zone, which has a volume of Ω.

The solutions of the wave equation have been stated to be Bloch waves (2.22) when dealing with structures that exhibit discrete translational symmetry. They have the form

$$\vec{H}_{n,\vec{k}}(\vec{r}) = \vec{u}_{n,\vec{k}}(\vec{r}) \mathrm{e}^{\mathrm{i}\vec{k}\cdot\vec{r}}. \qquad \text{(2.22 revisited)}$$

The same trick as for the inverse dielectric function can now be applied to the Bloch wave, resulting in

$$\vec{H}_{n,\vec{k}}(\vec{r}) = \sum_{\vec{G} \in \mathcal{G}} \sum_{\lambda=1}^{2} h^{\lambda}_{\vec{G}} \hat{e}^{\lambda}_{\vec{G}} \mathrm{e}^{\mathrm{i}\vec{G}\cdot\vec{r}}. \qquad (2.29)$$

The first summation again runs over all reciprocal lattice vectors and the second one over both transverse polarizations, labeled by the index λ. The $h^{\lambda}_{\vec{G}}$ indicate vector-valued Fourier coefficients and the unit vectors $\hat{e}^{1}_{\vec{G}}$ and $\hat{e}^{2}_{\vec{G}}$ are orthogonal to each other and to $(\vec{k} + \vec{G})$

$$\hat{e}^{1}_{\vec{G}} \times \hat{e}^{2}_{\vec{G}} = \frac{\vec{k} + \vec{G}}{|\vec{k} + \vec{G}|} \qquad (2.30)$$

and thus implement the transversality requirement. Inserting (2.27) and (2.29) into the wave equation (2.6b) converts the initial eigenvalue problem into a form which is accessible through numerical techniques

$$\sum_{\vec{G}\epsilon\mathcal{G}} \sum_{\lambda'=1}^{2} = \mathbb{M}^{\lambda\lambda'}_{\vec{G}\vec{G}'} h^{\lambda'}_{\vec{G}'} = \left(\frac{\omega}{c}\right)^2 h^{\lambda}_{\vec{G}} \tag{2.31}$$

with the infinite matrix

$$\mathbb{M}^{\lambda\lambda'}_{\vec{G}\vec{G}'} = \eta_{\vec{G}-\vec{G}'} \left|\vec{k}+\vec{G}\right| \left|\vec{k}+\vec{G}'\right| \begin{pmatrix} \hat{e}^2_{\vec{G}} \cdot \hat{e}^2_{\vec{G}'} & -\hat{e}^2_{\vec{G}} \cdot \hat{e}^1_{\vec{G}'} \\ -\hat{e}^1_{\vec{G}} \cdot \hat{e}^2_{\vec{G}'} & \hat{e}^1_{\vec{G}} \cdot \hat{e}^1_{\vec{G}'} \end{pmatrix} \tag{2.32}$$

(John and Busch 1999). Actually, the infinite matrix $\mathbb{M}^{\lambda\lambda'}_{\vec{G}\vec{G}'}$ needs to be reduced to a finite size by restricting the number of reciprocal lattice vectors to a common finite subset, as stated by Wolff (2011). The result is a matrix problem: the matrix can be diagonalized using standard numeric libraries and the eigenvalues can be computed using – for example – iterative eigensolver techniques, such as the *Arnoldi algorithm* (Arnoldi 1951), if one restricts the results to a finite number of bands.

The entirety of all possible methods which solve equation (2.31) are called *frequency-domain eigensolver techniques* (or sometimes *plane wave expansion methods*). For infinitely periodic systems, the computation is carried out by giving a real-valued Bloch wave vector $\vec{k}$ and finding the eigenfrequencies $\omega_n(\vec{k})$. This important class of problems is referred to as *standard band structure computation*. The opposite case of giving a frequency ω and finding possible wave vectors is called *on-shell band structure computation*. This rather complicated scheme gives the chance to also find complex-valued k-vectors and thus *attenuated waves*, but is not further covered in the scope of this thesis (see for example Wolff 2011).

MIT Photonic Bands

The software which was used exclusively to perform standard band structure computations is *MIT Photonic Bands (MPB)*, which was developed by Steven G. Johnson at the Massachusetts Institute of Technology and was described in detail by Johnson and Joannopoulos (2001). The package includes improvements of the standard procedure in view of computational speed and memory by using fast Fourier transforms and improves the accuracy of the spatial discretization from first to second order. A more detailed explanation can again be found in the thesis of Wolff (2011).

2.2.3 Finite-Difference Time-Domain Method (FDTD)

MPB demonstrates a state-of-the-art implementation for the frequency-domain eigensolver technique, which can be used to numerically solve for bands in photonic crystal structures. It thus gives the chance to gain insight into important phenomena present in photonic crystals as photonic bandgaps – but also guided modes in a line defect (see section 3.4), for example.

However, there are mechanisms and quantities which need to be characterized from a *time-domain* point of view. These are for example the propagation of light around bends, the field decay in a resonator or transmission and reflection spectra of arbitrary scatterers.

For such problems, the finite-difference time-domain method provides a feasible technique. It discretizes the dielectric distribution on a (mostly) cubic grid and solves the complete time-dependent Maxwell equations in a leap-frog manner – allowing to model complicated structures for wide frequency ranges in a single run. Consequently, it was used intensely to obtain important results for the investigation of photonic crystal nano-cavities, waveguides and grating couplers (chapter 3). According to its significance, the method will be studied in some detail in this section. The aim is to give an introduction to the topic which is as compressed as possible, while as complete as necessary. The main source for the treatise is the book of Taflove and Hagness (2005), which can be seen as the standard textbook on FDTD. Allen Taflove himself is one of the pioneers in the field, he for example coined the FDTD acronym (Taflove 1980) and was the first one to apply the near- to far-field transformation (Umashankar and Taflove 1982), presented in section A.2.

Finite Differences

The important advantage of the FDTD-method is, that it is able to solve the *full time-dependent Maxwell equations* (2.1), which are repeated at this point

$$\begin{aligned} \vec{\nabla} \cdot \vec{B} &= 0, & \vec{\nabla} \times \vec{E} + \frac{\partial \vec{B}}{\partial t} &= -\vec{M}, \\ \vec{\nabla} \cdot \vec{D} &= \rho, & \vec{\nabla} \times \vec{H} - \frac{\partial \vec{D}}{\partial t} &= \vec{J}. \end{aligned} \tag{2.1 revisited}$$

No further analytical tricks have to be applied and thus no further demands are made on the investigated structures. Additionally, there is no linear algebra involved in the method, making the possible number of field unknowns boundless (i.e. only limited by memory resources).

However, the Maxwell equations are a set of dependent equations including complicated *differential operators* which have to be evaluated. The trick is to directly approximate these differential operators by means of *finite differences*.

By subtracting the Taylor expansions of a function $f(x,t)$ at locations $x_i + \Delta x/2$ and $x_i - \Delta x/2$ at fixed $t = t_n$, one can obtain an approximation for the first derivative in space as

$$\left.\frac{\partial f}{\partial x}\right|_{x_i,t_n} = \left[\frac{f(x_i + \Delta x/2) - f(x_i - \Delta x/2)}{\Delta x}\right]_{t_n} + O\left[(\Delta x)^2\right], \tag{2.33}$$

which is called a *second-order accurate, central-difference approximation*. In this equation, $O\left[(\Delta x)^2\right]$ is a shorthand notation for the remainder term, expressing that the error shrinks with the square of Δx. One can now discretize time and space on a regular grid

$$x_i = i\Delta x, \qquad i \in \mathbb{N}, \tag{2.34}$$

$$t_n = n\Delta t, \qquad n \in \mathbb{N} \tag{2.35}$$

to achieve a shorter notation for equation (2.33)

$$\left.\frac{\partial f}{\partial x}\right|_{x_i,t_n} = \frac{f^n_{i+1/2} - f^n_{i-1/2}}{\Delta x} + O\left[(\Delta x)^2\right]. \tag{2.36}$$

An analog equation can be found for the time derivative

$$\left.\frac{\partial f}{\partial t}\right|_{x_i,t_n} = \frac{f^{n+1/2}_i - f^{n-1/2}_i}{\Delta t} + O\left[(\Delta t)^2\right]. \tag{2.37}$$

The Yee-Lattice

Equations (2.36) and (2.37) can now be used to derive *update equations* for the electric and magnetic field components of the Maxwell equations. However, at the end of the day one desires to solve problems in three dimensions, taking into account the fact that the Maxwell equations are connected between each other: a moved current induces a magnetic field and vice versa magnetic fields can generate electric fields. Consequently, a staggering scheme must be found, which logically implements the topology of the Maxwell equations.

The most popular scheme is the *Yee-lattice* (Yee 1966) which is illustrated in figure 2.6, showing a single *unit cell* of size $\Delta x \times \Delta y \times \Delta z$. As before, the positions on the lattice and in time are given by indices

$$x_i = i\Delta x, \quad y_j = j\Delta y, \quad z_k = k\Delta z \qquad i, j, k \in \mathbb{N}, \tag{2.38}$$

$$t_n = n\Delta t, \qquad n \in \mathbb{N}. \tag{2.39}$$

The electric and magnetic field components are stored at different locations in space. This effectively implements the Maxwell equations, as for example H-fields are forming a curl around E-fields and vice versa. The induction at a different location in space is connected to a *transport of information*. Accordingly, the fields also have to be *staggered in time* –

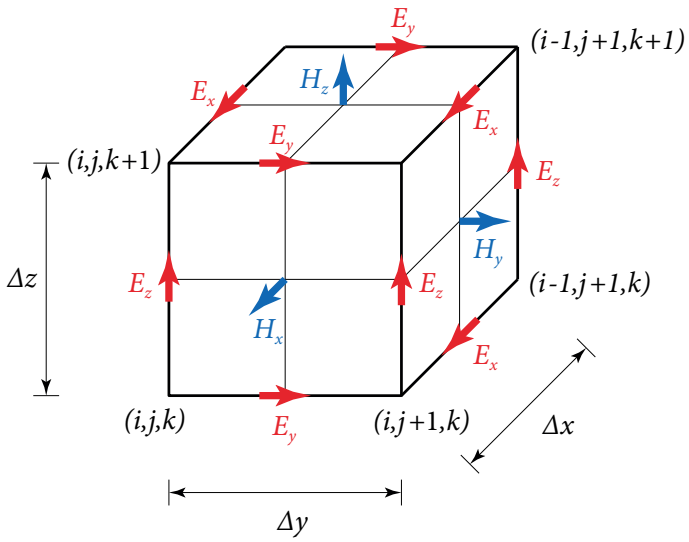

Figure 2.6 | Cubic unit cell of the Yee space lattice. Positions of the electric (red) and magnetic (blue) field vector components and numbering of the grid indices for a single unit cell in the Yee lattice of size $\Delta x \times \Delta y \times \Delta z$. The magnetic fields are stored at different locations than the electric fields.

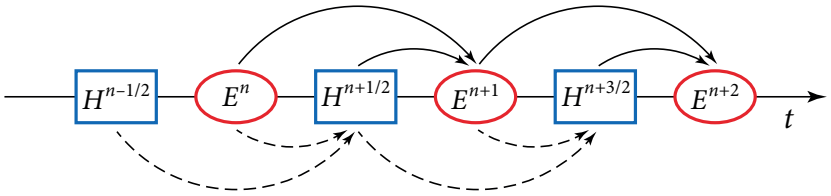

Figure 2.7 | Time stepping in the Yee-algorithm. Magnetic fields are stored at half time steps. The computation of a given component at a given time t_n always uses the results at times $t_{n-1/2}$ and t_{n-1}.

known as a *leap frog* algorithm, illustrated in figure 2.7. One time step is executed in the following order

1. the E-fields at t_{n+1} are computed from the E-fields at t_n and the H-fields at $t_{n+1/2}$. Afterwards,
2. the H-fields at $t_{n+3/2}$ are computed from the H-fields at $t_{n+1/2}$ and the E-fields at t_{n+1}.

Obviously, for the first time step the fields have to be initialized in some way.

Since information can not be transmitted with a velocity greater than the speed of light c, one can not choose the length of one time step freely – there must be a relation to the spatial discretization. Most often, the unit cell is chosen to be cubic, thus

$$\Delta x = \Delta y = \Delta z := \Delta r. \tag{2.40}$$

We can then define the *Courant number* S

$$S = \frac{c\Delta t}{\Delta r}, \tag{2.41}$$

which is a measure for the *numerical stability* of an FDTD simulation. More specifically, the condition $S \leq 1$ must be fulfilled in order to get numerically stable solutions and is called *Courant-Friedrich-Lewy criterion* (*CFL-criterion*). The FDTD-method is thus said to be *conditionally stable*.

Moreover, the case of $S = 1$ defines a maximum allowed time step, which is called *magic time step* and thus might be desirable. Its duration is

$$\Delta t = \frac{\Delta r}{c}. \tag{2.42}$$

For this choice of Δt one can show, that the numerical dispersion relation is an exact representation of the analytical dispersion relation. Unfortunately, for the magic time step one is very close to the edge of violating the CFL-criterion, and due to imperfect numbers in programming languages this really might happen. Consequently, smaller values for Δt are chosen, leading to a modified dispersion relation. The case is known as *numerical dispersion* and causes, for example, that an analytically dispersion-free wave packet diverges in a linear medium.

Subpixel Smoothing

The presented scheme was described to be of second order accuracy, since the approximations of the differential operators (2.36) and (2.37) are of the same order. Actually, this is only true for dielectric distributions which are exactly aligned with the Yee-grid and thus rectangular. For photonic crystals one often needs to simulate circular structures (figure 2.3), which would reduce the accuracy of the procedure to first order if they were naively implemented.

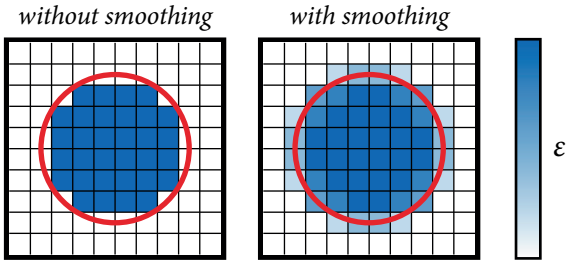

Figure 2.8 | Illustration of subpixel smoothing. The red line shows the outline of a circle which should be reproduced by the rectangular grid. Without smoothing, the corresponding ϵ is only assigned to pixels which lie primarily inside the structure. With smoothing, intermediate values for ϵ are used to restore second order accuracy.

The left hand side of figure 2.8 shows how a circle (red line) would be represented on a grid composed of square pixels. Only those pixels which lie primarily inside the circle are chosen to have the corresponding refractive index. Such an implementation would reduce the accuracy of the algorithm to first order. Fortunately, second order accuracy can be restored by a technique called *subpixel smoothing* (or subpixel averaging), described by Farjadpour et al. (2006). In this approach, intermediate ϵ-values are assigned to pixels which lie only partially inside a constant-ϵ region. This is illustrated on the right hand side of figure 2.8.

Sources

It is stated, that the fields have to be set to initial values at the very first time step. A possible choice would be to set all field values to zero except one point (i, j, k), where the E_z-component could be varied sinusoidally in time

$$E_z|^n_{i,j,k} = E_0 \sin(2\pi f n \Delta t), \tag{2.43}$$

for example. This would implement a simple point source of frequency f, which is known as a *hard source* in FDTD literature. However, these source conditions are quite unphysical and thus seldom used in FDTD codes. Instead, *current sources* are used which are implemented through the $\vec{J}$-terms in the Maxwell equations (equation (2.3)).

Concretely, the source which was used in most simulations is a J-current source with a temporal profile of a normalized differentiated Gaussian pulse (Gedney 2011)

$$f(t) = -\frac{t - t_0}{t_w} \exp\left[-\frac{(t - t_0)^2}{t_w^2}\right], \tag{2.44}$$

where t_0 is the time delay and t_w the half width of the pulse – implementing a Hertzian dipole. This source has a frequency bandwidth of $f_{\text{bw}} = 1/\pi t_w$ and the highest frequency is commonly assumed to be $f_{\text{high}} = 2/\pi t_w$.

Current sources present a much more physical implementation of excitations than hard sources. As in real systems, the resulting field amplitudes depend on the surrounding structures and materials, precisely on the local density of optical states. This is an important characteristic when trying to compute transmission spectra using two distinct simulations, for example. One needs to assure, that the source is embedded in exactly the same environment, to have an equal emission in both simulations.

Boundary Conditions and Perfectly Matched Layers

An issue which has not been dealt with so far is the boundary condition. The FDTD simulation is always limited to a finite region of space and thus the question arises how to treat fields at boundaries. The simplest case would be to set all E- or H-field values to zero at boundaries, known as *perfectly electric* and *perfectly magnetic conductor*, respectively. The result is a *reflecting boundary*.

Anyhow, in many cases the interest is on *absorbing boundary conditions* (ABC) (or *open boundary conditions*), such as when dealing with scattering problems or propagation through waveguides. This rather complicated problem is more or less an independent field in computational electromagnetics, which is documented in great detail by Taflove and Hagness (2005). However, it is worthwhile noting that the most important approach is called *perfectly matched layer* (PML), which was introduced by Berenger (1994).

The PML itself is not a boundary condition, but a quasi-material, which is inserted *before* the actual boundary. Incident waves of arbitrary angles are attenuated inside this medium and hence prevented from being back-scattered from the actual boundary. Omitting theoretical details, the PML is implemented using the σ and σ^* terms in equations (2.3) and represents the standard implementation of open boundary conditions in FDTD codes.

Of course, the attenuation is *not perfect* and depends on the thickness of the used PML-layer. In simulations, one needs to be sure to use a sufficient layer thickness and hence testing is often necessary. As a rule of thumb, a thickness of at least one longest occurring wavelength might be well-suited.

Flux Monitors as an Effective Tool for the Computation of Transmission/Reflection Spectra

As a last topic regarding FDTD, the calculation of flux spectra should be covered at this point. In most cases, it is not reasonable to store the calculated electric and magnetic fields at each grid point and for each time step. Actually, this is not even possible in many cases, since one is always trying to exhaust the potential of the machine and hence memory sizes are already at their limits. Consequently, it is a better approach to store only those fields which are essential for the computation of the desired quantity.

Using current sources, one has the ability to excite a broad-band wave packet and use it to illuminate an arbitrary scattering structure. The transmitted or scattered power in a particular direction can then be obtained as a function of frequency. This is what *flux monitors* are used for. During the simulation, the Fourier transforms of the electric and magnetics fields $\widetilde{E}$ and $\widetilde{H}$ on a surface S are allocated *on-the-fly*, using a discrete Fourier transform of the form

$$\widetilde{E} = \sum_n \mathrm{e}^{\mathrm{i}\omega n\Delta t}\vec{E}(n\Delta t)\Delta t, \tag{2.45}$$

as stated by (Oskooi et al. 2010). On the surface S, the integral of the Poynting flux is computed as

$$\mathcal{F}(\omega) = \Re\left\{ \oiint_S \widetilde{E}(\vec{r})^* \times \widetilde{H}(\vec{r})\, \mathrm{d}\vec{A} \right\}, \tag{2.46}$$

where $\vec{A}$ is orientated normal to the surface S and $\sim$ denotes a vector in phasor domain. This quantity, referred to as *flux*, can be used to calculate *transmission spectra* if the transmitted flux is divided by the incident flux, both measured in distinct simulations. To determine the optimum positions for these surfaces is a task specific to the investigated problem.

Using flux monitors is a great advantage in view of computer memory. One not only saves memory because the field values are stored in a smaller region of space, but also because only one (complex) number per frequency is necessary. They provide a straight forward and memory-efficient method to obtain flux related data at various locations in the desired direction. Examples of use are given in sections 3.5 and 3.6.

3 Results Part I: Numerical Results

It has been shown in the previous chapter, that computational electrodynamics offer a powerful instrument for the investigation of optical systems – especially for photonic crystals. Consequently, band-structure calculations and the FDTD-algorithm were used to study the systems of interest. The major advantage is the possibility to design a chip for later measurements without any effort of material or machines, and thus save a lot of time. Furthermore, simulations can help to validate measured results and help to understand them more completely.

The following sections contain all results that have been obtained using computer simulations. Results that have been achieved by physical measurements are presented in Chapter 4 (*Results Part II: Experimental Results*) and both are compared in Chapter 5 (*Discussion*). *Note* that *dimensionless units* are mainly used in this chapter. Exceptions are spectra that are closely related to later measured quantities, but these will be mentioned explicitly.

3.1 Maximum Bandgap Calculation

For many applications a large photonic bandgap is desirable. In practice, most parameters that have an influence on the bandgap size are fixed. For instance, the refractive indices of air and the substrate material as well as the substrate thickness – given by the manufacturer – will not be changed frequently, as they have a strong influence on the production processes. The remaining parameters are the hole radius r and the lattice constant a.

Characterization of the Bandgap Size

It has been shown in section 2.1.3, that it is more useful to work with dimensionless units, because of the scale invariance of the Maxwell equations. In the same manner, a good choice for the characterization of the gap size uses the so-called *gap-midgap ratio* $\Delta\omega/\omega_\mathrm{m}$ (compare to Joannopoulos et al. (2008)), where $\Delta\omega$ is the frequency width and ω_m is the frequency at the middle of the bandgap, respectively. This quantity, which will usually be given in percent, is independent of the lattice constant if all other dimensions (r, t) are scaled simultaneously.

Simulation Technique and Results

To compute the value of r for which the gap-midgap ratio reaches its peak value, several high resolution band calculations has been performed in *MPB* (resolution 32, mesh-size 7). A three-dimensional supercell was used consisting of one unit cell and the coordinates are chosen to point at the high-symmetry points Γ, M, and K. The SiN-slab of thickness $t = 0.8$ (approximately the thickness of the produced sample) was surrounded by air layers

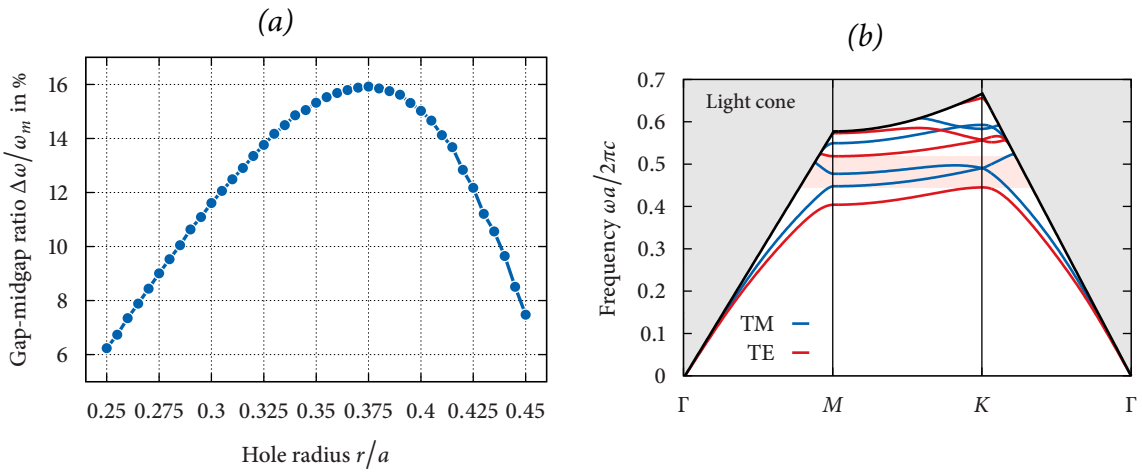

Figure 3.1 | Results of the maximum bandgap calculation. (a) Size of the bandgap as a function of hole radius r ($t = 0.8$, $n = 2$). The optimum bandgap is reached at $r = 0.375$ with a size of 15.92 %. (b) Corresponding band diagram for this hole radius. The TE-modes (red) show a photonic bandgap which is highlighted in light red. The TM-modes (blue) do not show a bandgap, the gray region corresponds to the light cone.

($n = 1$) with a thickness of 3.

For these fixed parameters, the values of r have been varied in the range of 0.25 to 0.45. Figure 3.1 shows the results of this investigation. The maximum bandgap is attained at $r = 0.375$ with a size of 15.92 %. The dispersion relation for that case is shown in figure 3.1b. Drawn are the lowest four TE- (red lines) and TM-modes (blue lines), the bandgap (light red) and the light cone (gray). The lower limit of the bandgap is located at $f_{\text{low}} = 0.44261$, the higher one at $f_{\text{high}} = 0.51915$. The TM-modes do not exhibit a bandgap.

3.2 Applications using Defects

The perfectly periodic photonic crystal does not offer a great variety of applications, except if *defects* are introduced into it. A defect is any imperfection in the lattice, for example shifted, shrunk, enlarged or removed holes. In general, such modifications lower the energy of bands, causing them to lie inside the bandgap. They represent states in which the light can exist in the area of the defect. Such states – more conveniently referred to as modes – are *evanescent* in the continuum of the perturbation-free crystal, and thus are located at or guided along the defect, consequently forming *resonators* or *waveguides*. From the infinite number of possibilities for these variations a few will be studied in the next sections.

3.2.1 Point-Defects

Point-defects are perturbations in a comparatively small region of the crystal lattice, most often forming *photonic crystal cavities*. The important advantages of such resonators are

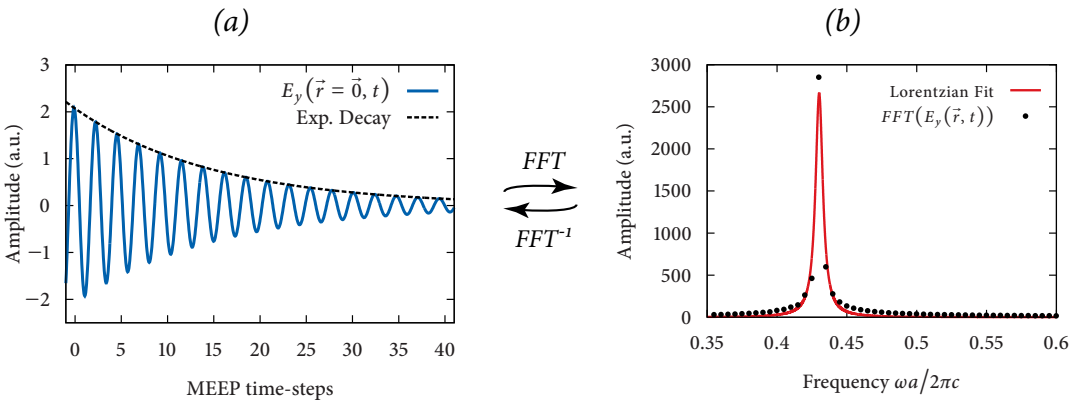

Figure 3.2 | Time-evolution in the L3-cavity. (a) Example for the time-evolution of the E_y component at the center of the L3-cavity (decay exaggerated for better visibility); (b) Fourier transform of this data with Lorentzian fit, revealing a frequency of $f \approx 0.43c/a$ and a quality factor of $Q \approx 135$.

- high quality factors (also called Q-factors/values),
- small mode volumes,
- high local density of optical states,
- the possibility of the insertion of quantum emitters,
- easy fabrication.

A cavity mode is a localized, exponentially decaying mode. As stated by Joannopoulos et al. (2008), the cavity mode frequency can be treated as a complex frequency

$$\omega_c = \omega_0 - \mathrm{i}\gamma/2, \tag{3.1}$$

with ω_0 as the resonance frequency and γ as the cavity loss rate. The energy inside the resonator decays as $\mathrm{e}^{-\gamma t}$. The *quality factor* is then defined as

$$Q := \omega_0/\gamma, \tag{3.2}$$

a dimensionless quantity for the characterization of the cavity loss rate. If the time-varying field inside the cavity is Fourier-transformed, one finds a Lorentzian peak proportional to $1/[(\omega-\omega_0)^2 + (\omega_0/2Q)^2]$. Thus, the Q-factor can also be interpreted as the inverse fractional bandwidth at half-maximum of this peak. This can be seen in figure 3.2, where an example time evolution at the center of the L3-cavity is shown for the E_y-component. The field shows a damped oscillation and the Fourier transform offers a Lorentzian peak. Typical Q-factors of photonic crystal cavities are on the order of 10^2–10^4, numerically much higher Q-values up to 10^7 have been demonstrated (Kuramochi et al. 2006).

The *mode volume* V is defined as the integral of the optical energy density $\frac{1}{2}\epsilon|\vec{E}|^2$, normalized to its maximum value, over space (compare to Saleh and Teich (2007))

$$V := \int \frac{\epsilon|\vec{E}|^2}{\max\left(\epsilon|\vec{E}|^2\right)} \mathrm{d}^3\vec{r}. \tag{3.3}$$

V is normally given in units of $(\lambda/n)^3$, where λ/n is the wavelength at the cavity resonance in the medium. It is on the order of 1 for photonic crystal cavities, which is very small compared to microsphere-resonators (~10^3), for example (Vahala 2003). If an emitter is brought into such a cavity, its emission is influenced by the surrounding structure: it can only emit into modes that exist in the cavity. Furthermore, the emission into high-Q modes is enhanced as a consequence of the *Purcell effect* (compare to O'Brien et al. (2009)). The enhancement is given by the Purcell factor

$$F = \frac{3}{4\pi^2}\left(\frac{\lambda}{n}\right)^3 \frac{Q}{V_{\text{eff}}}, \tag{3.4}$$

where Q is the cavity quality factor and V_{eff} is the effective mode volume (compare to Wolters et al. (2010)). The Purcell factor is proportional to Q/V (Purcell 1946), so large Q-values and small mode volumes are desirable. More precisely, the strength of the coupling between the emitter and the cavity modes is described by the *local density of optical states* (LDOS), whose spatial average is the density of states (García et al. 2009). If the LDOS is known for a cavity, the optimum position for a quantum emitter is known as well. Recently, Sapienza et al. (2012) presented a way to probe the LDOS for photonic crystal membranes using an electron beam, spatially and spectrally resolved. This way, the optimum emitter position can also be found experimentally. More details on cavity-quantum emitter systems are given in the appendix, section A.3.

The L3-Cavity

A very simple and often used resonator is the *L3-cavity*, formed by three missing nearest-neighbor holes. This resonator was intensely investigated: details on the mode structure can be found in Chalcraft et al. (2007) and possible optimizations have been discussed in the dissertation of Barth (2010). However, since its properties are known that well, the L3-cavity is a good choice to test if numeric or experimental tools work properly.

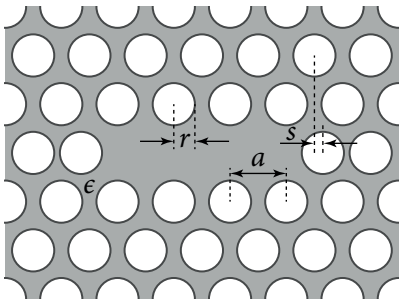

Figure 3.3 | Schematic diagram of the L3-cavity. The L3-cavity is a point-defect of three missing holes in the triangular lattice (in-line). Light can be localized in the defect region. The shift parameter s provides a simple way to improve the Q-factor of the resonator.

Some details of the L3-cavity can be found in figures 3.3 and 3.4. The geometry is shown in 3.3, defining the lattice constant a, the hole radius r and the outer-hole displacement s. The displacement s gives an easy producible possibility to improve the Q-factor and to fine-tune the resonance frequencies. Figure 3.4 shows the distributions of the E_x and E_y field components of the fundamental and the second mode, respectively, as computed by FDTD simulations.

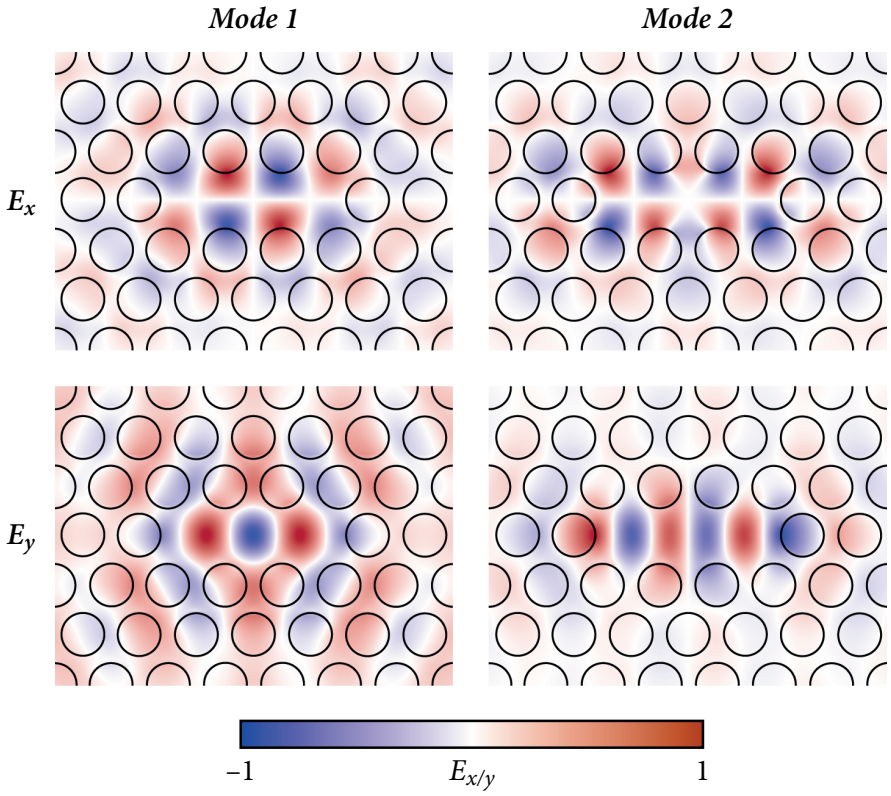

Figure 3.4 | Field Patterns of the L3-cavity. Shown are the E_x and E_y field components for the fundamental mode and the 2. mode of the L3-cavity, respectively ($E_z = 0$, because of TE). These profiles are calculated using the FDTD-method for the 2-dimensional case, but they are analog for 3d ($r = 0.38$, $s = 0$).

The LWM Line-Defect

The *local width modulated (LWM) line-defect* gives an example for an advanced photonic crystal cavity, offering ultrahigh-Q-factors of up to $7 \cdot 10^7$ in simulations and $8 \cdot 10^5$ in the experiment (Kuramochi et al. 2006). Another example would be the double-hetero structure, which has been reported to be able to reach Q-factors of $2 \cdot 10^7$ if it is optimized (Song et al. 2005).

A possible geometry for an LWM-cavity is shown in figure 3.5a. Firstly, a line-defect is formed by removing a complete line of nearest-neighbor holes: a W1-waveguide (see section 3.2.2). Then, there are three sections of holes having different shift values away from the line-defect: red holes (A) are shifted by d_A, green holes (B) by d_B and blue holes (C) by d_C, with $d_A > d_B > d_C$. Additionally, the standard width of the W1-waveguide $l_{W1,0} = \sqrt{3}a - 2r$ can be adjusted to a new width $l_{W1} = C \cdot l_{W1,0}$.

Figure 3.5b shows the distribution of the electric field energy $|\vec{E}|^2$ inside the cavity as computed by an FDTD-simulation. A Q-factor of ~5500 was calculated, but no optimizations have been investigated. The confinement is smoother than for the L3-cavity and the profile is similar to the one of the guided modes inside a W1-waveguide. Because of that,

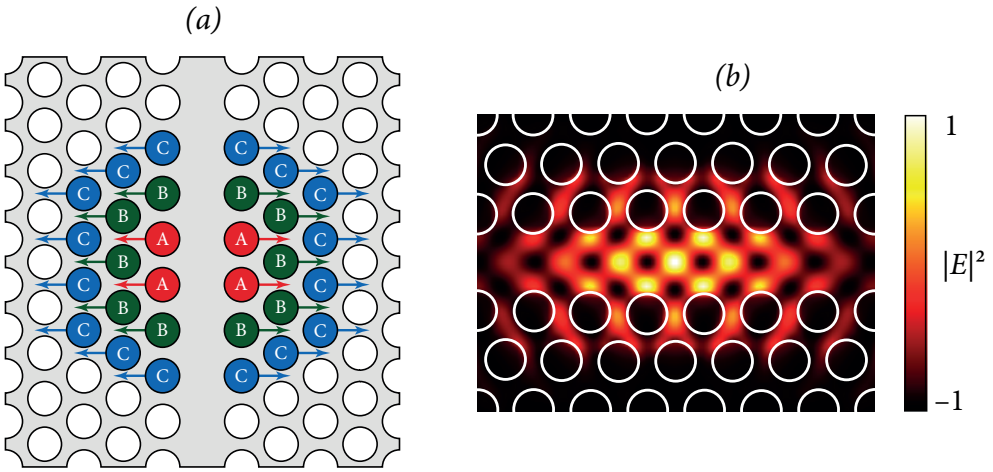

Figure 3.5 | The local width modulated (LWM) line-defect – an advanced photonic crystal resonator. (a) Possible geometry of the LWM-cavity formed by a missing line of holes (W1-waveguide) and a smooth shift of several holes at a particular position of the line-defect. Red holes (A) are shifted by d_A, green holes (B) by d_B and blue holes (C) by d_C – always away from the line-defect. (b) Distribution of the electric field energy $|\vec{E}|^2$ for the LWM-cavity.

the LWM-cavity could be a good choice for a filter as the coupling between waveguide and cavity should be effective. Further investigations would be necessary to give reliable statements.

3.2.2 Linear Defects

Linear defects are used to form *photonic crystal waveguides*. The modification is usually applied along a row of nearest-neighbor holes, but can also point along other directions. An important paper about photonic crystal waveguides was published by Johnson et al. (2000). Much of the following can be found in more detail in this paper. The main advantages of photonic crystal waveguides in general are

- the possibility to guide light by the photonic bandgap of the crystal, achieving near-zero losses,
- guiding light through sharp bends with near-zero reflection,
- coupling light efficiently to photonic crystal cavities.

In general, to show optimal performance, waveguides must fulfill three criteria (compare to Johnson et al. (2000)):

1. they must support true guided modes and be periodic along the direction of propagation,
2. they should be single mode in the desired frequency range and
3. the guided mode should lie within the bandgap.

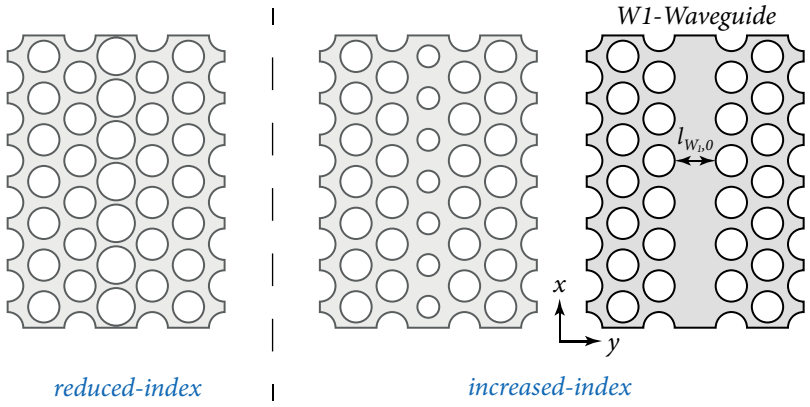

Figure 3.6 | Overview of photonic crystal waveguides. The left structure shows an example for reduced-index waveguides, for which the amount of high-index material is reduced. The other structures are increased-index waveguides with the limit case of the W1-waveguide (right).

The last criterion can only be satisfied by photonic crystals and this way they give the chance to completely eliminate radiation losses. Of course, one would need a photonic crystal with a true three-dimensional photonic bandgap to find such ideal conditions. Using photonic crystal slabs, which are quasi-2d, does not lead to this degree of perfection.

Index- and Gap-Guided Modes

In photonic crystal slabs the propagation of light is only inhibited by the bandgap in two directions (x and y in the current nomenclature). In the third direction, modes are confined by the dielectric contrast – they are index-guided. Because of that, one needs to clearly distinguish between *index-guided* and *gap-guided modes*. It will be shown in section 3.4, that one can easily discriminate these types of modes by performing a projected band structure calculation.

Increased- and Reduced-Index Waveguides

A further distinction can be made between two classes of photonic crystal waveguides: *increased-index* and *reduced-index*. Figure 3.6 shows some examples for both cases, all produced by the variation of nearest-neighbor hole radii. The W1-waveguide, which can be interpreted as the case of $r \to 0$, is one of the most often used types – again, as for the L3-cavity, because of its easy production (enlarged holes often lead to very thin parts in the dielectric material; strongly shrunk holes can be too small for the etching process). An additional design parameter for the W1-waveguide is its width $l_{W1,0}$. It can be used to shift the frequencies of the modes or even to design a single mode waveguide.

Field Patterns of the W1-Waveguide

The W1-waveguide is thus a simple line defect in which a single row of holes is missing. Figure 3.7 shows some H_z-field patterns for this system. The top row shows index-guided bands and the bottom row gap-guided bands. In section 3.4 it will be shown, that gap-guided modes always have higher frequencies than index-guided modes and where the shown modes lie in the projected band structure. At this point, one should notice that

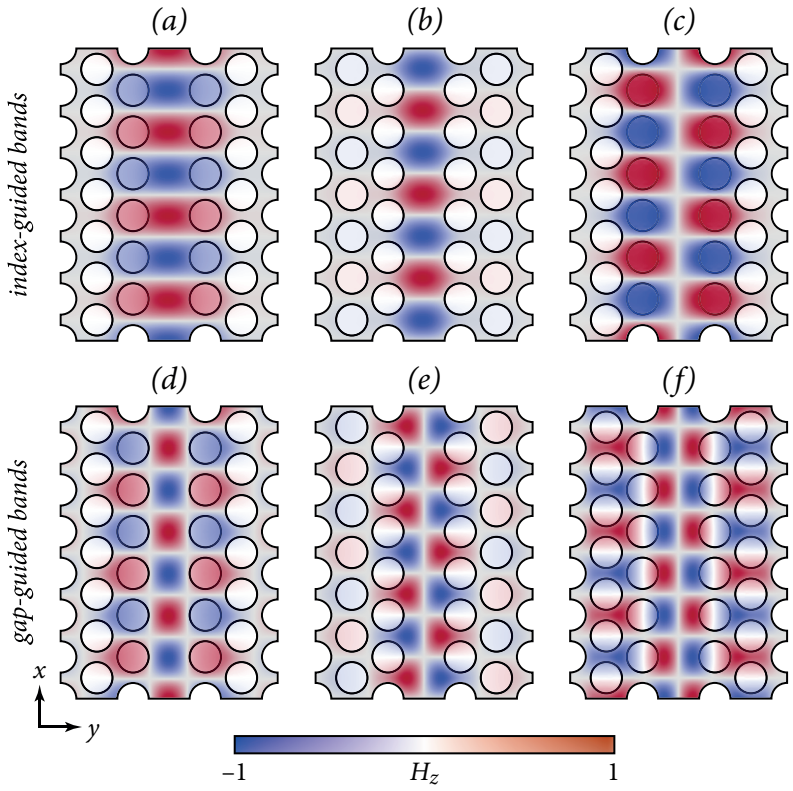

Figure 3.7 | Field patterns of guided modes for the W1-waveguide. The mode profiles show the distribution of the H_z-component at the $k_x = \pi/a$ point. (a)–(c) are index-guided, (d)–(f) are gap-guided modes. The exact positions of these modes in the projected band diagram can be found in figure 3.11.

there are modes which guide light in reduced-index regions (3d-photonic crystals can even guide light primarily in air). This way, the influence of absorption caused by the material is reduced. Details on the simulation technique used to calculated these field patterns will also be given in section 3.4.

3.3 Cavity Simulations

For the simulation of photonic crystal cavities the FDTD-method is an appropriate tool. Since the fields are decaying exponentially inside the crystal lattice and there is only a weak scattering in z-direction, one does not need to be concerned so much about boundary conditions. The physical membrane, surrounded by air and an comparatively thin PML is already a well-suited implementation. Anyhow, several points need to be considered more carefully. Firstly, the size and position of the point source must be chosen reasonably, since these parameters control which modes are excited. Secondly, the computation of mode frequencies and Q-factors must be carried out accurately.

Excitation of Modes
Different cavity modes are characterized by different frequencies *and* differing spatial distributions of the energy and accordingly their symmetries. This means, if an E_y-dipole source is used, only modes having a non vanishing E_y-component at the source location can be excited. The same problem arises if symmetries are applied to save time and memory: if the desired mode does not have the applied symmetry, the simulation will suppress it. For the L3-cavity, one can excite the fundamental mode with an E_y-source at the cavity center, but not the second mode, as can be seen in figure 3.4.

Q-Factor Determination (Harmonic Inversion)
Different approaches exist for the determination of resonance frequencies and Q-factors for the excited modes. The easiest procedure would be to record the values of a specific field component at a particular position inside the cavity as a function of time, thus finding $E_y(\vec{r} = \vec{0}, t)$, for example. If the Fourier-transform is applied, one finds several Lorentzian peaks – one for each resonant mode – having maxima at the respective frequencies and full-width at half-maximum values corresponding to the inverse Q-factors (as was stated in section 3.2.1). This was already demonstrated in figures 3.2a and 3.2b.

However, a more convenient and stable method when using the open-source FDTD implementation *MIT Electromagnetic Equation Propagation (MEEP)* (Oskooi et al. 2010) utilizes the *harmonic inversion*. With the harmonic inversion it is possible to calculate all frequencies, decay constants, phases, and amplitudes for a given discrete-time, finite-length signal that consists of a sum of finitely-many sinusoids (compare to the `harminv`-documentation, `http://ab-initio.mit.edu/wiki/index.php/Harminv`, Jan. 2014).

Numerically, the fields of a specific component at a particular position are decomposed using a time-series

$$C(t) = \sum_k d_k \mathrm{e}^{-\mathrm{i}\omega_k t}, \tag{3.5}$$

where $C(t)$ can be any component of $\vec{E}$ or $\vec{H}$ as a function of time, d_k are coefficients and ω_k are the complex resonance frequencies according to equation (3.1). A technique to efficiently implement this method is known as *filter diagonalization method* and was firstly presented by Mandelshtam and Taylor (1997). It has been demonstrated by Oskooi et al. (2010), that the filter-diagonalization method calculates the parameters more accurate and needs essentially less time-steps in the FDTD simulation.

3.3.1 Influence of the Surrounding Crystal

> *For this and the next section all simulations have been performed using the optimum parameters of section 3.1: a slab-thickness of* 0.8 *and a hole-radius of* 0.375*. It is assumed, that the influence of the surrounding holes and the s-parameter optimization are basically the same, if these design parameters are only changed slightly.*

Ideal two-dimensional photonic crystal cavities for which the surrounding crystal is extended infinitely can capture light perfectly – the modes have infinite Q-factors. Accordingly, the calculated Q-factors in 2d-FDTD-simulations are steadily increasing if the crys-

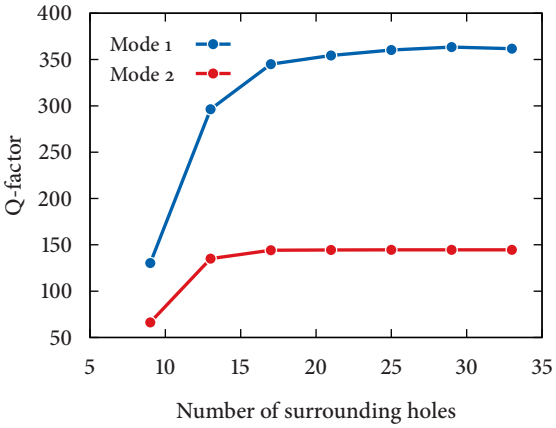

Figure 3.8 | Dependency of the Q-factor from the number of surrounding holes. The blue and the red curves correspond to the fundamental and the second mode, respectively. The simulation used the same number of holes for the x- and y-direction. From $M = N \approx 21$ a saturation of the Q-factor is reached – losses occur mainly in z-direction.

tal is enlarged. When dealing with photonic crystal slabs, one finds a saturation of the Q-values, since the loss channel of z-scattering is not influenced by the surrounding photonic crystal. In other words, an infinitely large photonic crystal slab cavity looses energy only because of the imperfect index-confinement.

To find an approximate value for the saturating number of surrounding holes, FDTD-simulations have been performed for "cubic" photonic crystals using the unoptimized L3-cavity. Cubic, in this case, means that the number of hole-rows (M) and hole-columns (N) has been chosen to be equal – the size of the crystal itself is not cubic. Figure 3.8 shows the results of this computation for the first two modes and M/N-values from 9 to 33. The expected saturation takes place approximately at a size of $M = N = 21$, but this may strongly depend on the Q-factor.

3.3.2 Q-Factor Tuning

As a simple design optimization parameter, the outer hole shift (s-parameter, see figure 3.3) has been investigated for a crystal of $M = N = 17$ holes. The results are shown in figure 3.9. Plotted is the dependency of the Q-factor (blue, left axis) and the resonance frequency (red, right axis) on s. For the fundamental mode, a doubling of the Q-factor is reached at $s \approx 0.275$. Apart from this, the resonance frequency can be tuned by about 1 %. For the 2. mode, a stronger frequency tuning of $\approx 4\,\%$ can be achieved, while the Q-factor is increased by a factor of ≈ 1.5 at $s \approx 0.1$.

Consequently, the s-parameter can be used to design two completely different characteristics. In addition – since the maxima for these two modes are reached for different values of s – one can forward a mode compared to another one regarding its Q-value.

Table 3.1 | Dominating modes for the produced L3-cavity. A comparison to experimentally measured results can be found in table 4.2.

Mode wavelength in nm	Q-factor
606.7	≈ 380
564.7	≈ 170

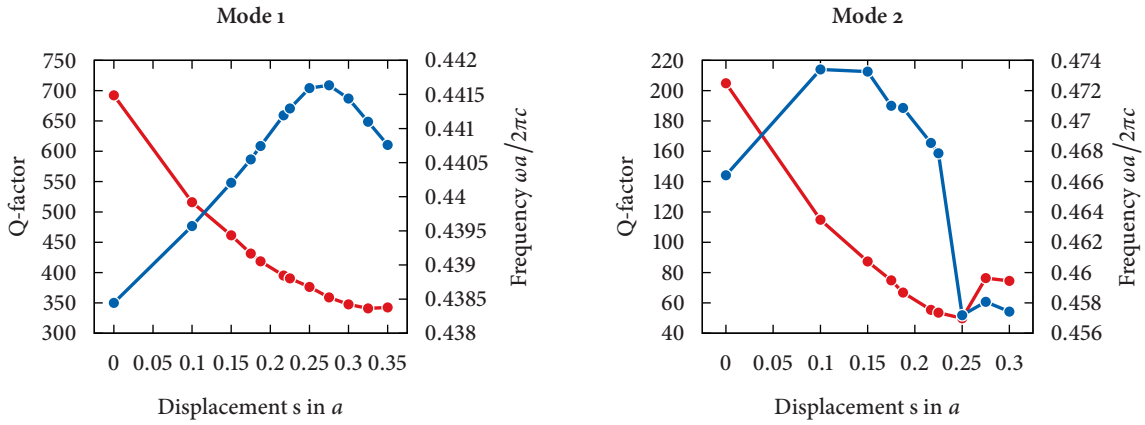

Figure 3.9 | Optimization of the *Q*-factor for the L3-cavity. Dependency of the Q-factor (blue, left axis) and the resonance frequency (red, right axis) on the s-parameter for the first two modes (in units of the lattice constant a). The maxima are reached at $s \approx 0.275$ for the 1. mode and $s \approx 0.1$ for the 2. mode, respectively.

3.3.3 Mode Frequencies of the Produced Photonic Crystal

For later comparison to the simulations and measurements regarding the produced chip, the mode frequencies and Q-factors for the L3-cavity have been computed using harmonic inversion. The parameters of the produced sample can be found in table 3.2.

Using several sources at different positions inside the cavity and also several positions at which the harmonic inversion was applied, the two dominating modes could be identified. Their mode wavelengths and approximate Q-factors can be found in table 3.1. They will be of importance later, when dealing with filters or real measurements on the L3-cavity.

3.4 Projected Band Structure of the W1-Waveguide

> *From this section on, the used design parameters of the simulated photonic crystals are the ones of the produced chip, which will be introduced in chapter 4. For an overview these parameters are listed in table 3.2 on page 34.*

In section 3.2.2, three criteria for an effective photonic crystal waveguide have been listed. Namely, the existence of true guided modes, the single mode characteristic in the desired frequency range and the fact that the modes should be gap-guided. All these qualities can be investigated by calculating the *projected band structure*.

3.4.1 Theoretical Considerations and Computational Method

If a line-defect is applied along the x-direction, the *discrete* translational symmetry of the crystal is broken. The only direction for which it is conserved is the direction along the defect. Thereby, the wave vector component k_x remains a conserved quantity of the system

(compare to Joannopoulos et al. (2008), Chapter 5). For point defects, each mode having a frequency ω inside the photonic bandgap is localized, which is a straight forward criterion. For linear defects, the situation is more difficult: only if the combination (k_x, ω) is disallowed in the crystal, the band will be forbidden – so there can be guided modes with frequencies lying outside the bandgap for suitable wave vectors k_x.

This difference has a simple cause: the Brillouin zone of the modified crystal is deformed relative to the unperturbed one – it is *projected*. This projection is illustrated in figure 3.10a. The linear defect points along the nearest-neighbor direction, thus the Γ-K-direction. Anyway, K is no longer the edge of the line-defect Brillouin zone. The M-point lies halfway between Γ and m. Projecting M onto the nearest-neighbor direction gives the edge of the new Brillouin zone – K' (compare to Johnson et al. (2000)). K' lies halfway between Γ and the projection of m, referred to as m'.

Consequently, to *project the band structure of the infinite crystal*, one has to select a value of k_x and find all possible values for k_y. These results are forming continuous regions when plotted versus k_x – the *slab band continua*.

Implementation in MPB

According to the theoretical analysis, one needs to do several band structure calculations in MPB to find all of the necessary information. The simulations split into two basic parts: (i) simulations using the *unperturbed crystal* to solve for the slab bands and (ii) simulations *with the line-defect* to solve for the waveguide modes. Both calculations are using *Cartesian coordinates* and for the defect simulation a supercell has to be used.

The computational domain for the waveguide simulation is highlighted by the black rectangle in figure 3.10b. Using more holes along the y-direction would lead to a higher accuracy, since the resulting separation between consecutive waveguides would be larger (although the modes are rapidly decaying inside the crystal). When solving for the z-even bands, one finds all guided and all forbidden modes corresponding to the line-defect. MPB is also able to output the field patterns for each band at a given k_x value, resulting in the distributions which had been presented in figure 3.7 of section 3.2.2.

The slab band calculation uses a smaller cell, but a lot more simulations have to be performed. For this thesis, 100 values for k_x have been chosen. For each of these values, 12 k_y points had to be solved for the first 4 bands. Always two bands together are forming a

Parameter	MEEP-value	SI-value
Refractive index n	2.0	2.0
Lattice constant a	1.0	261.20 nm
Slab thickness t	0.811 64	212.00 nm
Hole radius r	0.350 46	91.54 nm

Table 3.2 | Parameters of the produced sample. Listed are dimensionless units, as used for MEEP-calculations, and SI units.

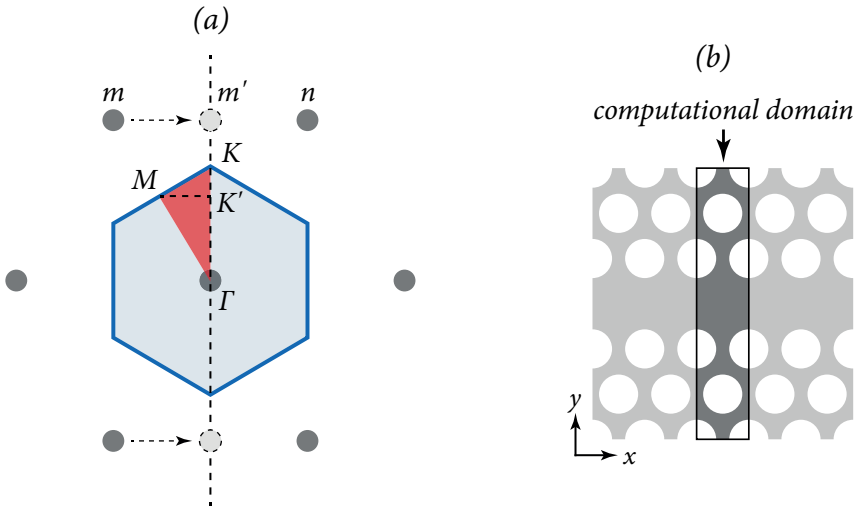

Figure 3.10 | Theoretical and computational details on the projected band structure calculation. (a) Projection of the reciprocal lattice onto the Γ – K-line. Gray dots represent the reciprocal lattice points, the blue region corresponds to the 1. Brillouin zone and the red area is the reduced Brillouin zone. After the projection, the new boundary of the 1. Brillouin zone transits through K'. (b) Computational domain for the MPB-simulation. The dark gray part inside the black rectangle corresponds to the vertical supercell. The W1-waveguide lies along the x-direction, so k_x is a conserved quantity.

continuum – in the region between these continua, the projected bandgap opens up. Consequently, the accompanying minimum and maximum of these conjugate bands had been chosen to form the outline of the continuum for the corresponding k_x-point.

3.4.2 Analysis of the Band Structure

Using the technique described in the previous subsection, one finds the band structure of figure 3.11. The inset again shows a sketch of the W1-waveguide for which this diagram was computed. The x-axis represents the wave vector component $k_x a/2\pi$ and reaches from Γ to K' (see figure 3.10a). The light cone is drawn in dark blue, while the slab band continuum is shown in light blue. The second slab band continuum lies above the light cone and is hence not visible.

Only modes which are both, lying outside the slab bands and the light cone, are *guided modes*. There are six guided bands in total. Three of them lie underneath the slab band continuum – these are the *index-guided modes* (green lines). The third one is barely visible, since it nearly lies inside the slab bands. The green modes are index-guided in all three directions, so they are not a special characteristic of the photonic crystal. Furthermore, they do not fulfill the 3. criterion for an effective waveguide. The red lines represent the bands of interest: the *gap-guided modes*. These modes are confined totally by the photonic band-gap in the x-y-plane and are index-guided in z-direction. As the gap-guided modes are lying in the bandgap – the region above the slab bands – they always have a higher

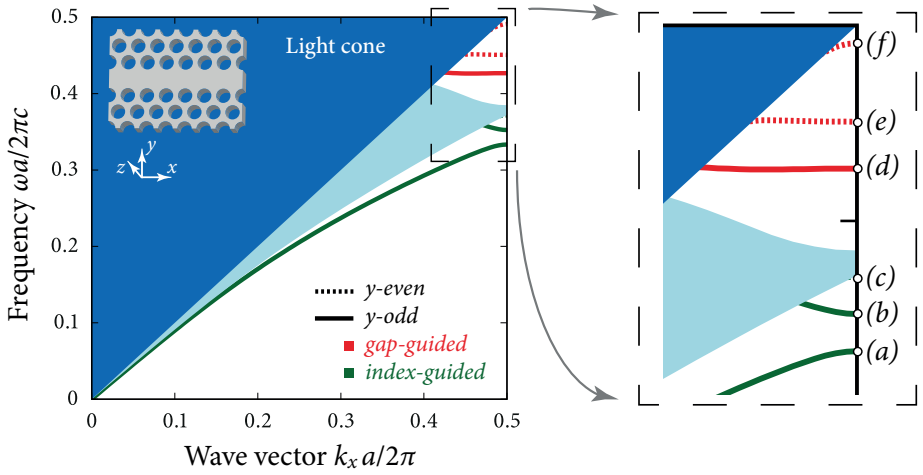

Figure 3.11 | Projected band structure of the W1-waveguide. Index-guided (green) and gap-guided (red) TE-like bands of the W1-waveguide (inset) versus the wave vector component k_x pointing along the defect. The extended TE-like modes of the defect-free crystal are forming a slab band continuum (light blue), the dark blue region corresponds to the light cone. The points (a)–(f) in the zoom are the positions at which the mode profiles of figure 3.7 have been calculated. The design parameters are listed in table 3.2.

frequency than the index-guided modes.

The 1. and the 3. criterion is fulfilled by the gap bands – they are truly guided and they are *partially* confined by the photonic bandgap. The word *partially* is important, since the fact that in z-direction only index-guiding is present limits the quality of the waveguide. This will be further investigated in section 3.5. The 2. criterion is fulfilled too – the waveguide is *single-mode* as there is at most one guided mode at a given frequency. If multiple rows would have been removed, the result would be a multi-mode waveguide, which is undesirable for information transmission as it leads to modal dispersion (Joannopoulos et al. 2008).

The H_z-field patterns at the marked points (a)–(f) in the zoom of figure 3.11 had been shown in figure 3.7. Since $\vec{H}$ is a pseudovector y-even modes look y-odd and vice versa (Jackson 1998). The real symmetry is marked in the figure by dashed (y-even) and solid (y-odd) lines. It has been stated by Joannopoulos et al. (2008) (Chapter 8) that y-odd modes are more easily excited by an incoming plane wave beam, due to identical symmetry.

3.5 Propagation Loss of the W1-Waveguide

When using a W1-waveguide in realistic cases one typically has to consider three different processes

1. the *incoupling*, i.e. the transition from the antecedent waveguide or grating to the photonic crystal waveguide,
2. the *propagation* through the W1-waveguide itself and

3. the *outcoupling* to the adjacent waveguide or grating.

Each of these processes introduces losses, leading to an *overall transmission* through the complete system. In this section, the focus will lie on the losses that occur during the propagation. The complete transmission spectrum will be investigated in section 3.6.

3.5.1 Loss Channels: The Exponential Decay

When disregarding bends, the main loss channels for common used waveguides are scattering at material imperfections and absorption. However, for photonic crystal waveguides there are a couple of additional loss mechanisms. These are, for example, the radiation of leaky modes (Hu and Menyuk 2009) and vertical radiation of Bloch-mode components (compare to Kappeler et al. (2011)). Without going into detail, the question is how these losses can be modeled.

From the results of the simulations, which will be presented in the following, the assumption of a simple *exponential decay* seems to be reasonable. Consequently, the used fit-function has the form

$$f(x) = P_0 \mathrm{e}^{-\alpha x}, \tag{3.6}$$

with α as the decay constant, P_0 as the initial power (which is of no interest) and x as the length of the waveguide. Of course, α might be a sum of all the involved decay constants α_k belonging to the different channels of losses k, thus $\alpha = \sum_k \alpha_k$.

3.5.2 The Method of Multiple Flux Monitors

To compute the propagation loss spectrum FDTD simulations have been used. Two main sources of errors need to be avoided to assure reliable results, which are

- light emitted by the source which is not bound to the waveguide and
- *reflections* inside the dielectric and/or the W1-waveguide.

To fulfill the needs the simulation technique illustrated in figure 3.12 was used. The left hand side consists of a dielectric waveguide of length l_{dw} with a spatially modulated dipole source – representing a Gaussian beam. The beam source has a directive radiation characteristic to initially insert as much light as possible into the waveguide. Using a large value for l_{dw} assures that most of the radiated light not bound to the waveguide has decayed away. Light which radiates to $-x$-direction (away from the W1) is then absorbed by the left PML (section 2.2.3), canceling all reflections inside the dielectric waveguide.

The right hand side consists of the photonic crystal with the W1-defect and multiple flux monitors which are separated by one lattice constant a (red lines in figure 3.12). These monitors are comparatively large in the y-direction, since the guided modes can have field patterns reaching widely into the crystal – this way, the monitors can record as much information as possible.

When the light arrives at the dielectric-W1-barrier a part of it is reflected. This radiation is not recorded by the monitors and decays inside the left PML. The other part couples into

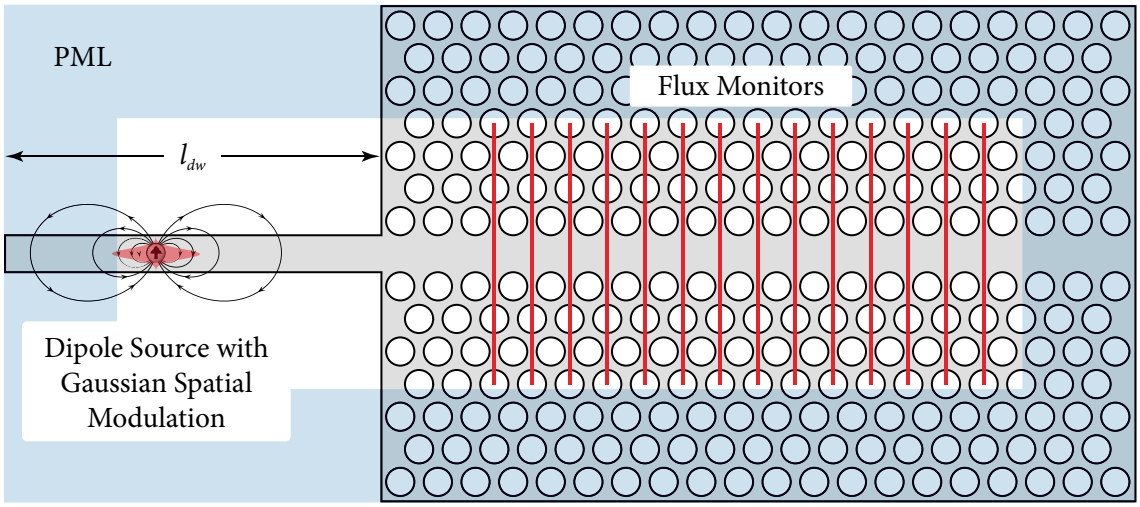

Figure 3.12 | Method of multiple flux monitors. Scheme of the used simulation setup (x-y-cut) for the computation of the propagation loss spectrum of the W1-waveguide. A Gaussian beam-source inside a dielectric waveguide is used to couple light into the W1-waveguide. Inside the W1 multiple flux monitors (red lines) with a distance of a record the transmitted power, while the PML suppresses the occurrence of reflections.

the W1. After some lattice constants – when the guided modes have formed – the light is recorded by the monitors and vanishes in the right PML.

A similar scheme was used by Kappeler et al. (2011). In contrast to the presented technique, they also used a dielectric waveguide after the W1-waveguide. Because of the involved in- and outcouple processes numerous reflections occurred in their simulation. Even if they presented a mathematical way to decompose the signal afterwards, the technique which was presented here seems to be more convenient, as the reflections are not produced and need not to be considered anymore.

3.5.3 Results and Discussion of Uncertainties

The simulation yields the flux through each of the monitors for each calculated frequency. Thus, for each frequency ω the flux $\mathcal{F}$ is known as a function of the position inside the waveguide: $\mathcal{F}(x, \omega)$. A fit of the results using equation (3.6) for each frequency ω results in a spectrum for the decay constants $\alpha(\omega)$ and additionally provides values for the corresponding variance σ^2. More conveniently, the propagation loss is given in units of dB/cm. If the distance x was given in cm, one can calculate the propagation loss in dB/cm then as

$$\alpha_{\mathrm{dB}} = 10 \log_{10} \left[\mathrm{e}^{-\alpha} \right]. \tag{3.7}$$

According to the law of error propagation the uncertainty of α_{dB} is then calculated from the standard deviation of σ by $u_{\alpha_{\mathrm{dB}}} = 10\sigma / \ln(10)$.

Figure 3.13 shows the results of a calculation using a resolution of 20 cells per lattice constant. The values for $u_{\alpha_{\mathrm{dB}}}$ are denoted by error bars and the bandgap – which was

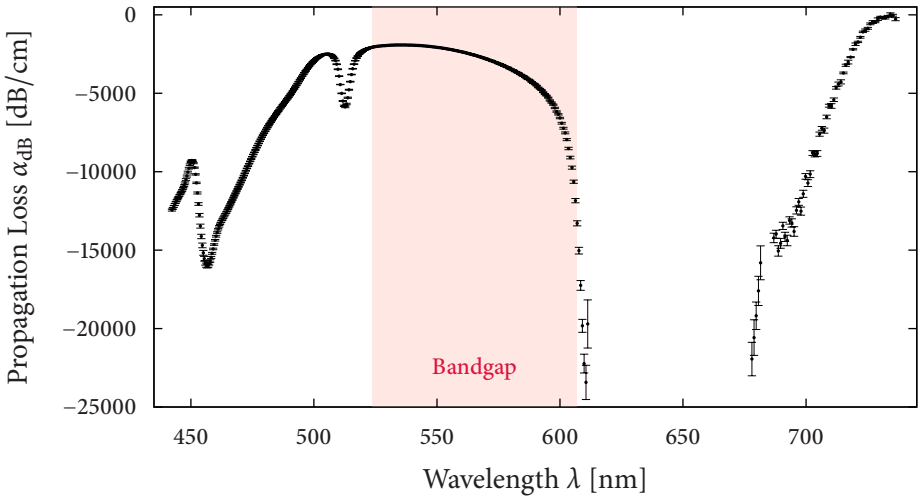

Figure 3.13 | Propagation loss spectrum of the W1-waveguide. Calculated values for α_{dB}, uncertainties are marked by error bars. The bandgap (calculated with MPB) is highlighted in red. Minimal loss inside the bandgap is reached at $\lambda \approx 535.37\,\text{nm}$ with $\alpha_{dB} = -1921 \pm 8\,\text{dB/cm}$. For larger wavelengths ($\sim 730\,\text{nm}$) near-zero losses have been computed.

calculated in MPB – is highlighted in red, ranging from 523.67 nm to 606.84 nm. For the comparison to experimental results the dimensionless units have been converted to absolute wavelength values using the production parameters of table 3.2 on page 34. Inside the photonic bandgap a local minimum of losses is reached at $\lambda \approx 535.37\,\text{nm}$ with $\alpha_{dB} = -1921 \pm 8\,\text{dB/cm}$. Note that α_{dB} is negative in the diagram, thus larger values are corresponding to smaller losses. At the long-wavelength edge of the bandgap the losses increase rapidly. They decrease again from $\sim 680\,\text{nm}$, reaching near-zero values at about 730 nm. Actually, even values slightly larger then 0 have been computed, but all having uncertainty intervals reaching values < 0. At the short-wavelength edge a dip is discovered at $\sim 512\,\text{nm}$ and an additional local maximum at $\sim 505\,\text{nm}$. For shorter wavelength the losses increase again.

3.6 Transmission and Reflection Spectra

It was already mentioned at the beginning of section 3.5 that one needs to distinguish between *propagation loss* and *transmission*. In this section, the total transmission through different systems will be investigated. This quantity takes all reflections and losses into account that happen during the incoupling, propagation and outcoupling through a system. After the concept was explained in the following, the transmission spectrum will be calculated for the W1-waveguide, band filters and the grating coupler. For the grating coupler the design will be presented and the transmission calculation will be used to find optimizations for its parameters.

3.6.1 Basic Principle

Again the FDTD method was applied for the investigation, using the capabilities of flux monitors and PMLs. As for the propagation loss computation one needs to be aware of unbound modes and unwanted reflections. Consequently, the technique is quite similar: it uses a Gaussian beam source in a dielectric waveguide and a PML which absorbs the power radiated backwards. In addition, a dielectric waveguide is used after the photonic crystal, leading to outcoupling effects.

In order to find correctly normalized transmission and reflection spectra, one needs to know the complete *incident flux* $\mathcal{T}_{\text{inc}}$. This can only be computed if no power is backscattered after it passed the flux monitor. An easy way to achieve this is to use two simulations: a *normalization simulation* for the incident flux computation and an *actual simulation* for the reflected and transmitted flux computation. Depending on the structure of interest one needs to design both simulations so that the desired spectra can be calculated correctly. In the following, for each of the investigated structures these methods will be explained, respectively.

Above all, it is very important that the source is surrounded by the same dielectric environment to guarantee that it radiates the same power. This is due to the implementation of the sources in MEEP, which has been explained in section 2.2.3.

3.6.2 W1-Waveguide

Figure 3.14 shows the setup of both, the normalization simulation and the actual simulation. In both cases the source is located at the same position in the dielectric waveguide, ensuring to emit the identical power. The length of the first dielectric waveguide l_{dw1} needs to be comparatively long, so that light which is not bound to the waveguide decayed away. A similar scheme was used by Kappeler et al. (2011).

In the simulation which includes the photonic crystal various reflections between the input and the output port of the W1-waveguide take place. This is clear, because there is no PML inside the photonic crystal which could damp the light before it is reflected. Thereby, the simulation must run till most of the oscillating light has decayed (caused by propagation losses). This particular time was determined by doing various simulations, doubling the runtime till the spectrum did not change anymore.

Flux Computations

In the normalization simulation the light passes the monitor M1 and is then absorbed by the $+x$-PML – no measurable reflections occur. The flux registered by M1 is equal to the complete flux that radiates the photonic crystal waveguide input port in the actual simulation, thus

$$\mathcal{T}_{\text{inc}} = \mathcal{T}_{\text{M1}}. \tag{3.8}$$

At the same position as M1 a flux monitor M2 is used in the actual simulation. M2 records the incident flux minus the flux that is reflected by the photonic crystal. Consequently, the

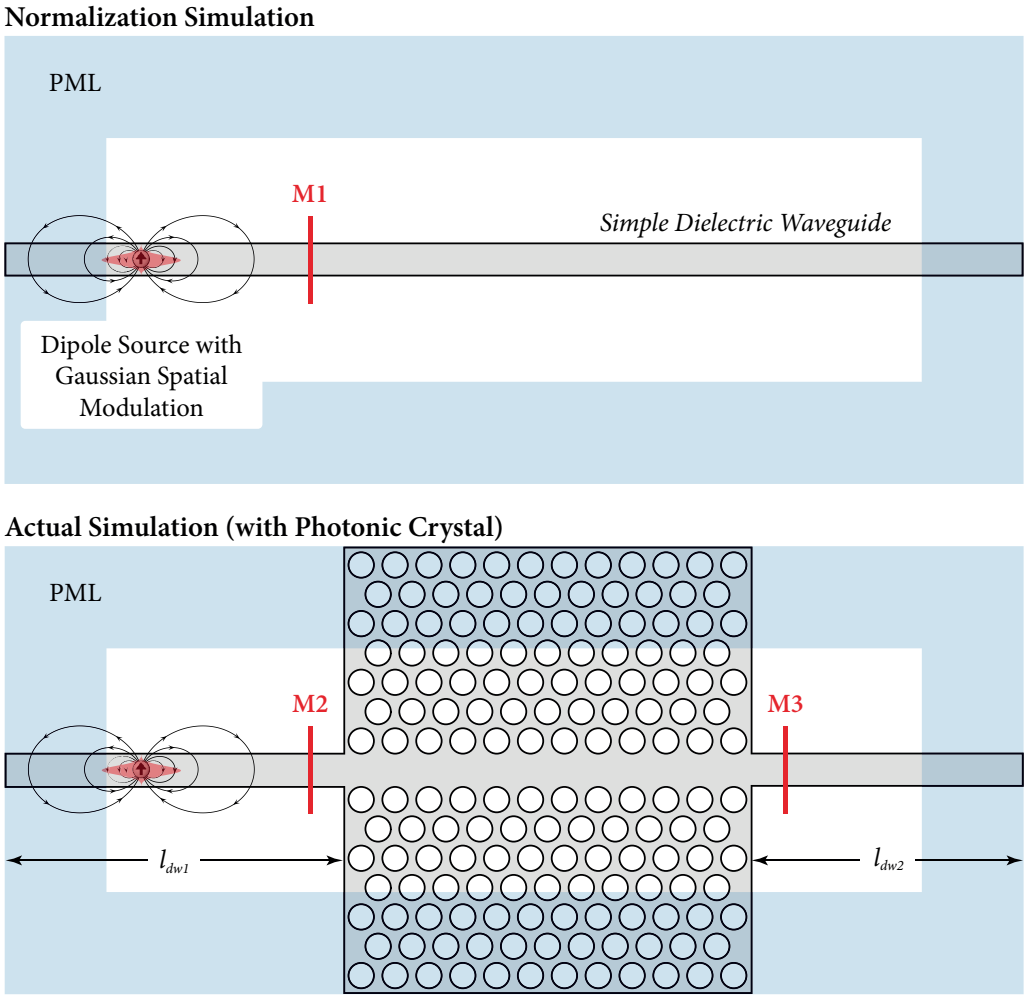

Figure 3.14 | Scheme of the computational method used for the W1-waveguide transmission spectrum calculation. The normalization simulation consists of a simple dielectric waveguide, a Gaussian beam source and a single flux monitor M1, which measures the incident flux. The actual simulation uses the identical domain, source and PML. Monitors are located before and after the photonic crystal, allowing to compute the reflected and transmitted flux afterwards.

reflection R is given by

$$R = \frac{\mathcal{F}_{\mathrm{M1}} - \mathcal{F}_{\mathrm{M2}}}{\mathcal{F}_{\mathrm{M1}}} = \frac{\mathcal{F}_{\mathrm{inc}} - \mathcal{F}_{\mathrm{M2}}}{\mathcal{F}_{\mathrm{inc}}}. \tag{3.9}$$

After the photonic crystal an additional monitor M3 is situated. Only light which propagated through the complete photonic crystal structure can be recorded by M3 and consequently the *transmission* T is given by

$$T = \frac{\mathcal{F}_{\mathrm{M3}}}{\mathcal{F}_{\mathrm{M1}}} = \frac{\mathcal{F}_{\mathrm{M3}}}{\mathcal{F}_{\mathrm{inc}}}. \tag{3.10}$$

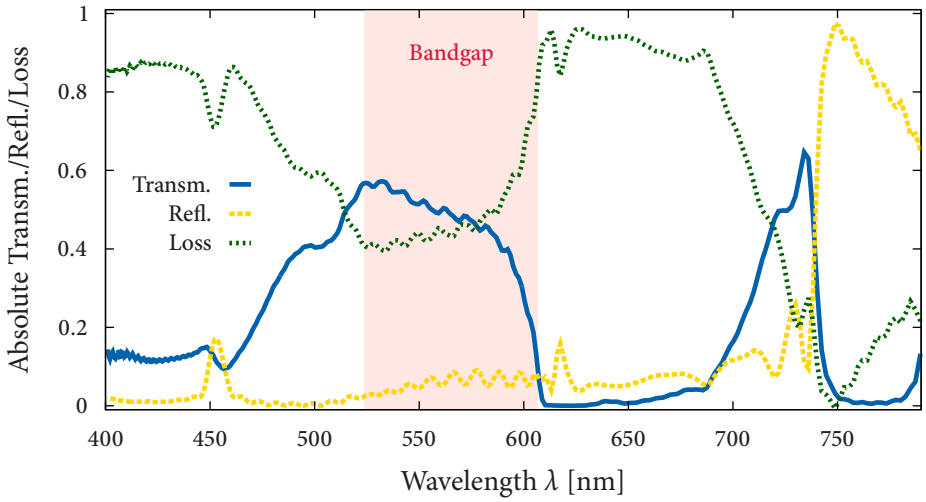

Figure 3.15 | Computed transmission spectrum of the W1-waveguide. Shown are the absolute values of the transmission (red, solid), reflection (yellow, dashed) and loss (green, short dashed). The bandgap is highlighted in light red. No values > 1 or < 0 appear in the data, being evidence of a successful normalization procedure. In addition, the computed loss greatly agrees with the one shown in figure 3.13.

The *loss* L is then simply given by the fraction which is missing in the transmission and reflection spectra

$$L = 1 - |T| - |R|. \tag{3.11}$$

Using equations (3.8) to (3.11) all spectra of interest can be computed using the data of the three monitors M1, M2 and M3.

Analysis of the Transmission Spectrum

Simulations using a resolution of 30 and a waveguide length of 25 lattice constants (equals to 25 columns of holes) resulted in the spectra shown in figure 3.15. There are two areas in the transmission spectrum (blue, solid curve) where the transmission reaches considerably high values of up to 60 %:

- below and inside the bandgap (about 490 to 600 nm) and
- in a range of 710 to 740 nm.

Especially between them near-zero transmission was recorded. The absolute maximum of 64.4 % is located at 734 nm.

In the reflection spectrum (yellow, dashed curve), there are 3 minor peaks between 16 and 25 % at 453 nm, 617 nm and 729 nm, respectively. From about 740 nm the reflection increases strongly, reaching a maximum value of 97.5 % at 749 nm. Consequently, the incoupling works extremely bad in the range of 740 to 790 nm. In the range of the bandgap the incoupling works comparatively well with maximum reflection values of about 8 %.

Regarding the loss spectrum, one observes an analog behavior to the one shown in figure 3.13. This is to be expected, since the main losses that occur from monitor M1 to M3 are

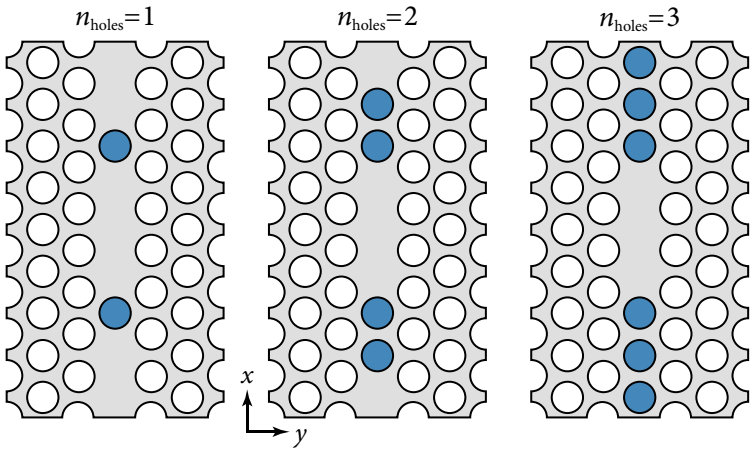

Figure 3.16 | Examples for filters using the L3-cavity. The L3-filter is an L3-cavity inside the W1-waveguide. It is coupled to the waveguide with a varying number of holes (n_{holes}). Shown are the three investigated cases of n_{holes} = 1, 2 and 3.

propagation losses in the W1. The similarities will be further discussed in section 5.3 of chapter 5. Inside the bandgap, the losses reach a local minimum of about 39 % at 533 nm. From 690 nm on the losses decrease rapidly, reaching near-zero at ~ 749 nm.

3.6.3 Filters

An identical technique as in section 3.6.2 can be applied to filters. Both simulations stay the same as in figure 3.14, except in the actual simulation an L3-cavity is included at the center of the W1-waveguide. The cavity is coupled to the waveguide symmetrically with a variable number of holes (n_{holes}), controlling the filtering strength. A sketch of the three studied cases n_{holes} = 1, 2 and 3 is shown in figure 3.16. The holes which are used to couple to the waveguide are highlighted in blue.

For the case of an *ideal coupling* between waveguide and cavity plus an *ideal L3-resonator*, one would expect zero transmission through the filter in the region of the photonic bandgap except for those wavelengths where the cavity modes lie. At these wavelengths Lorentzian peaks should appear, having a full width at half maximum (FWHM) inversely proportional to the cavity's Q-factors. In the real case increasing n_{holes} improves the resonator quality, but worsens the coupling and vice versa.

The computed transmission spectra for these filters are plotted in figure 3.17. The filters are mainly influencing the region of the photonic bandgap (light-red), as expected. For shorter wavelength the transmission gets worse when adding more holes, probably because of high propagation losses inside the waveguide during the back and forth reflection between resonator and input port. For wavelength larger then the bandgap the transmission looks similar to the one of the empty W1-waveguide (figure 3.15).

Inside the photonic bandgap the transmission decreases strongly with growing n_{holes}, reaching near-zero for n_{holes} = 3. Nevertheless, there are peaks near the computed L3-cavity

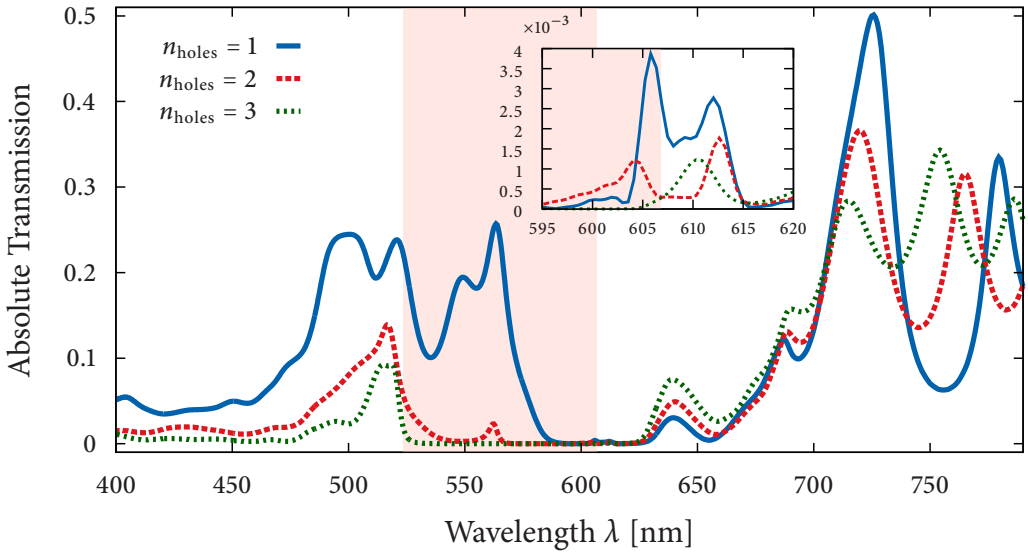

Figure 3.17 | Transmission spectra for L3-filters. Transmission spectra for the three studied L3-filters with n_{holes} = 1 (blue, solid), 2 (red, dashed) and 3 (green, short dashed). Inside the bandgap (light red) the transmission decreases strongly for larger n_{holes}. Peaks are visible near the L3-resonance wavelengths of about 565 and 607 nm (compare to table 3.1). The inset shows a zoom to the edge of the bandgap.

resonance wavelength of table 3.1, namely at about 565 and 607 nm (notice the zoomed inset in figure 3.17). For n_{holes} = 1 and 2 these modes seem to split into a larger number of modes having wavelengths near the calculated ones of the L3-cavity – leading to numerous peaks. Furthermore, the peaks are getting narrower (corresponding to larger Q-values) and the amplitudes of the peaks are shrinking. The shrinking is again due to the worsened coupling between waveguide and cavity. It has been reported by Faraon et al. (2007), that a 60°-tilt of the cavity can be used to improve the coupling, yielding efficiencies up to 90 %.

A Lorentzian fit of the n_{holes}=3–peak at about 610nm (see the inset in the figure, green dashed line) resulted in a Q-factor of 124 – a reasonable result, since this mode showed a Q of 380 for the plain L3-cavity.

3.6.4 The Grating Coupler

For many applications, efficient vertical outcoupling from the photonic crystal sample will be needed, as has been stated in the introduction (chapter 1). To this end, the photonic crystal waveguide needs to be terminated with some sort of scatterer, directing as much light as possible out of the photonic crystal plane. Two basic quantities need to be studied in order to find out if a coupler design works properly. These are

1. the *efficiency* – which fraction of the input power does the coupler scatter to the desired direction; and
2. the *directivity* – how does the angular distribution look like in the far-field?

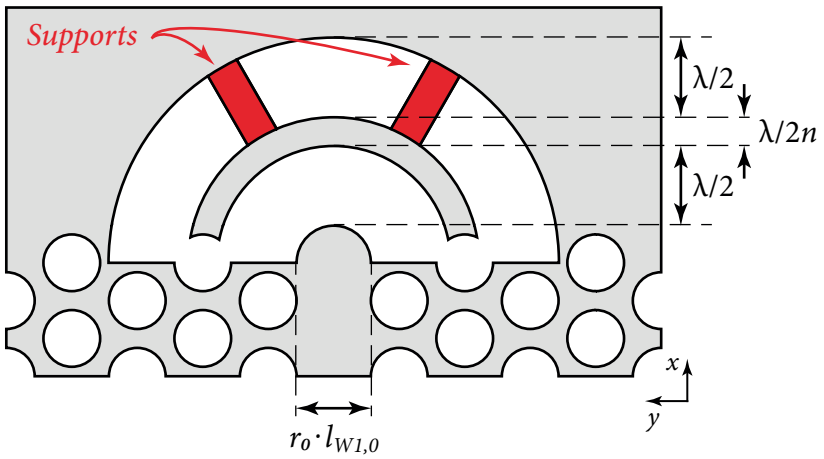

Figure 3.18 | Design of the grating outcoupler. The coupler is formed by two concentric (air-) half-rings of width $\lambda/2$, separated by $\lambda/2n$. Design parameters are the x-position (defaulting to the center of the last photonic crystal hole) and the most inner dielectric circle diameter $r_0 l_{W1,0}$. The outer ring can be stabilized by supports (shown in red) consisting of the dielectric material.

Additional features are the tunability and the bandwidth for which the coupler works efficiently.

The mentioned properties are more difficult to investigate than the ones studied so far – like the transmission of a W1-waveguide for example. Again, theoretically all of them can be analyzed using the FDTD-method – the efficiency inside the photonic bandgap will be calculated in this section. Although to study the angular distribution a *Near- to Far-Field Transformation* needs to be applied, which is not yet implemented in the used FDTD-software MEEP. Details to this technique can be found in the appendix, section A.2.

The Coupler Design

A specific design for a vertical outcoupler was presented by Faraon et al. (2008) and uses a grating for the scattering process. This design, which is sketched in figure 3.18, was used throughout this thesis – including the measurements presented in chapter 4. It was a fundamental task for the presented work to quantify the important measures (efficiency and directivity), both numerically and with real measurements.

The coupler is formed by two concentric half-rings of width $\lambda/2$ consisting of air, which are separated by $\lambda/2n$. The quantity λ was presented as a *tuning wavelength* by Faraon et al. – a fact that will be proved in the progress of this thesis. The rings are located at the end of the W1-waveguide, centered at the middle of the final hole of the photonic crystal in x-direction. The first optimization parameter is thus the x-shift Δx. The most inner dielectric circle has a default diameter equaling the width of the W1-waveguide $l_{W1,0}$. Consequently, a second design parameter is the factor r_0, scaling this inner circle diameter.

As a consequence of this design the whole coupler grows or shrinks when adjusting the tuning wavelength λ or the inner ring scaling factor r_0. For some constellations the dielectric ring separating the air-rings looses its contact to the slab, as shown in figure 3.18. For that purpose additional supports (highlighted in red) are used to guarantee the

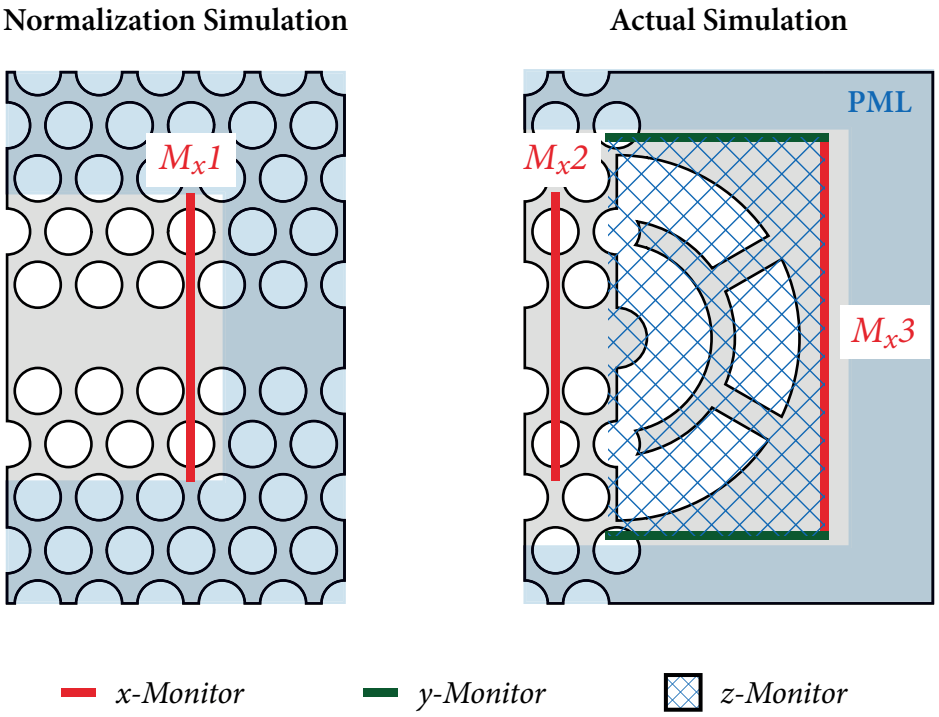

Figure 3.19 | Scheme for the transmission calculation for the grating coupler. For the normalization simulation the W1-waveguide reaches into the PML. The monitor M_x1 records the incident flux. In the actual simulation, the coupler is surrounded by a monitor-box. M_x2 is used to compute the reflected flux and the M_{+z}-monitor (blue hatched) for the transmitted flux.

stability of this ring. They consist of the slab material and are chosen to cover an angle of $\pi/20$ (measured at the largest circle).

Computational Method for the Transmission Calculation

The computational procedure for the computation of the absolute transmission is similar to the one used for the W1-waveguide. As before, one needs a normalization simulation to compute the incident flux and an actual simulation for the scattered flux. Both are using a dielectric waveguide for the incoupling process which is long enough for the radiating modes to decay and a Gaussian beam source at the same point to guarantee an identical emission.

Different in this case is, that the transmission of interest is composed of the flux scattered to $(+)z$-direction $\mathcal{T}_z$ divided by the complete flux that reaches the outcoupling structure. Accordingly, the *normalization simulation* already needs the W1-waveguide with a flux monitor at the coupler position. This waveguide needs to be continued into the PML to eliminate back reflections. A sketch of the interesting part of the computational domain is shown in figure 3.19 (left). As can be seen, the flux monitor M_x1 records the *complete incident power*,

$$\mathcal{T}_{\text{inc}} = \mathcal{T}_{M_x1}. \tag{3.12}$$

On the right hand side of figure 3.19 the interesting region of the *actual simulation* is depicted (note that in the real simulation, the computational domains are larger and the PML has the same thickness in both cases). Red lines correspond to $\mathcal{F}_x$-monitors, green lines to $\mathcal{F}_y$-monitors and the blue hatched region to an $\mathcal{F}_z$-monitor. Monitor M_x2 records all the incoming minus the back-reflected power, thus the reflection can be computed as

$$R = \frac{\mathcal{F}_{\mathrm{M_x1}} - \mathcal{F}_{\mathrm{M_x2}}}{\mathcal{F}_{\mathrm{M_x1}}} = \frac{\mathcal{F}_{\mathrm{inc}} - \mathcal{F}_{\mathrm{M_x2}}}{\mathcal{F}_{\mathrm{inc}}}. \tag{3.13}$$

Of course, one has to assure that M_x1 and M_x2 are located (at least nearly) at the same position. For applications one can exclusively use light which is scattered into one direction, + or $-z$. Since the structure exhibits a mirror symmetry relative to the x-y-plane the coupler always scatters the same power to both directions. Consequently, the maximum transmission to $+z$-direction that can be reached using this design is 50 %.

In the actual simulation the coupler is completely surrounded by flux monitors, recording all the power radiated by the coupler to x-, y- or z-direction. This monitor box has a fixed distance to the coupler in each direction, hence the M_{+z} monitor is located above the slab. The *transmission* can be defined as

$$T = \frac{\mathcal{F}_{\mathrm{M_{+z}}}}{\mathcal{F}_{\mathrm{M_x1}}} = \frac{\mathcal{F}_{\mathrm{M_{+z}}}}{\mathcal{F}_{\mathrm{inc}}}. \tag{3.14}$$

Way of Validation: The Check Sum

The additional monitors that are shown in figure 3.19 (right) are used to compute a *check sum* and thus to validate which points in the final transmission spectrum are trustworthy. In both simulations the identical power enters the W1-waveguide and this power is completely recorded in the normalization simulation. In the actual simulation this power can only be

1. reflected back to the waveguide – it then may oscillate between the coupler and the input port of the photonic crystal – or
2. scattered by the coupler to x-, y- or z-direction, respectively. If this case occurs the light will pass one of the monitors of the box and will then be absorbed by the PML.

For that reason, the equation

$$1 = \frac{|R| + |\mathcal{F}_{M_x3}| + 2\left|\mathcal{F}_{M_{+y}} + \mathcal{F}_{M_{+z}}\right|}{\mathcal{F}_{\mathrm{inc}}} \tag{3.15}$$

must be satisfied for each frequency of the spectrum. It thus acts as a *check sum* – only frequencies for which this equation is fulfilled with a given tolerance are treated as valid points. The factor 2 in the equation counts for the fact that in all simulations symmetries in y- and z-direction have been applied, so that the conditions

$$|\mathcal{F}_{M_{+y}}| = |\mathcal{F}_{M_{-y}}| \quad \text{and} \quad |\mathcal{F}_{M_{+z}}| = |\mathcal{F}_{M_{-z}}| \tag{3.16}$$

are true in all cases.

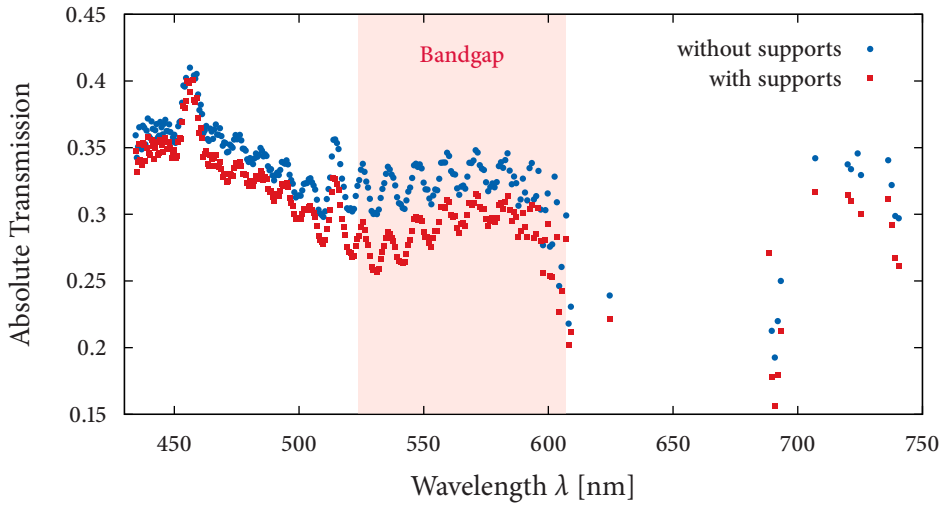

Figure 3.20 | Computed transmission spectra for grating couplers. Absolute transmission for a coupler without (blue dots) and with (red squares) supports, both having a tuning-wavelength of 640 nm. The bandgap is highlighted in red. Shown are only points for which the check sum (equation (3.15)) is fulfilled with a tolerance of ±10 %. The supports lower the in-gap efficiency from 32 to 28.7 %.

Efficiency

It may depend on the particular application one desires to use which definition of *efficiency* is appropriate. As most applications using photonic crystal waveguides and resonators focus on the region of the photonic bandgap, it seemed reasonable to choose a measure which is closely related to this frequency range. Accordingly, for a bandgap spreading from λ_i to λ_f the efficiency was defined as

$$\mathcal{E} = \frac{1}{\lambda_f - \lambda_i} \int_{\lambda_i}^{\lambda_f} T \, \mathrm{d}\lambda. \tag{3.17}$$

This quantity gives no information about the directivity of the coupler, since the $\mathcal{F}_z$-monitor is very close to the slab and thus collects information from approximately all scattering angles.

Transmission Spectrum and Influence of the Supports

The coupler has been simulated with its default parameters ($r_0 = 1$, $\Delta x = 0$, see figure 3.18) and a tuning wavelength of 640 nm, due to the produced chip which will be presented in chapter 4. The results for the transmission calculation are shown in figure 3.20, both for the case without (blue dots) and with (red squares) supports. Only points that fulfilled the check sum (3.15) with a tolerance of ±10 % are shown.

The shape of both curves is qualitatively equal. There is a maximum peak at ~ 457 nm followed by a rather stable section with values between 0.25 and 0.36 till the end of the bandgap. On the entire section an oscillation with a wavelength of about 11 nm is present. Directly behind the bandgap no valid points were calculated, since the W1-waveguide has

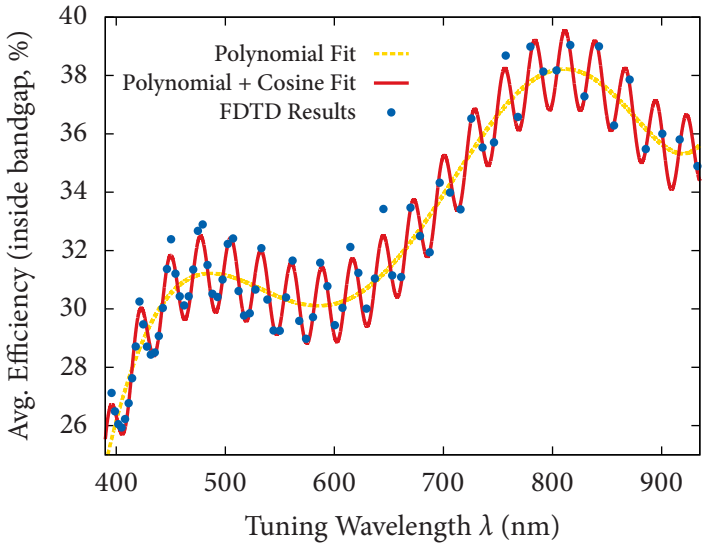

Figure 3.21 | Relationship between efficiency and tuning wavelength. Results for the efficiency of the coupler as computed by FDTD-simulations (blue dots) as a function of the tuning wavelength. The red line shows a 6th degree polynomial fit plus cosine modulation, revealing a oscillation wavelength of 27.85 nm. The yellow dashed curve shows the pure polynomial contribution. The maximum of ~ 40 % is reached at 810 nm, while the gap center is located at 566 nm.

very small transmission values in this part (compare to figure 3.15). From 690 nm on there again are valid points reaching transmission values of up to 0.33.

The supports seem to apply an overall decrease in the transmission of 10–20 %. The efficiency calculation, as defined in equation (3.17), resulted in

$$\mathcal{E} = 32.0\,\% \quad \text{and} \quad \mathcal{E}_{\text{supports}} = 28.7\,\%.$$

Relationship between Efficiency and Tuning Wavelength

As it was stated in the paragraph *The Coupler Design* the radii and separation of the two half-rings forming the coupler correspond to a wavelength λ, which should have an influence on the tuning of the coupler. To study if this tuning-wavelength has an influence on the efficiency – as one would expect – numerous simulations for different tuning wavelength have been done. For each of the simulations the efficiency was calculated as before. Since this quantity is more or less the averaged transmission inside the photonic bandgap one would expect an optimum for a tuning wavelength lying in the center of the gap.

Figure 3.21 shows the efficiency as a function of the tuning wavelength $\mathcal{E}(\lambda_{\text{tune}})$ – blue dots show the calculated results. The values exhibit an oscillatory behavior with a wavelength of $\lambda_{\text{osc}} = 27.85$ nm on a background which was successfully fitted using a polynomial of 6th degree. The yellow dashed line shows the pure polynomial fit, the red one the complete fit of polynomial plus cosine modulation.

As before, the bandgap ranges from about 524 nm to 607 nm, thus the center of the bandgap is at about 566 nm. Obviously, there is no sort of maximum at this wavelength,

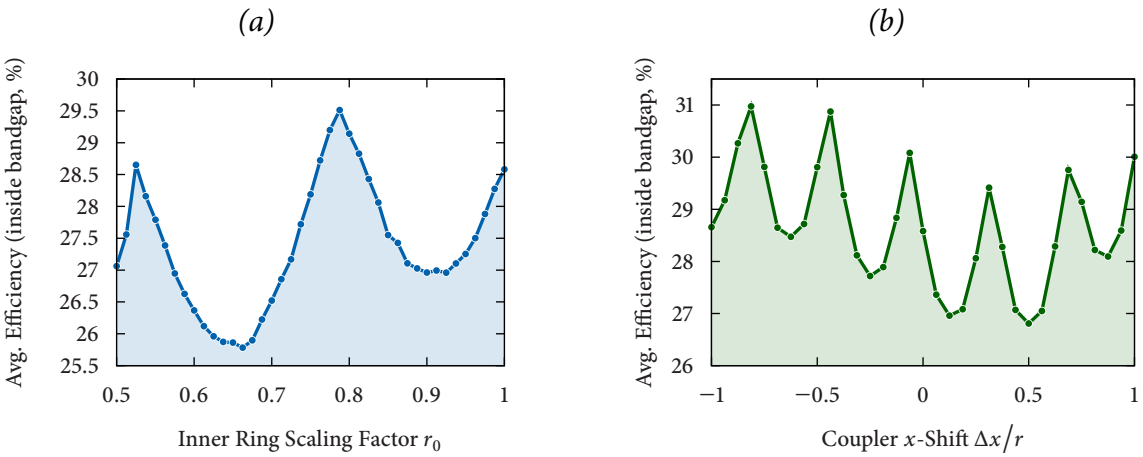

Figure 3.22 | Design optimizations for the grating coupler. (a) Variation of the inner circle diameter, showing a maximum efficiency of 29.5 % at $r_0 = 0.78$. (b) Results for the $\pm 1r$-shift of the coupler with a larger improvement than for the inner ring modification, having a maximum of 31 % at $\Delta x/r = -0.81$.

although a satisfying efficiency of 30 % is reached. The absolute maximum is reached at about 810 nm with almost 40 % – far off the bandgap center.

Therefore, the tuning wavelength does not tune the coupler in view of maximum z-scattering. Since longer tuning wavelengths lead to a larger coupler the light just hits a larger scatterer, which is probably the reason for the observed improvement.

Coupler Design Optimizations

As a final numerical investigation the influence of the two design parameters r_0 and Δx was studied using the same technique as in the previous paragraph. The coupler was simulated for a tuning wavelength of $\lambda_{\text{tune}} = 640$ nm *with supports*.

The results for both investigations are plotted in figure 3.22. For figure 3.22a the inner ring diameter of the coupler has been scaled down till $r_0 = 0.5$. The values are varying in the range of 25.8 ($r_0 = 0.66$) to 29.5 % ($r_0 = 0.78$). Accordingly, an improvement of roughly 3 % can be achieved in comparison to the default value.

In figure 3.22b the coupler has been shifted from the $-x$-end of the final hole to the $+x$-end, equaling to a total shift of one hole-diameter. The achievable improvement is slightly higher than for the r_0-variation. The efficiencies range from 26.8 to 31.0 % (at $\Delta x/r = -0.81$), corresponding to an improvement of about 7 %.

4 Results Part II: Experimental Results

After having presented all of the results that were achievable by numerical simulations, the present chapter focuses on true *experiments*. Using computations and real physical measurements together leads not only to a more efficient workflow, but also offers a way of validation. Both approaches have their own uncertainties and limits and thus they add up canceling the disadvantages of the other one if used reasonable – forming a couple stronger than the sum of its parts.

In this couple the numerics take on the role of a design-tool before any productions need to be executed – they provide the option to *optimize* a system-parameter under stable conditions without producing vast quantities of samples. Additionally, they feature the *verification* of measured results after the experiments, for example to distinguish between physical effects introduced by the system of interest and systematic errors being specific to the measurement setup.

The experiments constitute the connection to real applications, showing which issues have to be considered arising from production processes or detection mechanisms. For measurements on photonic crystals one needs to take care of the production process itself and of a chip design which allows to in- and output the light in a consistent way – enabling comparable measurements for all photonic crystals on the chip. Consequently, this chapter covers a brief introduction to the production process, the chip design, the measurement setup and the results that have been achieved in this fashion. Comparisons to numerical results will be covered in detail in chapter 5.

4.1 Production of Photonic Crystals

Photonic crystals must largely be produced under cleanroom-conditions, using numerous highly specialized machines which are rarely available at universities. For that reason these processes have been executed at the *Optical Technology* workgroup, belonging to the *Institute for Nanometer Optics and Technology* at the *Helmholtz-Center Berlin for Materials and Energy*.

The techniques used in these laboratories are optimized for silicon nitride (Si_3N_4, abbreviated in the following as SiN) – a material which is well suited to the production of photonic crystals. This is due to the following qualities (compare to Barth (2010) and Nüsse (2011)):

- The refractive index of $n \approx 2$ (see figure 4.1 for the refractive index as a function of wavelength) is high enough to achieve large bandgaps and thus good quality factors in resonators, as has been shown in chapter 3.

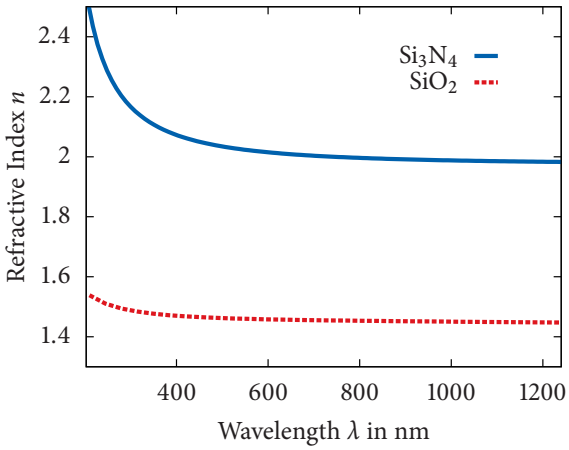

Figure 4.1 | Refractive index of silicon nitride and silicon oxide. In the visible spectrum $n \approx 2$ is a good approximation for SiN, while for ultraviolet light higher indices occur. SiO_2 is shown for completeness. Data was received at January 15, 2014; `http://refractiveindex.info`.

- SiN can easily be structured using standard complementary metal-oxide semiconductor technology (CMOS).
- In addition, using its intrinsic luminescence one can excite a high-bandwidth fluorescence with standard lasers and thus investigate resonators by measuring the emission spectrum.

The structuring process will be explained in the following – providing only an overview. Since most of the used techniques have been worked out by former PhD-students at the Helmholtz-Center Berlin, much more detailed explanations can be found in the accompanying theses ((Kouba 2008) and (Nüsse 2011)).

4.1.1 Basic Process

Figure 4.2 shows the five steps which are necessary for the production process. The basis is formed by a 4"-⟨100⟩-silicon wafer of 525 µm thickness with a 2.2 µm layer of thermally grown silicon oxide (SiO_2). The SiO_2 acts as a sacrificial layer as the desired product is a SiN-slab which is surrounded by air. The SiN layer – which is grown by low pressure chemical vapor deposition – forms the final layer of the wafer, which is delivered in this form by the manufacturer. Since the thickness of the SiN layer is of great importance for the comparison simulations (especially after the etching process), it was further investigated by X-ray reflectivity measurements (see the appendix, section A.4) resulting in an initial thickness of 230 ± 1 nm.

In step (a) this substrate is completely covered by a resist with 330 nm layer thickness using *spin coating*. The resist material, known as ZEP, is a highly specialized liquid with a well-suited viscosity and an incredibly stable exposition behavior. The resist is of great importance as it acts as the medium for the structuring information. This information – the chip design – needs to be modeled before using computer-aided design (CAD) software. In detail, the python module *GDSpy* (`http://gdspy.sourceforge.net/`) was used to write a parameterized program which creates the desired CAD-file.

The structuring is then done in step (b) using *electron beam lithography* with the 100 kV Vistec EBPG 5000+. All parts which should later be composed of air correspond to exposed

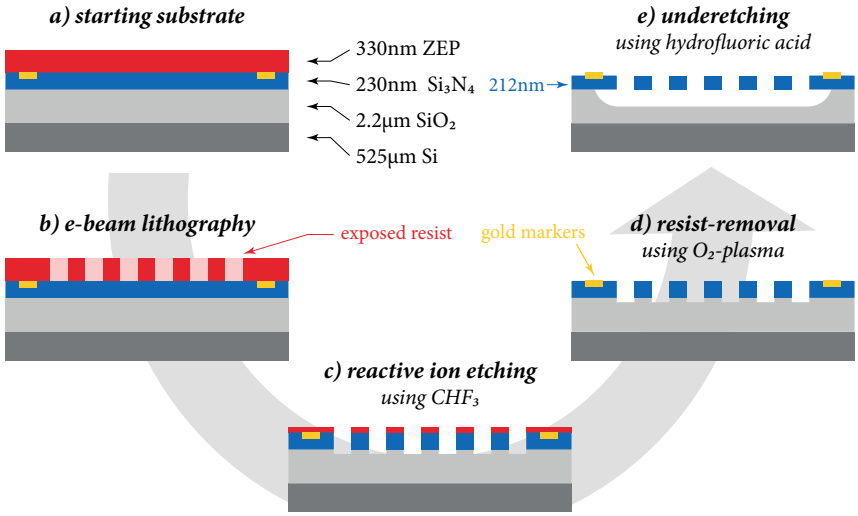

Figure 4.2 | Steps in the production process of silicon nitride photonic crystals. (a) Layers of the SiN-SiO-Si wafer which were covered with a 330 nm-resist (ZEP) by spin coating. For overlay designs additional 60 nm gold markers are necessary, which can be produced with the process described in figure 4.3. (b) The exposition of the resist is done by electron beam lithography using 100 kV Vistec EBPG 5000+. (c) The SiN-layer is structured by reactive ion etching using Oxford Plasmalab 80+, residuals of the resist are removed in a cleaning run using O_2-plasma (d). (e) Finally the chip is underetched using HF to obtain a structured SiN-layer surrounded by air.

regions in the resist. Exposed (and developed) parts are then affected when *reactive ion etching* is applied in step (c), using CHF_3 in an Oxford Plasmalab 80+. This way, the SiN-layer is completely etched through, while the unexposed resist protects the parts which should remain.

Remnants of the unexposed resist are removed with the help of an *oxygen-plasma* in step (d) – resulting in a ready-structured SiN-layer representing the former design. To finally achieve the air-surrounded sample, the complete wafer is suspended in a bath of hydrofluoric acid (50 % HF, 50 % H_2O). The SiO_2-layer is etched comparatively fast, leading to an *underetching* of great parts of the SiN-substrate. The SiN itself is thinned out during this process. The thickness has again been measured utilizing X-ray reflectivity, showing a final thickness of 212 ± 1 nm (see section A.4).

A feature shown in figure 4.2 which has not been explained yet are *gold markers*, as they have been unnecessary for the previously described process. Leaving out these markers, the procedure above can only be applied if all structures can be written in a *single e-beam run*. For all other cases the overlay process must be used.

4.1.2 Overlay Process

If the e-beam step should be applied multiple times, the e-beam writer must be able to locate where earlier written structures lie on the surface to align subsequent layers. This might be needed for example if parts of the SiN should not be completely etched through

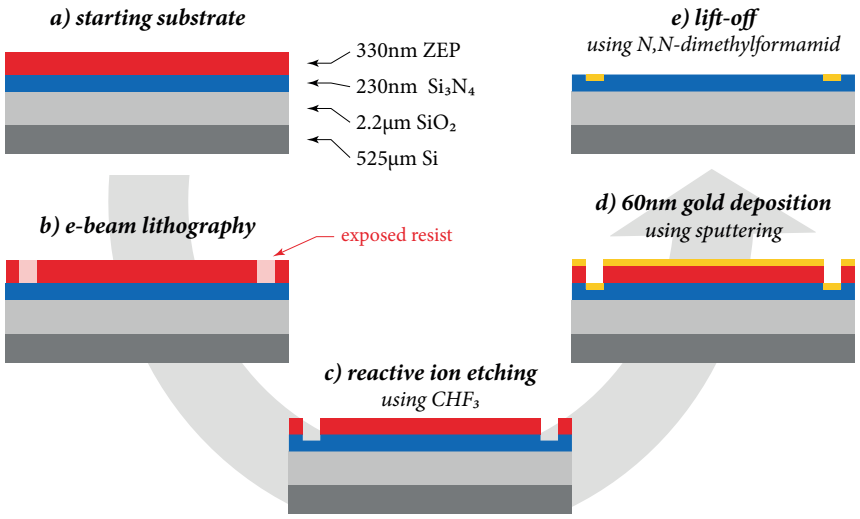

Figure 4.3 | Steps in the marker deposition process for overlay designs. (a) Layers of the SiN-SiO-Si wafer which were covered with a 330 nm-resist (ZEP) by spin coating. (b) The exposition of the resist is done by e-beam lithography. (c) By reactive ion etching pits for the gold markers are created, which are filled (d) with 60 nm of gold by sputtering. (e) The resist and the gold layer on top of it are removed by lift-off.

or if any other manipulations should only be applied to parts of the chip. These techniques are referred to as *overlay processes*.

For that purpose gold markers are used, which are arrays of gold squares positioned at four locations on the chip, in most cases. They have to be placed on the chip in a previous process, depicted in figure 4.3. Steps (a)-(c) are basically identical to the main process, except that the SiN is not completely etched through. A 60 nm coating of gold is then sputtered on top of the remaining resist in (d), reaching the SiN-substrate only at regions where the resist was developed before. Using N,N-dimethylformamid the excessive gold and the resist are then lifted off in step (e). After the marker deposition the main structuring process of figure 4.2 can be applied multiple times. Just before each e-beam lithography step the e-beam writer locates these markers semi-automatically and aligns the pattern origin according to the marker positions on the substrate.

4.2 Produced Optical Chip

A crucial part in the development of the measurement process is the chip design. The chip has to fulfill several requirements in order to enable the measurement of the desired quantities. The most important demands are

1. effective in- and outcoupling to the chip using a laser source,
2. outcoupling both for in-plane and out-of-plane transmission channels,
3. single mode excitation of the photonic crystal samples to avoid dispersion effects.

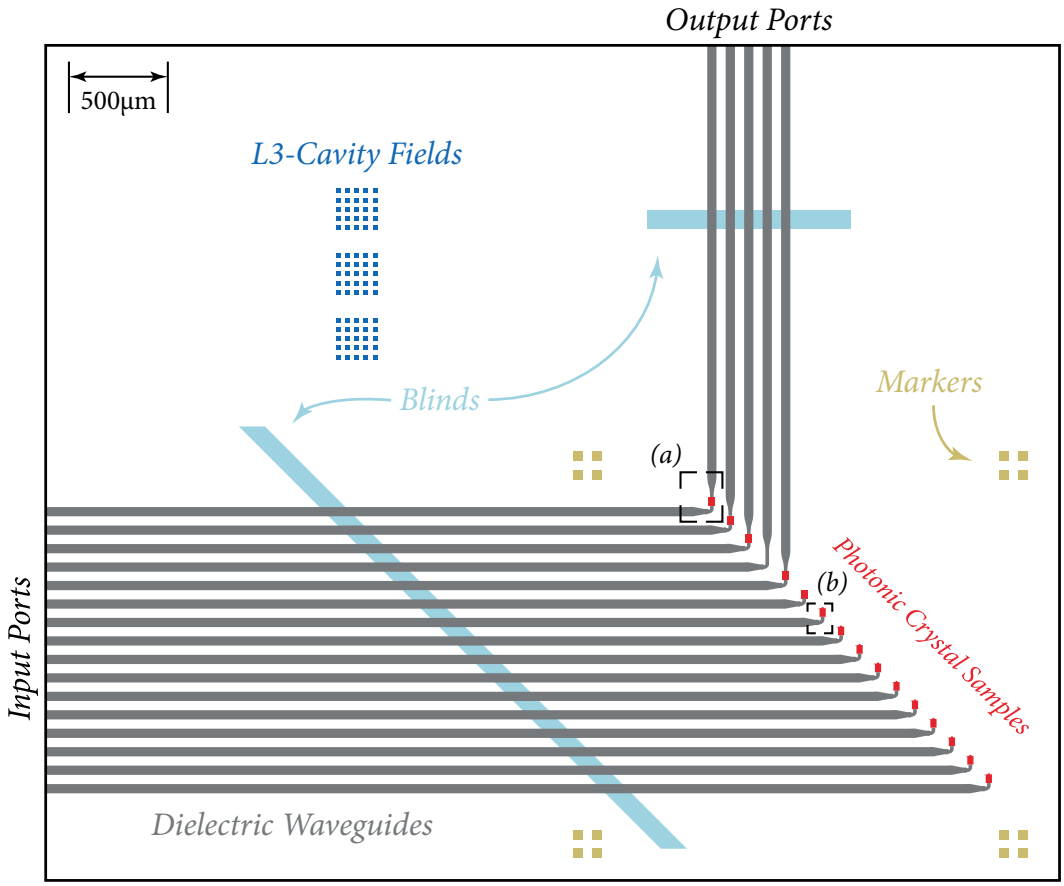

Figure 4.4 | Chip design for measurements on photonic crystals. Shown is a *sketch* of the complete chip design – on the real chip, in- and output dielectric waveguides are considerably longer and all channels are repeated for comparative measurements. Dielectric waveguides (gray) are used to guide light from the input ports to the photonic crystal samples (red). Blinds (light blue) prevent light inserted between input ports from reaching the samples. Additional L3-cavity fields are shown in (dark blue), each field being composed of 25 photonic crystals with resonators. Sandy rectangles correspond to the gold markers, the black outline shows the true borders of the chip. The two parts which are surrounded by dashed black lines and marked by (a) and (b) are zoomed in figure 4.5.

The design which was modeled to this end is conceptually sketched in figures 4.4 and 4.5. The former shows an *overview of the complete chip* which is basically composed of *transmission channels*, *blinds* and L3-cavity fields. Each transmission channel consists of a dielectric input waveguide, a (photonic crystal) sample and an optional dielectric output waveguide. The blinds – which are air gaps in the silicon nitride – prevent light which was coupled into SiN-regions from reaching the actual samples.

Concepts of the chosen Design

For comparative measurements numerous L3-cavities have been placed on the chip as well. Additionally shown are the locations of gold markers, which would be used for overlay

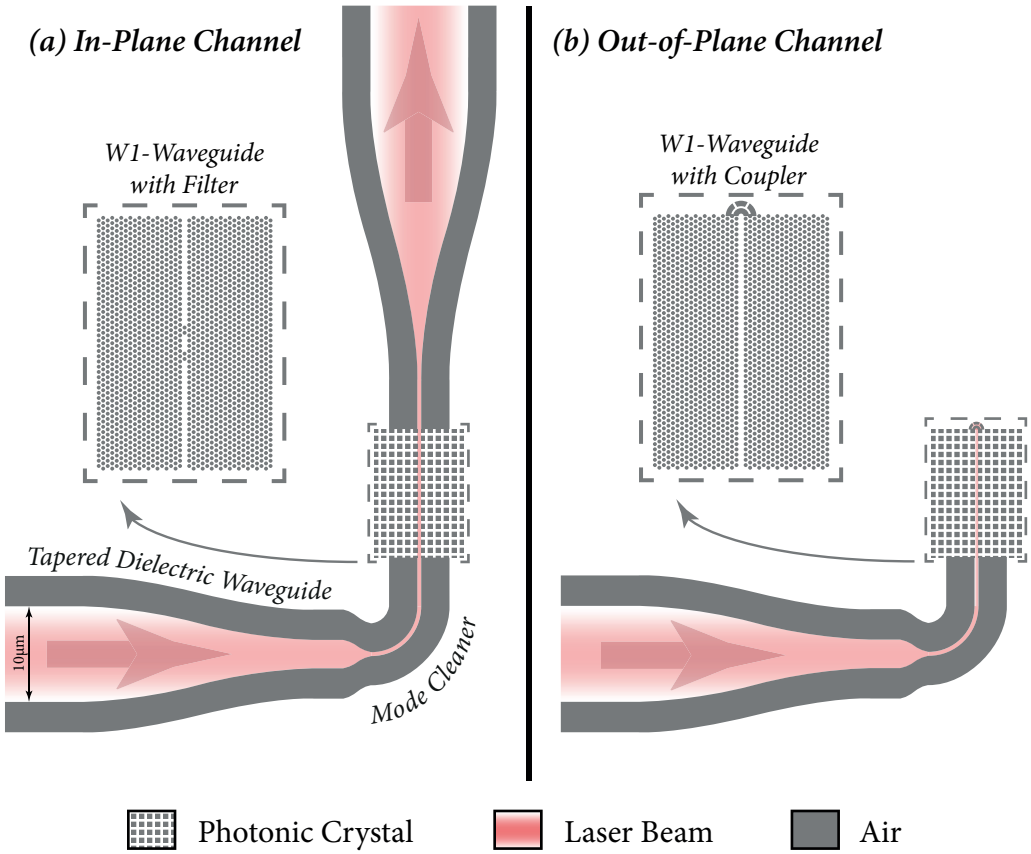

Figure 4.5 | Zoom of photonic crystal sample regions for both types of transmission channels. Enlargements of the highlighted regions (a) and (b) of figure 4.4 – giving examples for in-plane and out-of-plane transmission channels. White areas correspond to SiN, gray areas to air. Light is guided to the sample using a tapered dielectric waveguide with a final width of 300 nm. A 90° curve acts as a mode cleaner. The in-plane channel is terminated using a back-tapered dielectric waveguide, while the out-of-plane channel is terminated using the grating coupler.

processes. The actual chip is larger than in the picture, because the dielectric waveguides have about twice of the shown length and all channels are repeated as a precaution.

Figure 4.5 depicts a zoom of the two samples which are marked by *(a)* and *(b)* and surrounded by dashed rectangles in figure 4.4 – setting examples for *in-plane* and *out-of-plane* transmission channels. In both cases, the incoming dielectric waveguide is tapered in two steps from 10 µm to a final width of 300 nm. This way the tapering occurs smoothly but guarantees enough stability for the adjacent mode cleaner. The considerably wide 10 µm-waveguide is multi mode and can easily be observed at the chip and ensures easy incoupling (demand 3 from above). The 300 nm-waveguide is single mode according to demand 2. Additionally, the *mode cleaner* serves for the dissemination of unwanted modes.

The in-plane channels are terminated by a back-tapered dielectric waveguide with a final width of 10 µm, reaching till the cleaving edge of the complete chip. Together, the in- and outcoupling dielectric waveguides fulfill demand 1 from above. The out-of-plane channels

are terminated using either an abrupt ending of the photonic crystal or the outcoupler.

4.2.1 Overview of Channel Purposes

Each of the channels has a unique sample denoted by red rectangles in figure 4.4. The precise description for each of the samples can be found in table 4.1, where the channels have been numbered in ascending order of the input dielectric waveguides from top to bottom. The table also gives the information about whether it is an in-plane or an out-of-plane channel.

The first five channels are intended for in-plane-measurements. They include three different L3-filters (compare to 3.16) with 1, 2 and 3 hole separation, a pure dielectric waveguide of approximately the same width as the W1-waveguide (300 nm) and a W1-waveguide.

Channels 6–16 are out-of-plane type, offering different examples for outcouplers. The first one is a W1-waveguide which is just terminated abruptly, the other ones implement the different parameter variations as they have been investigated numerically in paragraph *Coupler Design Optimizations* of section 3.6 (see figure 3.22).

Using these different channel designs, it was expected to be able to measure

- the difference in transmission of a dielectric and a W1-waveguide, as it was investigated numerically in section 3.6 (figure 3.15),
- the transmission of different filters in comparison to the W1-spectra (numerically in figure 3.17),
- and the coupling efficiency and angular distribution of the grating outcoupler, both for naively terminated waveguides and different coupler variations.

Chan. nr.	Sample description	Channel type
1–3	L3-filters with 1, 2 and 3 holes for the coupling to the W1-waveguide, respectively	in-plane
4	dielectric waveguide of 300 nm width (without photonic crystal)	in-plane
5	W1-waveguide	in-plane
6	abruptly ending photonic crystal with W1-waveguide	out-of-plane
7-11	W1-waveguide terminated by grating coupler, with linearly spaced parameter variation of $\Delta x/r$ from −1 to 1	out-of-plane
12-16	W1-waveguide terminated by grating coupler, with linearly spaced parameter variation of r_0 from 0.5 to 0.9	out-of-plane

Table 4.1 | Descriptions of the samples used in the design. The channels are numbered after the input dielectric waveguides from top to bottom in figure 4.4.

4.3 Fluorescence Measurements on the L3-Cavities

For testing purposes there are also fields of L3-cavities on the chip. The basic idea was to validate the production process by investigating the mode wavelength, which have been stably computed by FDTD-simulations (section 3.3.2). If a good agreement is found the simulations are certainly useful for the comparison to the measured results for quantities which are not that well known, such as transmission spectra and efficiencies.

4.3.1 Measurement Principle

Mode wavelength and Q-factors of photonic crystal cavities are most easily quantified by *fluorescence measurements*. A simplified scheme is depicted in figure 4.6. The L3-cavity is illuminated using an intense 532 nm-laser beam (~ 300 µW) through an high numerical aperture objective (NA = 0.9). Accordingly, the material starts to fluoresce and modes are excited inside the resonator.

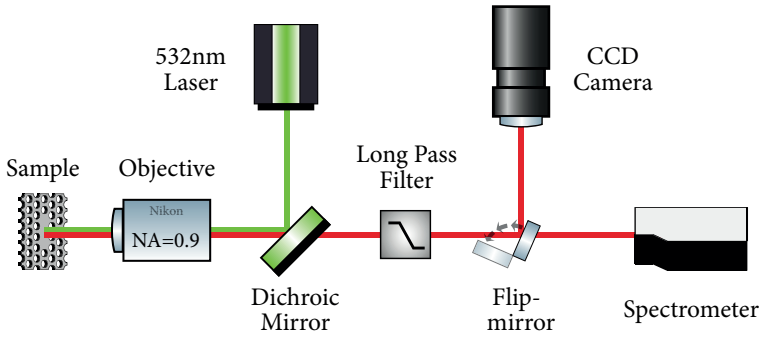

Figure 4.6 | Principle setup for fluorescence measurements. An intense, narrow-band laser beam is directed onto the chip using a high-NA objective to excite fluorescence inside the L3-cavity. Light emitted by the resonator is collected and separated from the laser radiation to be detected on a sensitive spectrometer. Locating is done with a CCD-camera and a white light source (not shown).

The fluorescence light is collected through the same objective (red line in the figure) and separated using a proper dichroic mirror and a long pass filter for suppression of the excitation laser. With the help of a sensitive spectrometer with a liquid nitrogen cooled CCD-camera the fluorescence light is analyzed. Not shown for simplicity is a white light (LED) illumination used to locate the desired structures on the chip. Both, the laser and the white light are therefore guided to a CCD-camera using a flip mirror.

4.3.2 Resonance Frequencies and Q-Factors

These measurements have been performed on 15 distinct L3-cavities to achieve good statistics. A typical spectrum is shown in figure 4.7. One observes a sharp peak at 532 nm corresponding to residual laser light. For longer wavelength numerous Lorentzian-shaped peaks are visible on a monotonically increasing background. The data of all measured spectra has

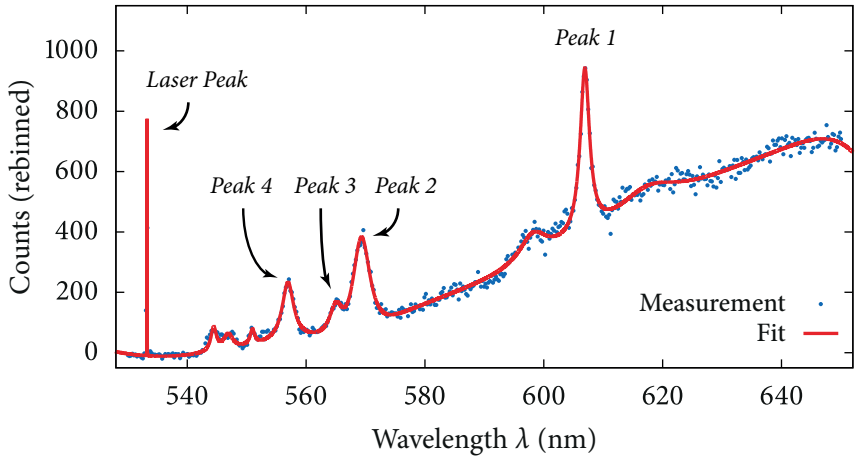

Figure 4.7 | Typical resonance spectrum for an L3-cavity fluorescence measurement. The data was fitted using a polynomial background (6th degree) plus Lorentzians for the most dominant peaks. The peaks corresponding to modes which have been investigated more closely are numbered from 1 to 4. At 532 nm the extremely sharp laser peak is visible.

been fitted using a polynomial background (degree 6) and Lorentzians for the most dominant peaks. An example fit is depicted in figure 4.7 as well. The peak fitting data have been evaluated statistically, offering the results listed in table 4.2. Again shown in this table are the results which were found using FDTD-simulations.

The mode corresponding to peak 2 could not be excited using FDTD-simulations. The other three modes show a great agreement in their resonance wavelength: the deviation for peaks 3 and 4 reaches from about 1 to 2 nm, peak 1 agrees in the scope of the uncertainties. The Q-values are not absolutely comparable, because the crystal dimensions surrounding the defect differ. In the measurement a larger crystal was used and accordingly higher Q-values are possible. Of course, production imperfection and material losses cause opposite effects.

Thus, it has been shown that the simulations are reproducing the measurements with high accuracy and consequently the corresponding methods are well-suited as a tool of comparison for unknown effects too.

		Peak 1	Peak 2	Peak 3	Peak 4
FDTD	λ in nm	606.7	–	564.7	555.7
	Q-factor	380	–	170	75
Measurement	λ in nm	606.9 ± 0.2	569.1 ± 0.1	565.07 ± 0.04	557.03 ± 0.08
	Q-factor	315	190	255	255

Table 4.2 | Resonance mode wavelength and Q-factors for the L3-cavity. Listed are results from FDTD-simulations and fluorescence measurements for the four dominant peaks (see figure 4.7). Mode 2 could not be excited in the FDTD-simulation. Q-factors are only conditionally comparable because of different crystal dimensions.

4.4 Measurement Setup for Transmission Measurements

In the previous sections the chip design has been explained in detail – covering the distinction between *in-plane* and *out-of-plane* channels. Additionally, a first successful measurement was presented in section 4.3, showing the possibility of great agreement between FDTD-simulations and results from experiments. From now on the setup which was used to actually measure the radiation from the transmission channels will be explained.

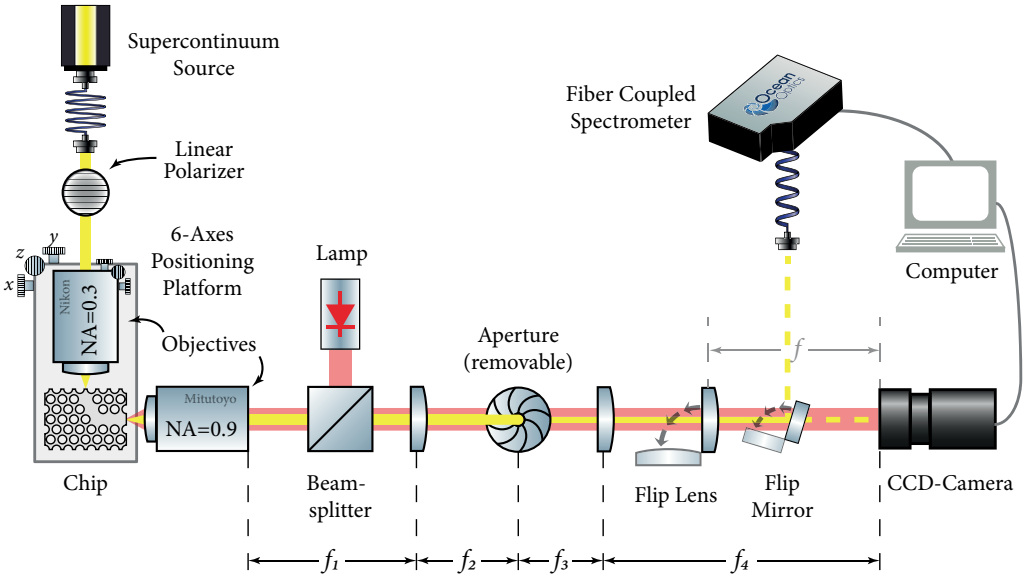

Figure 4.8 | Setup for transmission measurements. Detailed sketch of the used setup for both, in-plane and out-of-plane transmission measurements. An in-depth description is given in the text below.

4.4.1 Used Components and 4f-Configuration

Figure 4.8 depicts the measurement setup in detail. The main source of radiation is a Koheras® SuperK Versa (*NKT Photonics*), which is a *supercontinuum source*. Supercontinuum sources are laser devices with a broad spectral bandwidth. In general, pulsed laser light is guided through a strongly nonlinear device, for example a photonic crystal fiber. When using such a source the experiment benefits from the typical laser properties such as high spatial coherence and high intensities and – at the same time – provide an extensive spectral information.

The supercontinuum source is achromatically fiber-coupled, linearly polarized and then guided to a high working distance objective (NA = 0.3, *Nikon*) for incoupling. This objective, together with the chip, is fixed on a *6-axes positioning platform*. A photograph of this platform is shown in figure 4.9. The objective can itself be moved relative to the chip in all three directions allowing to optimize the incoupling. The whole platform, together with

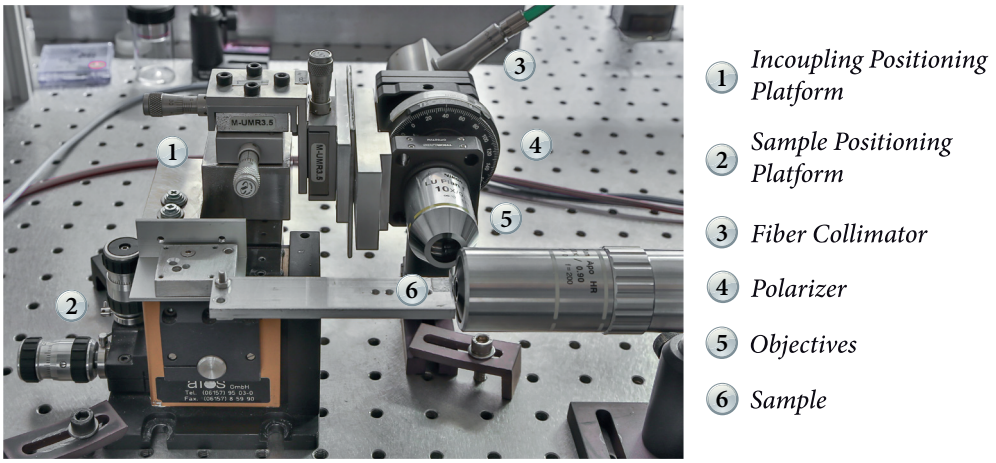

Figure 4.9 | Six-axes positioning platform. Photograph of the actual positioning platform, showing the incoupling platform (1) with the achromatic fiber collimator (3), the polarizer (4) and the incoupling objective (5, top left). This platform, together with the chip (6) is placed onto another positioning platform (2), for the movement in front of the detection objective (5, bottom).

the chip, can as well be moved in front of the detection objective. The *detection objective* (NA = 0.9, *Mitutoyo*) collects the light which radiates from the chip and is additionally illuminated from behind using an LED-lamp for orientation.

Subsequent to the detection objective a *4f-configuration* is aligned. After the first lens this configuration features an image plane where the *removable aperture* is located to clip desired parts of the image. The third (flip) lens gives the ability to switch between real space and Fourier-space on the camera (*Andor* iXon®) – a feature that was used for *back focal plane imaging* (see section 4.7). Using the *flip mirror* the light can additionally be directed onto a *fiber coupled spectrometer* (*OceanOptics* HR4000®).

The described setup can be used for both channel types (in-plane and out-of-plane) if the chip is attached in a proper orientation. For both types, real- and k-space imaging plus the allocation of spectrum data is possible, as well for clipped images.

4.4.2 Polarization

It has been shown numerically in section 3.1 that the triangular hole slab only offers a photonic bandgap for TE-modes. Consequently, in the experiment TM-modes would unnecessarily disturb the measurement and are thus filtered using the linear polarizer shown in figures 4.8 and 4.9.

For TE-like modes with $E_z \approx 0$ the electric field must be polarized *in the slab plane* – the x-y-plane. The proper polarizer angle was determined using a second, high-accuracy Glan–Thompson polarizer. This additional polarizer can also be used in the setup (after the detection objective, not shown in the figure) to investigate the polarization of the output light.

4.5 W1-Waveguide and Filters

Measuring the *transmission* in an experiment is closely related to the calculation of the same in an FDTD-simulation. One needs to know the *absolute* incident flux in order to calculate the *absolute* transmission. The current section focuses on the transmission of the W1-waveguide and the filters.

4.5.1 Measuring Concept

Actual Measuring Process
The measurement for a specific channel is performed in the following steps:

1. incoupling to the channel using the positioning platform,
2. localization of the desired channel output on the camera using the light from the LED-lamp and the emitted light of the channel,
3. focusing of the emitted light onto the spectrometer fiber so that a maximum amplitude is reached in the spectrum,
4. optimization of the incoupling, again so that the spectrum amplitude is maximal.

Incident Flux
The incident flux is the power to which the measured spectrum of an investigated system needs to be normalized in order to calculate the *influence of one specific section* of the system. For the W1-waveguide, the incident light comes from a 300 nm-dielectric waveguide. For the filter, the light comes from the W1-waveguide. This is very similar to the process of calculation in section 3.6. Accordingly, a good approximation for the incident flux of both systems is given by

- the pure dielectric waveguide (channel 4, see table 4.1) for the W1-waveguide and
- the W1-waveguide (channel 5) for the filters,

respectively. Using the data of these channels is of course an *approximation*, since the considered systems are not identical in all parameters (e.g. length of the dielectric waveguide). However, a more significant problem arises from the incoupling. If the data of a specific channel needs to be related to the data of a different channel, the incoupling is changed during the measurement process. Due to that fact, *only relative transmissions* can be measured with the described technique.

4.5.2 Results of the Measurement and Comparison to Semi-Numerical Data

The previously explained steps have been executed for channels 1-5, thus for the purely dielectric waveguide, the W1-waveguide and filters of 1 to 3 holes (see figure 3.16). Since no absolute transmission spectra can be measured, the attention will be on the pure spectra which have been measured. The spectra for the W1-waveguide and a two-hole filter are depicted in figure 4.10 with a black solid line in both cases.

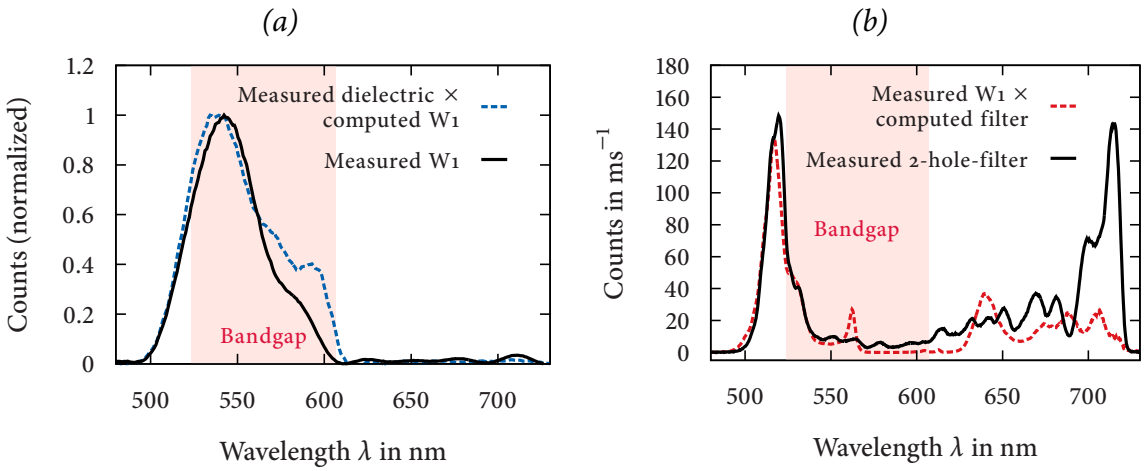

Figure 4.10 | Measured spectra and semi-numerical comparisons for the W1-waveguide and a two-hole L3-filter. (a) Normalized spectrum for the W1-waveguide (black, solid) and product of numerical transmission and measured dielectric waveguide (blue, dashed). (b) Spectrum for the two-hole-filter (black, solid) and numerical transmission times measured W1 (red, dashed). In both investigations a notable accordance can be seen.

W1-Waveguide

The normalized spectrum of the W1-waveguide (figure 4.10a) shows high values in the region of the photonic bandgap and for some shorter wavelengths, thus from about 500–600 nm. From about 700 to 730 nm a slight peak is visible again. This is in agreement with results from the projected band structure and transmission calculations (further details can be found in chapter 5).

A comparison to the calculated transmission spectrum of the W1-waveguide (section 3.6.2) can easily be done, if the spectrum of the dielectric waveguide (channel 4) – which is an approximation of the incident flux $\mathcal{T}_{\text{inc}}$ – is multiplied with the *numerical* transmission spectrum. This can be seen from equation (3.10), which related the measured flux behind the W1-waveguide $\mathcal{T}_{\text{W1}}$ to the transmission by $T = \mathcal{T}_{\text{W1}}/\mathcal{T}_{\text{inc}}$ Consequently, the W1-comparison spectrum is given by

$$\mathcal{T}_{\text{W1}}^{\text{comp}} = T_{\text{W1}}^{\text{num}} \cdot \mathcal{T}_{\text{inc}} = T_{\text{W1}}^{\text{num}} \cdot \mathcal{T}_{\text{ch.4}}. \tag{4.1}$$

The resulting spectrum is denoted by the blue dashed line in figure 4.10a – exposing a remarkable agreement. Only for the long wavelength-half of the bandgap stronger deviations are present.

Filters

A similar procedure can be applied for the filter measurement, shown in figure 4.10b. The semi-numerical comparison in this case is given by

$$\mathcal{T}_{\text{W1}}^{\text{comp}} = T_{\text{filter}}^{\text{num}} \cdot \mathcal{T}_{\text{inc}} = T_{\text{filter}}^{\text{num}} \cdot \mathcal{T}_{\text{ch.5}}, \tag{4.2}$$

since the incident flux is given by the measured spectrum of the W1-waveguide. Inside the bandgap the filter damps most of the light, except for numerous low-Q modes. The numer-

ical transmission spectrum shows peaks at about 562 and 605 nm inside the bandgap. The measured spectrum offers modes at the same positions, but also additional peaks. These might be real modes which just have not been excited in the simulation, since the measured resonance spectrum of the L3-cavity showed additional modes as well (see section 4.3 and figure 4.7).

4.6 The Grating Coupler

After having dealt with comparatively well-known systems like the L3-cavity and the W1-waveguide, the grating coupler will be further investigated in this section. As has been stated in chapter 3, an important quantity for the characterization of the coupler is its *efficiency*. The calculated efficiencies are in the range of about 25–31 %. It was expected that the efficiencies of the produced couplers would be some percent below, because of production inaccuracies.

4.6.1 Measurement Steps

It became apparent in the experiments that the absolute coupling efficiency is difficult to measure, because the incident power is hard to determine. To get a good estimation several measurement steps were required. As in the numerical simulations the main quantities of interest are

1. the incident power P_{inc} illuminating the coupling structure and
2. the outgoing power P_{out} which is scattered to z-direction by the coupler.

If both quantities are known, the efficiency over the photonic bandgap (from λ_i to λ_f) can be computed as in equation (3.17), thus

$$\mathcal{E} = \frac{1}{\lambda_f - \lambda_i} \int_{\lambda_i}^{\lambda_f} T \, \mathrm{d}\lambda = \frac{1}{\lambda_f - \lambda_i} \int_{\lambda_i}^{\lambda_f} \frac{P_{\text{out}}}{P_{\text{inc}}} \, \mathrm{d}\lambda. \tag{4.3}$$

In contrast to the FDTD-simulations monitoring of the radiation reaching the coupler is not possible in a direct way, when using the measuring setup described in section 4.4. Consequently, a workaround is necessary.

Actual Out-Of-Plane Measurement Process
Basically, the out-of-plane measurements are conducted in the following way (the setup is depicted in figure 4.8):

1. incoupling to the channel using the positioning platform,
2. localization of the desired channel output on the camera using the light from the LED-lamp and the emitted light of the channel,

3. insertion of the aperture to clip the desired parts of the image plane, for example to measure the light emitted by the coupler exclusively,
4. focusing of the emitted light onto the spectrometer fiber so that a maximum amplitude is reached in the spectrum,
5. optimization of the incoupling so that the spectrum amplitude is maximal.

Incident Power

To measure a reasonable incident flux that corresponds to a given coupler scattering measurement, *the incoupling must not be changed*. Since P_{out} is measured from a top view (out-of-plane measurement), a way must be found to measure P_{inc} in the same measurement. The idea was to use the *z-radiation from the center of the W1-waveguide* P^z_{W1} for that purpose.

It is an assumption that the z-scattered radiation is proportional to the complete radiation inside the W1-waveguide and it is not proven in the scope of this thesis. However, to find this proportionality the first two steps in the complete process are

Step 1: measurement of the W1-waveguide in-plane, resulting in the complete power which passes the W1-waveguide in x direction P^x_{W1}. This power is approximately equal to the power that reaches the coupling structure. The steps of the measurement have been explained in section 4.5.1.

Step 2: measurement of the same W1-waveguide channel – but out-of-plane – using the steps above. For this measurement the center of the W1-waveguide is clipped with the aperture and the spectrum is recorded, resulting in P^z_{W1} for that channel.

These two quantities can be used to calculated the ratio R_{W1}, which connects the z-scattered radiation of the W1-waveguide center to the complete radiation which passes the W1 – and thus reaches the coupler for the corresponding channels. Unfortunately, the incoupling is changed during this process, since the chip needs to be removed and tilted between the measurements. This non-constant incoupling results in unequal oscillations in the spectrum (further information on these oscillations will be given in the discussion, chapter 5). Consequently, the next step is

Step 3: Fourier-filtering of the data for P^x_{W1} and P^z_{W1} to limit the influence of differing incoupling effects.

The desired ratio is then computed from these filtered spectra, thus

$$R_{\text{W1}} = \frac{\mathcal{FF}\left(P^z_{\text{W1}}\right)}{\mathcal{FF}\left(P^x_{\text{W1}}\right)}, \tag{4.4}$$

where $\mathcal{FF}(x)$ stands for the Fourier-filtered data of x. The quantity of interest for each channel is P_{inc}. This can now be approximated using the ratio (4.4) if the z-scattered radiation of the W1-waveguide center P^z_{W1} is measured for the specific channel using

$$P_{\text{inc}} \approx \frac{P^z_{\text{W1}}}{R_{\text{W1}}}. \tag{4.5}$$

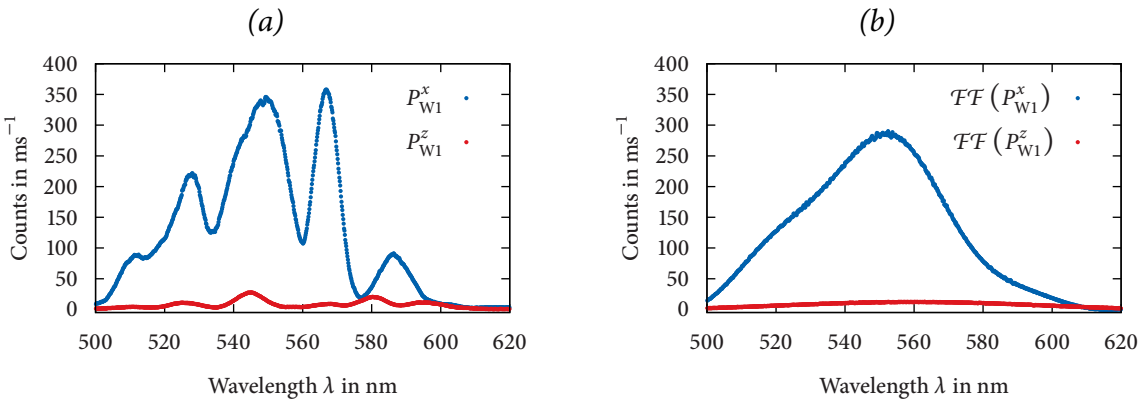

Figure 4.11 | Effect of Fourier-filtering. (a) Measured, background-corrected spectra of the W1-waveguide in x- (blue) and z-direction (red) in the region of the photonic bandgap. The oscillations are inconsistent – peaks in both data are not always at the same wavelength and have differing amplitudes, due to unequal incoupling. (b) The same data after Fourier-filtering. The oscillations are corrected, leading to comparable data well-suited for the calculation of R_{W1}.

Outgoing Power and Efficiency

The final step is

Step 4: the measurement of the *outgoing power* P_{out} given by the spectrum of the pure coupler z-radiation, determined using the steps of paragraph *Actual Out-Of-Plane Measurement Process*.

Together with equation (4.5) the coupling efficiency can then be calculated for a given channel using equation (4.3).

4.6.2 Results of the Measurements

The described technique has been applied to all of the coupler channels and the ratio R_{W1} was determined using a W1-waveguide channel. To clarify the process and to prove its significance some interim results will be given in the following.

Fourier Filtering

A rather fragile part of the investigation is he filtering step, since it potentially reduces the contained information. Anyhow, without this step the calculation does not make sense, since the differing incoupling causes absurd disagreements in the observed spectra. The measured and background-corrected spectra are depicted in figure 4.11a, exhibiting these oscillations. Peaks are inconsistent in both data, as well in amplitude as in wavelength.

After the appropriate filtering the data turns out to be smooth and comparable, as shown in figure 4.11b. These spectra are the ones which were used for the calculation of R_{W1}.

Normalization Procedure

Since parameter optimizations have been included to test how they influence the coupling efficiency, the investigated coupler channels do not feature identical grating couplers. Un-

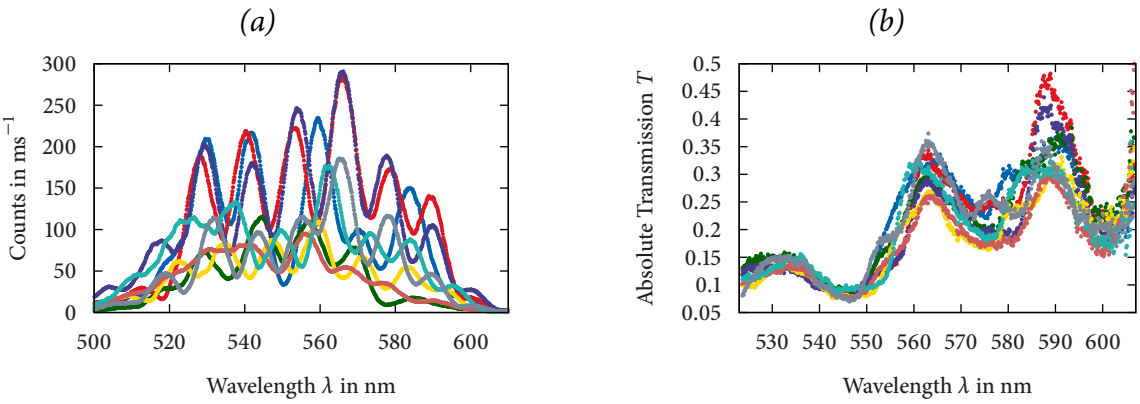

Figure 4.12 | Measured spectra for coupler channels and calculated transmission spectra. (a) Background-corrected spectra for eight different coupler channels, showing wild-looking behavior. The spectra feature strong oscillations, unique for each data set, caused by incoupling effects. (b) The normalization process used for the transmission calculation cancels the incoupling effects and reveals a consistent trend.

fortunately, the uncertainty in the presented calculation is too high to observe the expected differences, as will be shown in section 4.6.3. Consequently, *these differences will be ignored* in the following – all channels will be treated as if they include an identical coupler.

Again, all spectra which were recorded for the different channels exhibit huge discrepancies due to the varying incoupling. Figure 4.12a depicts the measured spectra for eight different channels. The differences are extreme and consequently the spectra look confusing and are not suggestive of belonging to an approximately identical system. This is an impressive example for the fact that incoupling effects are an enormous parameter and must be considered.

In any case, the presented normalization technique reveals that these spectra do exhibit information about the same quantity. This can be seen in figure 4.12b where the absolute transmission is shown for the same channels (computed using equations (4.3) to (4.5)). After the normalization process, the data show an astonishing agreement – being evidence of a reasonable procedure. It is therefore assumed that efficiencies calculated on this basis are trustworthy.

Efficiency

From the consistent data shown in figure 4.12b the efficiency was calculated according to equation (4.3). The transmission spectra of all data sets have been averaged for the computation, resulting in

$$\langle \mathcal{E}_{\text{measured}} \rangle \approx 21\,\%.$$

However, this result is useless without a determination of the uncertainty, since numerous sources of errors have been introduced. A detailed error analysis will be given in the next section.

4.6.3 Uncertainty Calculation

The uncertainties of all measured spectra using the *OceanOptics* HR4000® have been treated as statistical errors of magnitude $\sqrt{\text{count}}$. When measuring P^z_{W1}, the center of the W1 has to be focused using the CCD-camera. The W1-waveguide has a length of roughly 13.2 µm and the uncertainty of the center determination was estimated to ≈ 0.6 µm. Using the numerical power loss spectrum of figure 3.13, the maximum field decay in this uncertainty length was determined to be 10 %. The uncertainty of the Fourier-filtering process was quantified using largest error estimation – the maximum deviation between filtered and measured data was assumed to be the largest possible uncertainty.

All errors have been added using the law of error propagation for uncorrelated quantities. Consequently, an overall largest error was found for each of the calculated transmission spectra of figure 4.12b. Again, the difference between the largest possible resulting curve $T + \Delta T$ and T was used as an approximation for the expectable uncertainty. The final result is

$$\langle \mathcal{E}_{\text{measured}} \rangle = 20 \pm 10\,\%. \tag{4.6}$$

In the numerical calculation of section 3.6, efficiencies in the range of 25–31 nm have been found. These values barely lie in the uncertainty interval of the measured result, although near the upper limit. This is a reasonable result, since smaller values than in the computation are expected for real produced samples.

Taking note of the large uncertainty it is clear that no distinction is observable between the different produced couplers. The calculated differences in the efficiency are of the order of a few percent and thus cannot be resolved. The same reasoning applies to a comparison between measured and calculated transmission spectra (figure 4.12b versus 3.20).

4.7 Back Focal Plane Measurements

At this point, the efficiency of the outcoupler has been investigated using numerical *and* experimental methods. Both techniques showed agreeing results and especially when using simulations, parameter optimizations were found and the tunability was studied.

Admittedly, the numerical investigations did not show a tunability effect when considering only the in-gap efficiency, as it was defined in equation (3.17). But as was mentioned earlier an important quantity of the coupler has not been examined so far. The efficiency calculations and measurements always considered the complete radiation over a large angular space. From now on the attention will be turned to the *directivity* – the angular distribution of the coupler radiation.

4.7.1 Technique of BFP-Measurement

In the experiment, the angular distribution of a scatterer is analyzed using a *back focal plane measurement*. The back focal plane is one of four necessary planes (points) to describe ideal systems in Gaussian optics, as stated by Hecht (2002). All six available *cardinal points* on

the optical axis are the focal points, the principal points, and the nodal points.

The back focal plane (BFP) is the plane perpendicular to the optical axis intersecting the *back focal point* – the focal point between lens and image. Figure 4.13 depicts the location of the BFP, assuming a thick, symmetrically convex lens. The two principle points P and P' are always located inside the lens in such cases. All rays that leave the object *under the same angle* are focused in *the same point* on the BFP. Accordingly, each point on the BFP belongs to rays with the same angle. Thus, if an CCD-chip is placed directly in the BFP, a direct measurement of the angular distribution of the light leaving the object takes place.

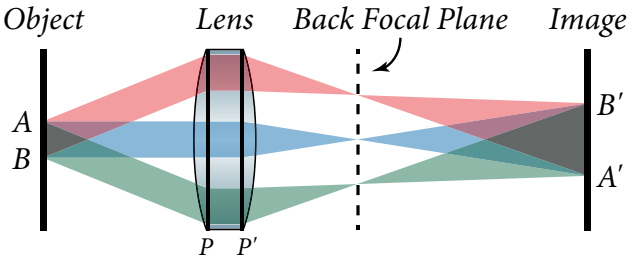

Figure 4.13 | Principle of back focal plane measurement. Sketch of the position of the back focal plane for a system using a thick, symmetrically convex lens. P and P' are the principle points which are always inside the lens in this case. Rays with same angle are focused at the same point in the back focal plane – offering an angular information.

4.7.2 Results of the Grating Coupler Measurement

For the experiment, the camera was aligned to so that it is at the back focal plane position. An on-axis, collimated laser beam was used for the alignment, producing a centered minimal spot on the camera. The setup has been explained in section 4.4 and is depicted in figure 4.8. The flip lens gives the possibility to rapidly switch between real and k-space.

For each measurement laser light was coupled to the desired channel and the coupler light was isolated using the removable aperture. To achieve not only angular resolved, but also *frequency resolved* information, a prototype narrow-band tunable supercontinuum source (*PicoQuant*) was used. This source can be tuned to any desired wavelength in the supercontinuum spectrum and filtered to an approximately 3 nm-bandwidth, purely controlled by software.

The resulting angular patterns for a selection of wavelengths are shown in figure 4.14. The drawn circles for angle determination are *approximations*, extracted from the outer border of visible intensity, approximately corresponding to $\arcsin(0.9) \approx 64.16°$ for an $NA = 0.9$-objective. The intensities are normalized, since the used laser had a non-uniform output power for different tuning wavelength. Thus, the images reveal *no intensity information relative to each other*.

As already mentioned the coupler was tuned to $\lambda_{\text{tune}} \approx 640\,\text{nm}$ for the produced chip. In the figure, lower regions correspond to back-scattered and higher regions to forward-scattered radiation (*forward* corresponds to $+x$direction in figure 3.18). For $\lambda = 600\,\text{nm}$

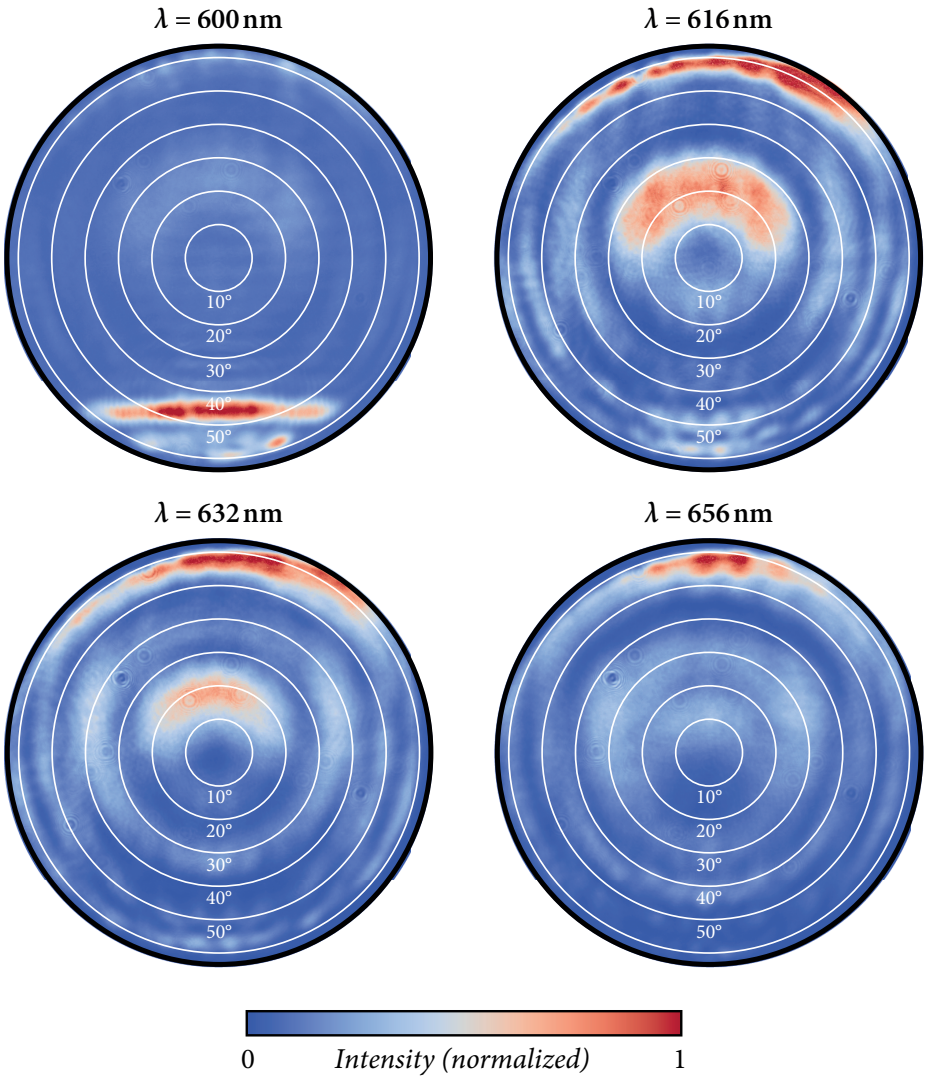

Figure 4.14 | Results of the back focal plane measurement. Angular distributions of the coupler light for 3 nm-bandwidth radiation of wavelength λ = 600 nm, 616 nm, 632 nm and 656 nm. The patterns transition from back-scattering to forward-scattering, passing a region of high directive, perpendicular radiation.

most of the light is back-scattered into angles between 40° and 50°. In contrast, for λ = 656 nm the light radiates to the forward direction to angles of about −60°. Accordingly, the radiation is only slightly influenced, passing as if no coupler was present.

For the intermediate wavelengths the radiation transitions through much more perpendicular patterns. For λ = 616 nm the outline of the coupler is clearly visible and a strong radiation to angles between −10 and −20° exists, being stable till wavelengths of about λ = 640 nm.

The observed behavior is suggestive of an existing tuning functionality. The wavelengths for which the coupler exhibits a high directivity to vertical directions is very close to the

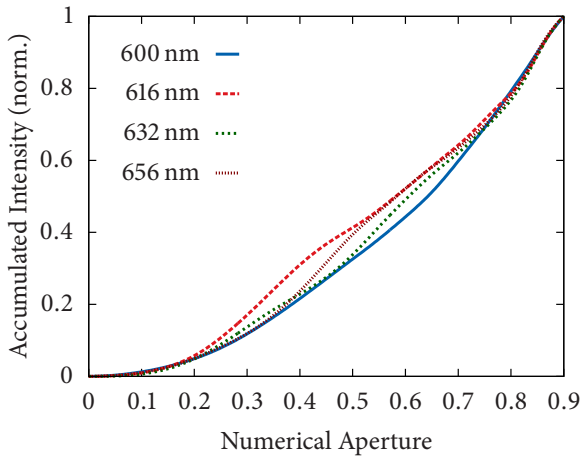

Figure 4.15 | Accumulated intensities for a selection of wavelength. The accumulated intensities $I_a(NA)$ are plotted as a function of the numerical aperture for the same wavelengths as in figure 4.14. For 616 nm the optimum directivity is reached, scattering 41 % of the intensity to angles smaller than 30° (NA = 0.5).

fabricated tuning wavelength of 640 nm. It should be mentioned at this point, that these measurements have been performed *without a polarizer* before the chip. Thus, not only TE, but also TM-modes are excited in the photonic crystal. It is possible that the strong forward scattered pattern in the distribution for 616 nm is due to TM modes (a further discussion is given in chapter 5).

Intensity versus Numerical Aperture

To quantify the results of figure 4.14 a suitable measure is the *accumulated intensity* I_a *over circles of constant numerical aperture* NA. To calculate this quantity a center pixel (i_c, j_c) must be chosen in the original gray-scale images. One can then sum up all values of the pixels which are on a ring of constant NA, thus having a constant radius from the center pixel. Since circles are not well defined on an image consisting of square pixels, one can choose those two pixels per row which fulfill the *equation of the circle*

$$(i - i_c)^2 + (j - j_c)^2 = r^2 \tag{4.7}$$

best, using integer values for i, j and r. The result is an approximation for the intensity as a function of the numerical aperture $I(NA)$ in arbitrary units. When taking the *cumulative sum* of these values the accumulated intensity is obtained

$$I_a(NA) = \int_0^{NA} I(NA')\,\mathrm{d}NA'. \tag{4.8}$$

This quantity is plotted (normalized) in figure 4.15 for the four wavelength 600 nm, 616 nm, 632 nm and 656 nm. In figure 4.14 the best result was obtained for 616 nm, corresponding to the long-dashed red line in figure 4.15. Correspondingly, the accumulated intensity ascends fastest for this wavelength, showing that more intensity is scattered to smaller numerical apertures and thus smaller angles. For NA = 0.5, corresponding to an angle of θ = 30°, the 616 nm-curve already reached 41 %, while the 600 nm-curve is at 33 %.

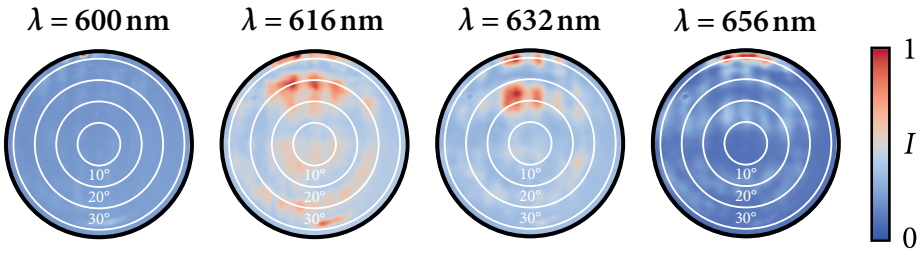

Figure 4.16 | Back focal plane images for an abruptly terminated W1-waveguide. The images are shown for the same wavelengths as in figure 4.14, giving evidence that the patterns at $\lambda = 616\,\text{nm}$ and 632 nm are caused by the grating coupler. The used objective had a numerical aperture of $NA = 0.7$. Stronger noise is due to a very weak signal.

Comparison to an Abruptly Terminated W1-Waveguide

As a final result, figure 4.16 shows the back focal plane images for the same wavelengths as in figure 4.14, but for a channel without a grating coupler – thus an abruptly terminated W1-waveguide. Unfortunately, these patterns were recorded using an objective with a smaller numerical aperture of $NA = 0.7$. Consequently, only angles up to $\theta \approx 44.4°$ are covered. In addition, the images have a stronger noise, since a long exposure time was necessary due to a weak signal.

Anyway, the patterns arising from the coupler, as seen for $\lambda = 616\,\text{nm}$ and 632 nm in figure, *are absent*. No clear pattern is noticeable in the corresponding images without coupler – the light seems to be scattered to arbitrary directions. This again constitutes a proof for the proper functioning of the coupler.

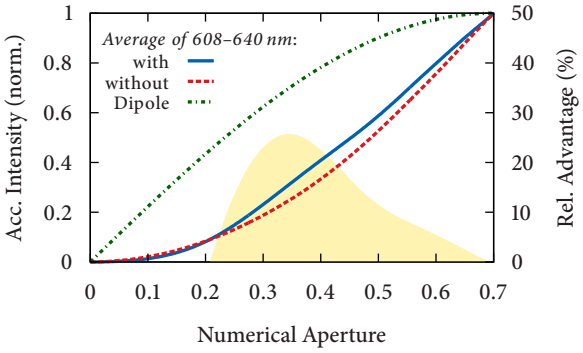

Figure 4.17 | Comparison of coupler and abruptly terminated waveguide. Averaged (608 to 640 nm) accumulated intensities for the abruptly terminated W1-waveguide (red dashed), grating coupler (blue solid) and standard dipole (on-axis, data are normalized to $NA = 0.7$). The yellow region denotes the relative advantage of the coupler (right hand y-axis).

To have a more quantitative comparison, figure 4.17 shows the accumulated intensities averaged over the wavelength range from 608 to 640 nm for three different cases: (i) without the coupler, (ii) with the coupler and (iii) for a standard dipole, radiating on-axis (Demtröder 2009). The curves are normalized to a numerical aperture of $NA = 0.7$, for convenience. The yellow area illustrates the relative advantage of the coupler over the abruptly terminated waveguide in percent (right hand y-axis). Obviously, the coupler is an improvement with respect to the naive approach, but the improvement is less than 30 % (for the maximum). Compared to the standard dipole, the coupler is still far off an optimum implementation.

5 Discussion

The obtained results from numerical and experimental investigations have been presented in the two previous chapters – although these are just numbers and figures without interpretation and comparison between each other. It was already explained in the introduction of chapter 4 that computations and measurements together *can* lead to an improved comprehension, but only if they are carefully weighed up against each other – deciding which approach is trustworthy in the case of occurring contradictions.

Therefore, in this chapter all results are regarded in context, revealing the common grounds of numerical and experimental data. As it was of greatest importance for this thesis, the results corresponding to the grating coupler are considered first. Afterwards, the L3-cavity and the W1-waveguide are made subject of the discussion. At appropriate passages problems and disadvantages of chip design and measurement setup are mentioned as well.

5.1 Overall Result of the Grating Coupler Investigation

5.1.1 Summary of the obtained Results

Several results regarding the double-ring grating coupler structure (figure 3.18), which was proposed by Faraon et al. (2008), have been presented in the previous two chapters. The *numerical results* obtained for the coupler can be found in section 3.6.4 from page 44, where the *absolute transmission* and the *in-gap efficiency* were computed for several couplers, differing in their tuning wavelengths and optimization parameters. Additionally, the influence of the mechanical supports has been investigated. *Experimental results* have been presented in sections 4.6 and 4.7 from page 64. As in the numerical part, the (approximate) absolute transmission was measured for different couplers, all having the same tuning wavelength and mechanical supports but differing in their optimization parameters. At last, the angular distribution of the far-field radiation from the coupler was studied using back focal plane measurements.

All things considered, the results prove the functionality of the coupler in two different ways. These are:

- *the scattering of electromagnetic energy to the vertical (out-of-plane) direction*. Without angular information it was shown numerically and experimentally, that the coupler scatters approximately a quarter of the incident energy to each of the vertical directions. Simulations showed that design optimizations can improve this amount to exceed 30 %. In contrast to the expected behavior the *tunability* was not observed in view of the maximum amount of scattered radiation.

- An *improved directivity in comparison to an omitted grating coupler* was shown using back focal plane measurements, although the advantage was smaller than 30 %. In addition, the tunability regarding the directivity was proved, since the best directivity was found for incident wavelengths near the tuning wavelength λ_{tune}.

Besides, the applied numerical and experimental techniques left some things unclear or were not suitable or accurate enough to give evidence for. The most important points are:

- an unknown source of significant oscillations in the experimentally measured transmission spectra remained unexplained.
- By reason of the inaccurate measurement technique, it was impossible to observe the effects of parameter optimizations experimentally. Accordingly, the numerical results have not been confirmed in practice, to date.
- The improper tuning wavelength of the produced grating coupler hindered the investigation of important quantities – such as the directivity – because unpolarized light had to be used for the back focal plane measurements. Accordingly, the influence of excited TM-modes can not be assessed.
- Due to unknown power amplitudes the back focal plane images could not be compared quantitatively. As a consequence, it is unclear if the obtained advantages of the coupler over the abruptly terminated waveguide in view of directivity are meaningful.

The following sections will provide more details on the facts stated in this overview by comparison of the numerical and experimental data and discussions of uncertainties.

5.1.2 Calculated and Measured Transmission Spectra

A quantity which is well-suited for a comparison is the *absolute transmission* of the coupler, as it was determined via experimental and numerical approaches. A plot of both data sets for an identical coupler with supports and a tuning wavelength of $\lambda_{\text{tune}} = 640\,\text{nm}$ is depicted in figure 5.1. The data from simulations (red dashed line) show a comparatively stable behavior, exhibiting transmission values of ≈ 0.22 to 0.32. A soft oscillation with a wavelength of about 11 nm is visible, transitioning to a shorter wavelength and larger amplitude near the low-energy edge of the bandgap at ~ 607 nm. The origin of the oscillations is unclear. They could be due to numerical errors or to reflections inside the W1-waveguide.

In contrast, the experimental data (blue solid line) show large variations from 0.08 to 0.38, reaching higher values near the low-energy edge of the bandgap. A comparable oscillation of 11 nm is not visible. However, the light blue shaded region denotes the approximate (maximum) error interval for the experimental data, indicating a large uncertainty. Consequently, it is not expected that the resolution of this measurement is good enough to reveal oscillations of this order of magnitude. Since a check sum procedure was used to validate the numerical data (section 3.6.4, paragraph *Way of Validation: The Check Sum*) , the error should not exceed 10 %. For that reason, the numerical data might have an advance in reliability.

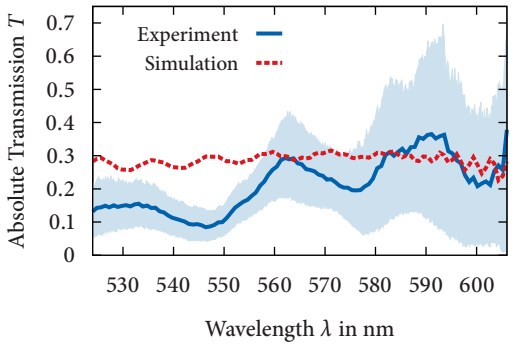

Figure 5.1 | Comparison of coupler transmission spectra. Absolute transmission spectra for an identical coupler ($\lambda_{\text{tune}} = 640\,\text{nm}$, with supports, no optimizations) which were obtained experimentally (blue) and numerically (red). The light blue region illustrates the comparatively large interval of uncertainty for the experimental data.

Anyhow, the agreement of both data sets is not too bad. If for example the numerical curve is slightly shifted to lower values – as it is to expect due to manufacturing imperfections – it predominantly lies inside the error interval of the measurement. Hence, improvements of the chip design and the measurement technique may uncover a better agreement with the numerical data.

Efficiencies

The efficiencies, as defined by equations (3.17) and (4.3), are computed from the absolute transmission spectra. Consequently, the same reasoning can be applied: the computations might be more trustworthy, since the experimental results suffer from large uncertainties. A comparison is possible for the determined results for a coupler with supports and identical tuning wavelength

$$\mathcal{E}_{\text{FDTD}} = 28.7\,\%, \qquad \langle \mathcal{E}_{\text{measured}} \rangle = 20 \pm 10\,\%. \tag{5.1}$$

Certainly, the measured result is an average over several couplers with differing tuning parameters. This fact has been neglected, since computational results suggested that the differences are not resolvable. The numerical result lies near the upper limit of the error interval of the experimental result. This is indeed reasonable, since simulations neglect a couple of effects present in real systems. Anyhow, as before a more sophisticated measurement technique would be desirable to lower the uncertainty.

Disadvantages of Chip Design and Measurement Technique

During the measurements a couple of complications were caused by unexpected behavior of the transmission channels and improper design elements of the chip. An observed characteristic of great significance was the *extreme dependency on incoupling*: a small change in the position of the incoupling laser beam resulted in massive changes in the measured spectra. The reason is assumed to be the cleaving edge of the chip. Since the laboratories in which the production was carried out did not provide a machine to cut well-defined pieces out of the silicon-based wafer, the chip was simply broken along crystallographic axes. Consequently, the edge can not be expected to be plane and hence arbitrary scattering may occur. It was thus hard to determine an optimum adjustment for the incoupling, complicating a proper measurement. The effects on the spectra had been illustrated in figure 4.12a on page 67, exhibiting the weird behavior occurring on nearly identical systems!

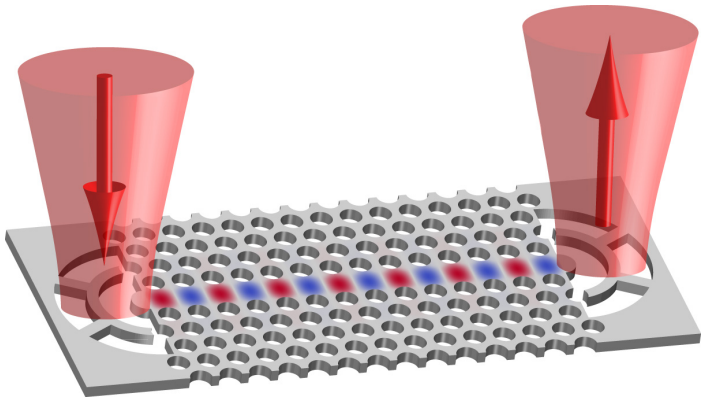

Figure 5.2 | Proposal for a different measurement technique. A W1-waveguide may be terminated by two identical couplers to obtain a symmetric system. One coupler would be used for incoupling, the other one for outcoupling of laser radiation.

A second fundamental issue was caused by *oscillations*, which are as well visible in the spectra of figure 4.12a. Interestingly, these oscillations were present on all channels, even those without any photonic crystal structures (dielectric waveguide). Hence, it is logically to assume that these oscillations are not caused by reflections inside the photonic crystal waveguide. Calculations suggested an estimated resonator length of about 10 µm as the origin of the oscillations. Unfortunately, no adequate structure is present in the design, leaving the phenomenon unexplained. However, a candidate is the tapered part of the dielectric waveguide and the mode cleaner (figure 4.5 on page 56). Both components may introduce side effects and contribute to the unwanted oscillations. The resulting necessary procedure of Fourier filtering in the efficiency determination (section 4.6.2) is one of the undesirable consequences, contributing to the large uncertainty of the accompanying results.

As a third important mistake in the chip design, the improper tuning wavelength of the coupler may be noted again at this point. The tuning wavelength of about 640 nm was formerly chosen to accord with a red diode laser, which was intended to be used for operation. The lattice constant and hole diameter of the photonic crystal samples have been changed again afterwards, due to formerly unknown fabrication guidelines. Unfortunately, it was not noticed that after the adjustment the tuning wavelength lay in the range of very low transmission of the waveguide. Of course, future measurements should use more advantageous values for these parameters.

To overcome most of the presented problems, a different measurement approach would be reasonable. A possible technique is depicted in figure 5.2. Two identical grating couplers are placed at both ends of a W1-waveguide. One coupler is used for incoupling, the other one for outcoupling – with a suitable detection device located above it. This scheme would exhibit significantly less uncertain variables and may be directly implementable in an FDTD-simulation. Parameter optimizations should clearly affect the detected light, since in- and outcoupling are influenced in the same way. Anyhow, problems may arise from the spatial closeness of both couplers, thus rather long waveguides may be needed.

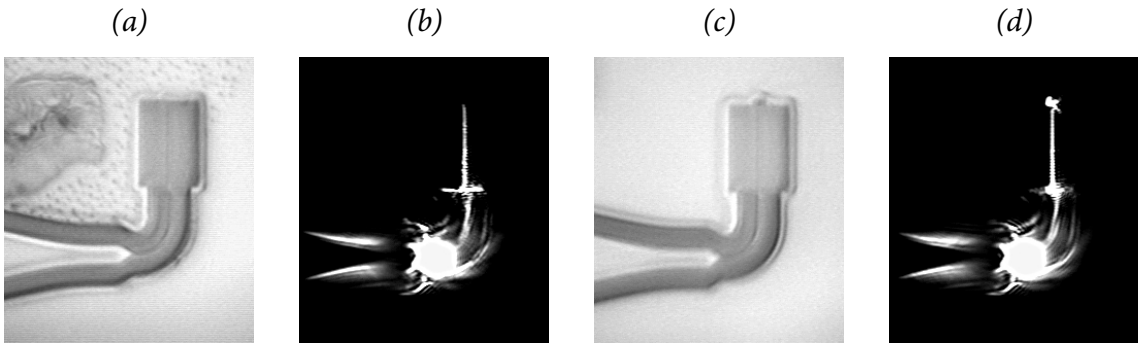

Figure 5.3 | Visible coupler action. The images illustrate that the coupler functionality was even visible using a direct camera observation. Images (a) and (b) show a channel *without* coupler with direct illumination from top and scattered laser radiation, respectively. (c) and (d) show the same situations for a channel *with* coupler. The radiation coming from the coupler is clearly visible as a bright spot.

Another challenge would be to find a measurement technique for the incident power, as it is necessary to obtain quantitative information.

5.1.3 Directivity

Besides the obtained transmission spectra, the back focal plane measurements were used to analyze the angular distribution of the coupler light (section 4.7). These results are of special importance, because they complete the information of the transmission measurements and calculations. Suppose a detector is situated above the coupler in a distance d and covers a circular area of $A = \pi r^2$. Geometrical considerations show that only light which is scattered to angles smaller than $\varphi_{\max} = \operatorname{arccot}(d/r)$ can be detected. The same line of reasoning can be applied to an objective, for which the maximum angle is $\varphi_{\max} = \arcsin(NA)$, where NA is the numerical aperture. Let $\varphi_{\max}$ be 30° ($\rightarrow NA = 0.5$) for a fictive detector and the operation wavelength be $\lambda \approx 607\,\mathrm{nm}$, which is the low-energy edge of the band gap. The absolute transmission of the coupler at this wavelength is about 30 % (figure 5.1) and from the back focal plane measurements it is known that the coupler scatters about 40 % of the total power to this range of angles (figure 4.15). Consequently, the absolute fraction of detected light is about 12 %. In the photon picture one would speak of *detection probabilities* if a single-photon device is investigated. For this purpose 12 % may not be satisfactory.

It is thus important to be aware of both characteristics: the absolute transmission and the directivity. For a proper working device, both quantities have to be optimized. It was already mentioned that the results of the back focal plane measurements may not be completely consistent. The advantage in directivity over the omitted coupler was measured to be less then 30 %. This fact seems to be contradictory to camera observations, which are shown in figure 5.3. Images 5.3a and 5.3b show top views of a channel without coupler; 5.3c and 5.3d show the same for a channel with coupler. Images 5.3a and 5.3c have been obtained using direct illumination from top, while the two darker images show the laser radiation

which is scattered during the propagation through the structure. As expected, the end of the taper and the mode cleaner scatter the greatest fraction, since in this region a transition from a multi mode to a single mode waveguide occurs. Another bright spot is visible at the incoupling area of the photonic crystal waveguide. Along the W1-waveguide the radiation decreases, since the power inside of it decays exponentially due to propagation losses (section 3.5). However, the bright spot at the coupler position in image 5.3d is missing in 5.3b. Accordingly, it is expected that far more light is radiated by the coupler, as it is even visible using a camera.

This supposed inconsistency shows that an *incident power information* would also be desirable for the back focal plane measurements. For the omitted coupler channel, very small intensities have been recorded in the back focal plane – complicating to distinguish between radiation coming from the desired spot or from outside. A quantitative comparison is not possible, since the incident power is unknown. A possible solution would be to introduce a *control scatterer* at a fixed position in each channel. Using a second microscope, the radiation from this scatterer could be measured and used for normalization.

Evaluation of Achievements

Anyhow, the angular distributions measured for the coupler seem to be trustworthy, since they mirror the coupler outline near the tuning wavelength $\lambda_{\text{tune}} \approx 640\,\text{nm}$ (see figure 4.14). Hence it is assumed that the corresponding results for the accumulated intensity versus NA together with the absolute transmission spectra give a good estimation for the coupler characteristics. A repetition of the back focal plane measurements with a tuning wavelength inside the photonic bandgap, a control scatterer for the incident power estimation and with a polarizer allowing to work exclusively on TE-modes should give even more detailed information. In addition, FDTD simulations with a near- to far-field transformation (section A.2) are desirable to have a comparison for the expected far-field patterns.

5.2 L3-Cavity Analysis

The L3-cavity is possibly the most intensely investigated resonator of triangular lattice slab-type photonic crystals. It was the first one for which Q-factors in the scale of $4 \cdot 10^4$ were found experimentally (Akahane et al. 2003) and in this context several different, easy-to-produce optimization techniques have been found. An important advantage is also that the remaining crystal remains unaffected – in contrast to the double-heterostructure, for which the lattice constant has to be varied in a specific region, for example (Song et al. 2005). Besides the well-studied fundamental mode, the L3-cavity supports numerous alternatives for modes, which as well have been analyzed in detail by Chalcraft et al. (2007).

It were these advantages which lead to the utilization of the L3-resonator as a comparison structure for the produced chip (see figure 4.4) – acting as a tool of validation for the numerical analyzes.

Review of the Results

Numerically, the L3-defect was studied in section 3.3. Using FDTD-simulations, the saturation of Q-factors – which is expected for photonic crystals with incomplete bandgaps – was shown. This effect occurs because for larger crystals the leakage of the cavity happens mainly by imperfect index confinement.

Afterwards, the *s*-parameter optimization was studied as well using FDTD simulations (figure 3.3). Physically, a slow variation of the cavity electric field distribution is needed to minimize leakage effects – most ideally described by a Gaussian function (Song et al. 2005). The shift of outer holes helps to improve the fulfillment of this criterion. It was shown that *a doubling of Q-factors is possible* for the investigated structure. Since only Q-factors up to 700 were found, no state-of-the-art applications would be possible using these cavities. Anyhow, the focus was not on a maximum Q-factor, but on an agreement between numerical and experimental results. As a second effect of the *s*-parameter modification, a *frequency shift was observed* for two modes. This was also reported by Chalcraft et al. (2007) and can even lead to reordering of modes.

In the simulations only a small number of modes could have been found. This illustrates that FDTD is not the best-suited tool for the investigation of cavity modes. In fact, Chalcraft et al. chose a completely different approach, using calculations which find the modes using an expansion in a basis of the guided modes of an unpatterned membrane. Accordingly, for a complete mode structure analysis techniques other than FDTD may be considered as well.

In the fluorescence measurements (section 4.3) a larger number of modes has been found – again illustrating the problems occurring in FDTD. The mode frequencies and Q-factors have been obtained using Lorentzian fits and *three peaks could successfully be compared to FDTD results*. The results have been listed in table 4.2 and show an amazing agreement between calculations and measurements. It is again noted at this point that *no parameters of the photonic crystals have been adjusted for the calculations* – all simulated quantities are based on measurements. Consequently, the L3-cavity investigations proved the reliability of FDTD predictions – serving as an argument to use FDTD as a tool of validation for systems which are not as well-known.

5.3 Consistency Considerations regarding the W1-Waveguide

The system which enables the vertically outcoupling of light out of photonic crystal structures is composed of the grating coupler on the one hand, and a *W1-waveguide* on the other hand. Consequently, it was not only the grating itself which was of interest, but also the waveguide which needed to be understood as complete as possible. Again, numerical and experimental tools have been applied to carry out this study.

As an analysis which provides great insight the *projected band structure* was calculated in section 3.4. Using FDTD, the propagation loss spectrum (section 3.5) and the (absolute) transmission spectrum (section 3.6) were obtained. In the experiments, the (relative) transmission spectrum was measured (section 4.5) as well. The results corresponding to

filters are not further discussed, as they were of minor significance.

The following sections study these results again in view of consistency and reliability. In addition, a comparison to literature values for the propagation loss will be given.

5.3.1 Projected Band Structure and Simulated Spectra

The projected band structure analysis of the W1-waveguide revealed the complete information about the guided modes – as well for the index-guided as for the gap-guided modes (figure 3.11). There were six guided modes in total of which three were gap-guided. Normally, it is expected that only for frequency ranges which exhibit guided modes a proper functionality of the waveguide is given. However, the propagation loss and transmission computations both suggest a well transmittance even far off the guided mode frequencies. For a better overview the propagation loss and the transmission spectrum of chapter 3 have been depicted again in figure 5.4. Additionally, the wavelength ranges which are covered by guided modes of the projected band structure are shown by yellow shadings.

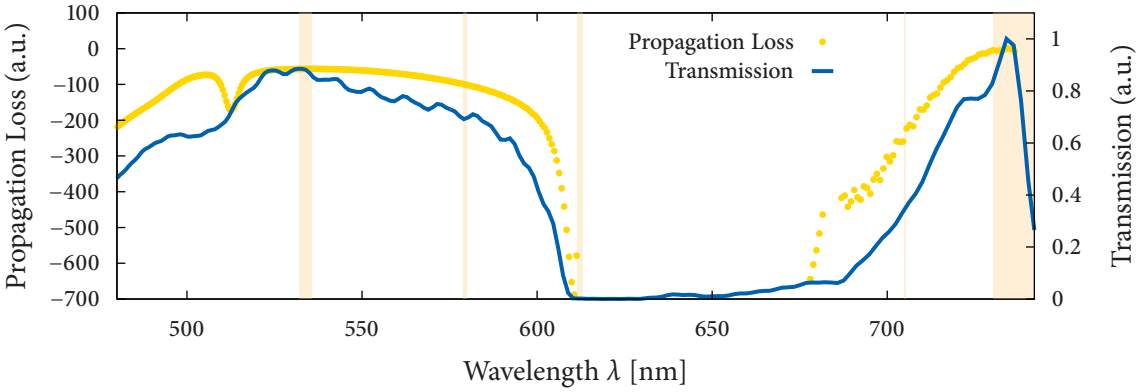

Figure 5.4 | Comparison of propagation loss spectrum, transmission spectrum and guided modes. Propagation loss (yellow dots) and transmission spectrum (blue) are shown in arbitrary units. Yellow shaded areas denote wavelength ranges for which guided modes are present.

Actually the regions between the yellow shaded ranges are referred to as *stop bands*. The transmission should be considerably low in this region, likewise the propagation losses should be high. The FDTD computations of Kappeler et al. (2011) de facto showed this behavior. Unfortunately, the presented results do not exhibit these features. The computed guided mode at ~ 607 nm even lies in a region of very low transmission and high propagation losses. It is unclear whether an error is present in one of the methods or not. On the one hand, the projected band structure calculation is a well-understood procedure – the calculated field patterns are very similar to those of Joannopoulos et al. (2008), for example. On the other hand, the propagation loss and transmission calculations use two considerably different approaches, but both feature agreeing results. Additionally, the transmission spectrum is also confirmed experimentally (see next section).

As a consequence thereof further investigations are necessary to solve the problem of

contradictions. A possible way would be to reproduce the results of Kappeler et al. (2011) with the developed numerical techniques as it would maybe reveal if one of the techniques is erroneous. If the results are accurate, one would have to think of which physical mechanism could produce the observed guidance inside the stop bands.

5.3.2 Simulated and Measured Spectra

A comparison between simulated and measured results for the transmission of the W1-waveguide has already been presented in section 4.5.2, especially in figure 4.10a – exhibiting a good agreement. Anyhow, the experimental data suffered from most of the same issues as the transmission measurements on the grating couplers. These problems have been discussed in detail in section 5.1.2 and in brief they are (i) a strong dependency on incoupling and (ii) intense oscillations on the spectra of unknown origin. The possibilities to overcome these disadvantages are of course the same as for the coupler measurements.

Another desirable feature would be to measure *absolute* rather than only *relative* transmission spectra. To achieve this a reliable measure for the incident power is needed. As explained earlier this could be gained using a well-defined scatterer, perhaps already inside the dielectric waveguide. A channel without photonic crystal could than be used to find the relation between scattered and incident power.

5.3.3 Comparison to Literature Propagation Loss Values

Lastly, the computed propagation loss of the W1-waveguide should be compared to literature results, in order to give a better imagination of its scale. The in-gap minimum loss was calculated to be -1921 ± 8 dB/cm, equaling to a loss of about 36 % for a waveguide of 1 µm length. The lowest reported loss which was found for a comparable system was −154 dB/cm (measured, substrate-type W1-waveguide; Kappeler et al. 2012) – thus corresponding to a loss of only 3.5 % over 1 µm of length. However, this was a highly optimized system and accordingly a factor of 10 (in dB) is not a bad result. But an optimization seems to make sense, since lengths of W1-waveguides in realistic networks may be in the scale of ~ 10 µm.

Moreover, several different systems for waveguiding of optical frequencies are available. Especially for the case of nanometer-sized networks, Tong et al. (2003) reported on subwavelength-diameter *silica wires* with losses smaller than −1 dB/cm. Such structures could be used to connect parts of optical networks which are too distant and thus contribute to these systems.

For terrestrial or over-sea distances photonic crystal slab waveguides are obviously not well-suited. Classical all-glass fiber optics, as used for telecommunication, exhibit losses in the order of −4 dB/km (Saleh and Teich 2007) for optical frequencies, and even smaller for telecom-frequencies (−0.15 dB/km). Probably the lowest losses are obtained using *photonic crystal fibers* (sometimes called *microstructured optical fiber*), – materials which use the photonic bandgap rather than index-guiding for the confinement. Such structures have been reported to exhibit losses on the order of −0.58 dB/km already in 2003 and provide a multitude of applications, such as ultrahigh nonlinearities (e.g. for supercontinuum sources) or atom and particle trapping and guidance (Russell 2003).

6 Conclusion

The focus of this thesis was on the investigation of important characteristics of the grating coupler proposed by Faraon et al. (2007) – thus to answer the question *if this particular structure is a good implementation for a vertical scatterer; providing a high efficiency, directivity and tunability*. In the following, the obtained answer to this question will be given again as compact as possible together with a brief summary of the complete thesis. The chapter will be closed with an outlook regarding applications using the presented photonic crystal components.

6.1 Summary

The important *theoretical concepts* for the description of light propagating through photonic crystal structures were presented in the first part of *chapter 2*. As the foundation, the macroscopic *Maxwell equations* together with simplifications for the considered materials were explained and the *wave equation* was derived from them. By rewriting the wave equation in form of an *eigenvalue problem*, similarities to quantum mechanics and hence solid state physics were highlighted. As a fundamental difference the important property of *scale invariance* was shown. After these general considerations the special characteristics of photonic crystals – especially photonic bandgaps – were derived from the nature of symmetries.

The second part of chapter 2 dealt with the field of *computational electrodynamics*, as numerical methods were of tremendous importance for the entire thesis. Beside a brief explanation of *dimensionless units*, the important *frequency-domain eigensolver techniques* for the calculation of photonic band structures and the *finite-difference time-domain method (FDTD)* were presented.

Both methods have been used throughout to achieve the results which were exposed in *chapter 3*. Here, it was shown how band structure calculations can be used to achieve a *maximum bandgap* for infinitely periodic photonic crystal slabs. A selection of important defects for the considered triangular lattice were then explained, primarily those which are used to form *resonators* and *waveguides*. On this basis, numerous own numerical investigations were presented. At first, the *L3-cavity* was studied as a well-known reference system in view of Q-factor saturation, Q-factor tuning and its mode frequencies – with the intention to validate the computational predictions with later measurements. Secondly, the *W1-line defect* was analyzed in three different ways: (i) the *projected band structure* and selected mode profiles were calculated, (ii) the *propagation loss* spectrum was computed using the FDTD-method, as well as (iii) the *absolute transmission* of a system of two dielectric waveguides coupled from both sides to the W1-line defect. Additionally, different

filters have been investigated as well using approach (iii).

After the reference system (L3-cavity) and the light guiding structure (W1-waveguide) had been studied in-depth, the structure of greatest interest – the *double-ring grating coupler* – was examined. Besides the explanation of its geometry, transmission measurements have been used to analyze the influence of necessary mechanical supports and three parameters of optimization, including the tuning wavelength.

In *chapter 4* experimental results were presented. As it is of importance for an experimentalist, the production process of photonic crystals was marked briefly. Furthermore, the optical chip produced in this fashion was explained in detail, as well as utilized measurement techniques and setups. L3-cavities were studied regarding their mode frequencies and Q-factors using fluorescence measurements – proving an outstanding agreement between experimental and computational results. Accordingly, the remaining quantities which were obtained numerically and which were accessible through measurements have been attained: transmission spectra for grating couplers, W1-waveguides and filters. The coupler was shown to reach an efficiency on the order of 20 % in the range of the photonic bandgap – in comparatively good agreement with numerical calculations. Improvements through parameter optimizations could only be shown numerically. In addition to the simulations, back focal plane measurements were used to study the angular distribution of the coupler radiation. In this respect, the tunability of the coupler could be shown in view of its directivity. Comparing measurements to a channel without coupler proved the advantage obtained by the coupler, although it was only of the order of 30 % and is thus capable of development.

Finally, in *chapter 5* all results have been weighed up against each other and possible contradictions were discovered. Moreover, disadvantages and ways of improvement for the measurement techniques were discussed and in particular for the propagation loss of the W1-waveguide comparisons to literature results were made.

6.2 Outlook

Several components for integrated devices for visible light based on photonic crystals were studied in the scope of this thesis – many of them were already well-understood, such as the L3-cavity and the W1-waveguide. Certainly, results for a structure which is particularly unexplored have been obtained as well: the grating coupler. Especially in combination with quantum mechanical two-level emitters, the assembly of optical networks oriented towards real applications appears realistic.

The physical background of cavity-emitter systems is explained in the appendix (section A.3) and candidates for such emitters are nitrogen-vacancy centers in nanodiamonds or quantum dots. Such systems were intensely investigated over the last decade, a fact that may be illustrated with some examples. That the emission of a quantum dot can be controlled over a large spectral range was shown experimentally by Lodahl et al. (2004). They used an inverse opal photonic crystals and proved that modified emission can be observed over large frequency bandwidths of 10 %. Furthermore, various applications using cavity-

quantum dot systems have already been shown to work. A quantum dot as active medium embedded in a *p-i-n* junction and surrounded by Bragg-mirrors has been used to produce single photons or regulated pairs of photons (Benson et al. 2000). Even a potential to generate pairs of entangled photons was observed, which is a main problem for quantum information processing. In addition, similar systems have been used to build ultra-small and ultra-fast all-optical switches and logic devices (Asakawa et al. 2006). Consequently, extremely fast photonic digital processors could be a possible future application. Englund et al. (2007) as well showed that quantum dots can be used to control the reflectivity of a photonic crystal cavity, offering the chance to realize quantum devices based on coherent light scattering and large optical nonlinearities. Recently, near-unity coupling between a quantum dot and a W1-waveguide mode was reported by Arcari et al. (2014).

For most of such systems, a direct vertical incoupling of laser radiation or the vertical detection using grating couplers could help to reach a higher level of integration or miniaturization. A specific example was already given in the introduction (chapter 1, figure 1.3) – an on-chip Hong-Ou-Mandel experiment. Just as in this case, the communication between different parts of a future photonic computer could utilize grating couplers and thus exploit the space available in the third dimension.

A further investigation of coupler geometries and optimizations is thus desirable – helping to achieve even higher directivities and efficiencies. The next step would be to break the mirror symmetry in the vertical direction and thus try to generate a predominant direction for the emission. This way, efficiencies exceeding 50 % would be possible and are maybe essential for single-photon devices. The numerical and experimental techniques which have been developed for this thesis provide a well-suited foundation for the achievement of these aims. The computational methods are already suitable to investigate arbitrary coupling structures. Using overlay processing couplers with broken mirror symmetry can as well be fabricated.

A Appendix

A.1 Update Equations for a 2d-FDTD Algorithm

For clarification, the update equations for a 2d-FDTD scheme will be derived in detail. In three dimensions, the Maxwell curl equations can be written explicitly as

$$\begin{aligned}
\frac{\partial H_x}{\partial t} &= -\frac{1}{\mu}\left(\frac{\partial E_z}{\partial y} - \frac{\partial E_y}{\partial z}\right), & \frac{\partial E_x}{\partial t} &= \frac{1}{\epsilon}\left(\frac{\partial H_z}{\partial y} - \frac{\partial H_y}{\partial z}\right), \\
\frac{\partial H_y}{\partial t} &= -\frac{1}{\mu}\left(\frac{\partial E_x}{\partial z} - \frac{\partial E_z}{\partial x}\right), & \frac{\partial E_y}{\partial t} &= \frac{1}{\epsilon}\left(\frac{\partial H_x}{\partial z} - \frac{\partial H_z}{\partial x}\right), \\
\frac{\partial H_z}{\partial t} &= -\frac{1}{\mu}\left(\frac{\partial E_y}{\partial x} - \frac{\partial E_x}{\partial y}\right), & \frac{\partial E_z}{\partial t} &= \frac{1}{\epsilon}\left(\frac{\partial H_y}{\partial x} - \frac{\partial H_x}{\partial y}\right),
\end{aligned} \tag{A.1}$$

if electric and magnetic currents are neglected. For two-dimensional systems of size 0 in z-direction, all partial derivatives $\partial/\partial z$ vanish and thus, the Maxwell equations decouple into two sets of independent equations

TM-polarized:

$$\frac{\partial H_x}{\partial t} = -\frac{1}{\mu}\frac{\partial E_z}{\partial y}, \qquad \frac{\partial H_y}{\partial t} = \frac{1}{\mu}\frac{\partial E_z}{\partial x}, \qquad \frac{\partial E_z}{\partial t} = \frac{1}{\epsilon}\left(\frac{\partial H_y}{\partial x} - \frac{\partial H_x}{\partial y}\right), \tag{A.2}$$

TE-polarized:

$$\frac{\partial E_x}{\partial t} = \frac{1}{\epsilon}\frac{\partial H_z}{\partial y}, \qquad \frac{\partial E_y}{\partial t} = -\frac{1}{\epsilon}\frac{\partial H_z}{\partial x}, \qquad \frac{\partial H_z}{\partial t} = -\frac{1}{\mu}\left(\frac{\partial E_y}{\partial x} - \frac{\partial E_x}{\partial y}\right). \tag{A.3}$$

As an example, the update equations will be derived for the TM-case. For the temporal and spatial discretization of the lattice the following notation will be used

$$\begin{aligned}
{}^{(z)}E^{n}_{i,j} &= E_z(i\Delta x,\ j\Delta y,\ n\Delta t), \\
{}^{(x)}H^{n+1/2}_{i,j+1/2} &= H_x\left(i\Delta x,\ (j+1/2)\Delta y,\ (n+1/2)\Delta t\right), \\
{}^{(y)}H^{n+1/2}_{i+1/2,j} &= H_y\left((i+1/2)\Delta x,\ j\Delta y,\ (n+1/2)\Delta t\right).
\end{aligned} \tag{A.4}$$

If the derivatives in equations (A.2) are replaced by finite differences (equations (2.36) and (2.37)), one can obtain the following update equation for the z-component of the elec-

tric field

$$\frac{{}^{(z)}E_{i,j}^{n+1} - {}^{(z)}E_{i,j}^{n}}{\Delta t} = \frac{1}{\epsilon_{i,j}} \left(\frac{{}^{(y)}H_{i+1/2,j}^{n+1/2} - {}^{(y)}H_{i-1/2,j}^{n+1/2}}{\Delta x} - \frac{{}^{(x)}H_{i,j+1/2}^{n+1/2} - {}^{(x)}H_{i,j-1/2}^{n+1/2}}{\Delta y} \right),$$

$$\Rightarrow \quad {}^{(z)}E_{i,j}^{n+1} = {}^{(z)}E_{i,j}^{n} + \frac{\Delta t}{\epsilon_{i,j}} \left(\frac{{}^{(y)}H_{i+1/2,j}^{n+1/2} - {}^{(y)}H_{i-1/2,j}^{n+1/2}}{\Delta x} - \frac{{}^{(x)}H_{i,j+1/2}^{n+1/2} - {}^{(x)}H_{i,j-1/2}^{n+1/2}}{\Delta y} \right). \quad \text{(A.5)}$$

Equation (A.5) is an explicit equation, which can easily be implemented on a computer. The E_z field at time step $n+1$ is calculated from E_z at time step n and the H_x and H_y fields at time step $n+1/2$. This is exactly the temporal scheme depicted in figure 2.7. The quantity $\epsilon_{i,j}$ in this case, is a matrix-element corresponding to the dielectric constant on the grid point (i, j). Similar equations can be derived for the magnetic fields

$${}^{(x)}H_{i,j+1/2}^{n+1/2} = {}^{(x)}H_{i,j+1/2}^{n-1/2} - \frac{1}{\mu_{i,j+1/2}} \frac{\Delta t}{\Delta y} \left({}^{(z)}E_{i,j+1}^{n} - {}^{(z)}E_{i,j}^{n} \right), \quad \text{(A.6)}$$

$${}^{(x)}H_{i+1/2,j}^{n+1/2} = {}^{(x)}H_{i+1/2,j}^{n-1/2} + \frac{1}{\mu_{i+1/2,j}} \frac{\Delta t}{\Delta x} \left({}^{(z)}E_{i+1,j}^{n} - {}^{(z)}E_{i,j}^{n} \right), \quad \text{(A.7)}$$

where μ_{ij} corresponds to the permeability at point (i, j).

A.2 Near- to Far-Field Transformation

In chapter 3 the finite-difference time-domain method (FDTD) was used to characterize the near-field behavior of the grating coupler, used to vertically scatter the power incident from a W1-waveguide. However, in the experiments of chapter 4 it became apparent that a numerical far-field investigation would be necessary to validate the results achieved by back focal plane measurements (section 4.7). To attain such numerical results, it is not necessary to extend the computational domain to the far-field.

Instead, a phasor domain *near- to far-field transformation* (NTFF transformation) can be applied to calculate the complete radiation pattern of arbitrary structures *from the near-field data*. This scheme was firstly implemented into an FDTD algorithm by Umashankar and Taflove (1982) in two dimensions, by Taflove and Umashankar (1983) in three dimensions and is described in-depth in Taflove's book (Taflove and Hagness 2005). The following explanation is a summary based on the book.

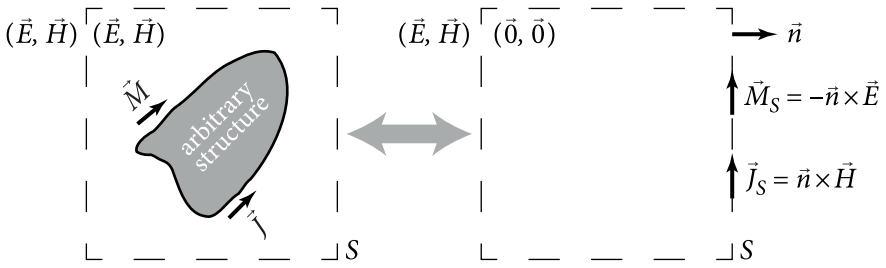

Figure A.1 | Illustration of the surface equivalence theorem. The real electric and magnetic currents $\vec{J}$ and $\vec{M}$ are replaced by equivalent electric and magnetic currents $\vec{J}_S$ and $\vec{M}_S$ on the box surface S, so that the fields $\vec{E}$ and $\vec{H}$ inside the box vanish and the ones outside are equal to the original fields.

Surface Equivalence Theorem

The fundamental idea is that any structure scattering electromagnetic radiation can be replaced by a closed box, radiating equivalent fields from the box surface S. This is known as *surface equivalence theorem*. The equivalent electric and magnetic currents $\vec{J}_S$ and $\vec{M}_S$ are chosen so that the fields inside the closed box vanish and the fields outside are equal to the ones formerly produced by the actual sources. The theorem is illustrated in figure A.1 and the equivalent current densities are given by

$$\vec{J}_S = \vec{n} \times \vec{H}, \tag{A.8}$$

$$\vec{M}_S = -\vec{n} \times \vec{E}. \tag{A.9}$$

Implementation in the FDTD-Method

As for flux monitors, described in the paragraph *Flux Monitors as an Effective Tool for the Computation of Transmission/Reflection Spectra* of section 2.2.3, the Fourier transform of the electric and magnetic fields $\widetilde{E}$ and $\widetilde{H}$ are computed on-the-fly, where $\sim$ denotes a vector in phasor domain. This is done on a rectangular closed box which completely surrounds the scatterer of interest, as illustrated in figure A.2.

Consequently, one yields the near-field electric and magnetic fields and can thus calculate the near-field equivalent electric and magnetic currents from equations (A.8) and (A.9), which also hold for phasor quantities. From these fields, one can calculate assistant fields $\widetilde{N}$ and $\widetilde{L}$ by integrating over the complete surface

$$\widetilde{N} = \iint_S \widetilde{J}_S e^{ikr' \cos\psi} \, ds', \tag{A.10}$$

$$\widetilde{L} = \iint_S \widetilde{M}_S e^{ikr' \cos\psi} \, ds', \tag{A.11}$$

where r' is the distance between observation point and equivalent source point on S. The angle ψ is measured between the vectors $\vec{r} = r\hat{e}_r$, pointing from the box center to the observation point, and $\vec{r}' = r'\hat{e}_{r'}$, which points from the equivalent source point on S to the observation point. The observation point is an arbitrary point in the far-field.

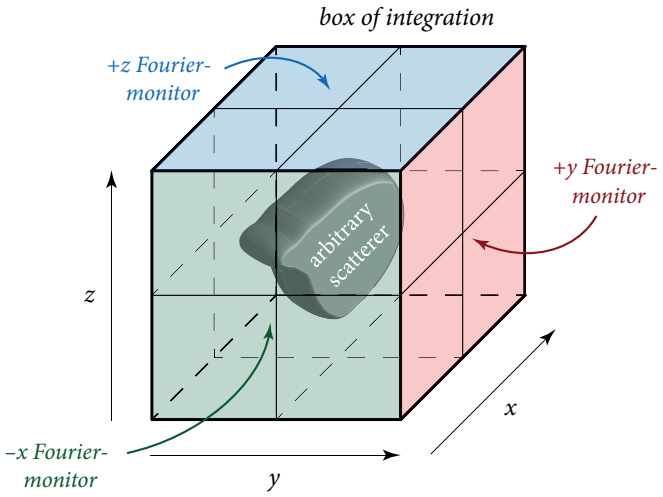

Figure A.2 | Sketch of the computational domain for near- to far-field transformation in FDTD. A closed box of Fourier-monitors, aligned with the Yee-grid, completely surrounds the scatterer. The allocated Fourier-transformed electric and magnetic fields $\widetilde{E}$ and $\widetilde{H}$ are used to compute the equivalent electric and magnetic currents $\widetilde{J}_S$ and $\widetilde{M}_S$.

Using the assistance fields (A.10) and (A.11), one can compute the electric and magnetic fields in the far field or the *bistatic radar cross section*, which is a standard measure for the radiation characteristic of an antenna or scatterer. The complete equations can again be found in the book of Taflove and Hagness (2005).

A.3 Cavity Quantum Electrodynamics

In view of the desire to find new areas of applications, the combination of photonic crystal cavities and two-level emitters is a promising field in order to build devices with novel capabilities. Apart from the fact that there are large barriers in the production of such systems, many groups have already shown possible new applications as well in simulations as in practice (Englund et al. 2007). It will be shown that one reason why photonic crystal resonators are an excellent choice for the production of cavity-quantum dot systems is the extremely small achievable mode volume, as has been in explained in 3.2.1. To understand the phenomena that are met inside such systems, a short introduction to cavity quantum electrodynamics (CQED) will be given. But before, two prominent examples for two-level emitters will be presented, which are *quantum dots* and *nitrogen-vacancy centers*.

A.3.1 Quantum Dots

Inside a metal or semiconductor free electrons are trapped in a specific region. For modern nano-structures, electrons are confined to areas of a few nanometers in each dimension. They can only escape from the structure by supplying a specific energy W, referred to as work of emission. If the electrons are trapped to a zero-dimensional potential, a *quantum dot* is formed: a portion of matter whose excitons are confined in all three spatial dimensions. An *exciton* is an electrically neutral bound quasiparticle consisting of an electron-hole pair. The energy distinction between the electron and the electron hole equates to the sum of their confinement energies and the band-gap.

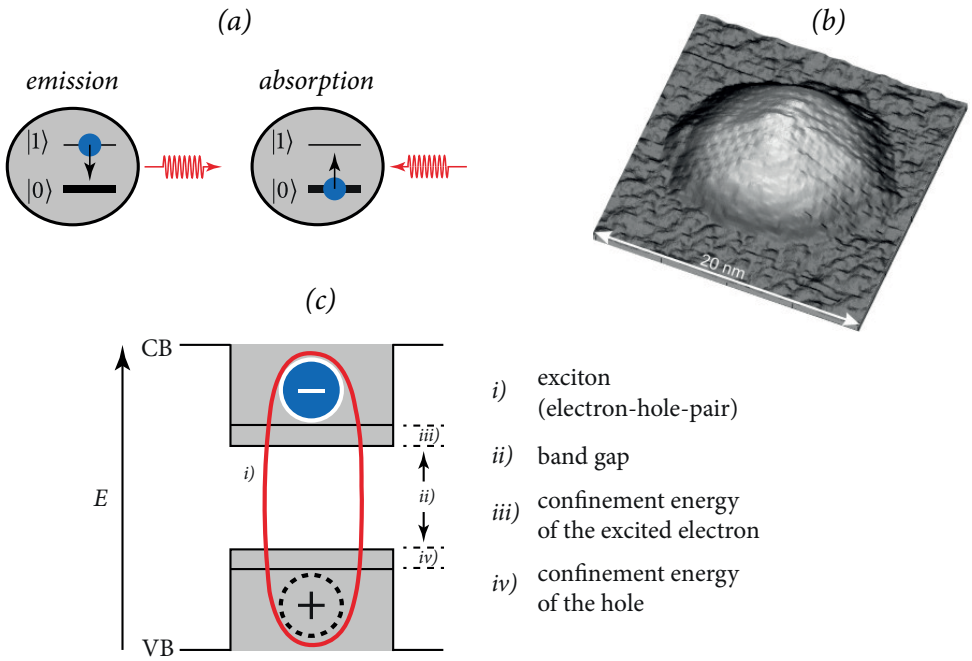

Figure A.3 | The quantum dot – an artificial atom. *(a)* Energy levels $|0\rangle$ and $|1\rangle$ of the quantum dot and the two possible interactions with light: emission and absorption of a single photon. *(b)* Top-view scanning tunneling microscope image of an InAs quantum dot on GaAs (Eisele et al. 2008). *(c)* Scheme of how a quantum dot is formed by a semiconductor, as it has a band gap between its valence and its conduction energy bands.

This strong localization leads to the *quantum confinement effect*. In a semiconductor, the excitons can be described by a Hamiltonian which is comparable to the one of hydrogen

$$\hat{\mathcal{H}} = -\frac{\hbar^2}{2m_h}\Delta_h - \frac{\hbar^2}{2m_e}\Delta_e - \frac{e^2}{\epsilon|r_e - r_h|}, \tag{A.12}$$

where m represents the effective mass, ϵ the dielectric constant of the semiconductor, Δ the Laplacian and the subscripts e and h denote the electron and the hole, respectively (compare to Novotny and Hecht 2012). In semiconductors the Bohr radius of the excitons can be smaller than 10 nm, caused by the very small effective masses of the electrons and holes. Thereafter, the quantum confinement effect becomes important for length scales much larger than the size of atoms or molecules. For small particles the Coulomb potential is strongly screened and so the last term in equation (A.12) can be neglected. Consequently, the electron and the hole can be described by a potential-well model leading to discrete energy levels where the energies increase if the dimensions of the well decrease. The result is an object whose optical properties are *highly tunable* and therefore is perfectly suited to be used as an emitter/absorber inside a photonic crystal nanocavity.

Figure A.3 gives an overview about the important qualities of quantum dots. Figure A.3*(a)* illustrates the quantum dot modeled as a two-level system. The only two possible interactions of the quantum dot with light are the emission and the absorption of a single

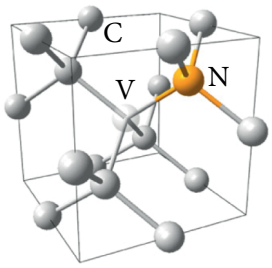

Figure A.4 | The nitrogen-vacancy center. The crystallographic structure reveals a missing carbon atom and a substitutional nitrogen atom (taken from Aharonovich et al. 2011).

photon having the same energy as the separation of the two levels. Figure A.3*(b)* shows a scanning tunneling microscope (STM) image of a fabricated InAs quantum dot on GaAs and Figure A.3*(c)* depicts how the quantum dot is formed from the band-gap between the conduction and the valence band of a semiconductor.

A.3.2 Nitrogen-Vacancy Centers

A second important candidate for a quasi two-level system which can be used as quantum emitter is the *nitrogen-vacancy (NV) center in nanodiamonds*. Nanodiamonds are diamond crystals with only a few nanometers in size, which can be produced on an industrial scale (Wolters 2013). Impurities formed by non-carbon atoms in the diamond lattice lead to *defect centers*, of which more than 100 are known to be luminescent (Barth 2010). The most frequently met defect is the nitrogen-vacancy center, formed from a missing carbon atom and a substitutional nitrogen atom (figure A.4). The defect introduces new energy levels which can be stimulated for optical transitions.

Such nanocrystals can be isolated and brought into a photonic crystal cavity (Wolters et al. 2010), for example using an atomic force cantilever for manipulation (Schell et al. 2011). Once the problems with the instability of the optical transition line (Wolters et al. 2013) are solved, it will be suitable for quantum information processing devices like the on-chip Hong-Ou-Mandel experiment, as described in the introduction (chapter 1).

A.3.3 Cavity Quantum Electrodynamics (CQED)

The most important system described by cavity quantum electrodynamics is a single two-level dipole emitter coupled to the electromagnetic field of a single mode of an optical resonator. Such systems can be described theoretically using the Jaynes-Cummings model. The dipole emitter can exclusively occupy two distinct energy levels $|0\rangle$ and $|1\rangle$, while the cavity itself can contain a large number of photons, which characterize its energy levels. Within the dipole and rotating wave approximation, the Jaynes-Cummings-Hamiltonian

$$\hat{\mathcal{H}} = \underbrace{\hbar\omega_r\left(\hat{a}^\dagger\hat{a} + \tfrac{1}{2}\right)}_{\text{cavity}} + \underbrace{\frac{\hbar\omega_a}{2}\hat{\sigma}_z}_{\text{dipole}} + \underbrace{\hbar g\left(\hat{a}^\dagger\hat{\sigma}_- + \hat{\sigma}_+\hat{a}\right)}_{\text{interaction}} \tag{A.13}$$

consists of three terms representing the quantized fields inside the cavity, the 2-level system of the dipole and the interaction of both systems. ω_r denotes the frequency of the single

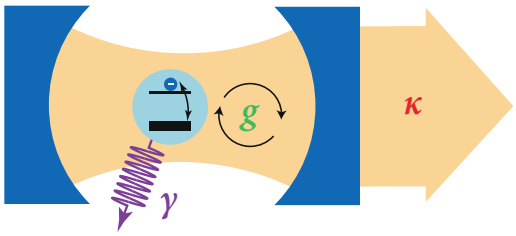

Figure A.5 | Basic scheme of a CQED-system. A two-level system is situated inside a Fabry-Perot cavity. It is coupled via the photon Rabi frequency g to a single cavity mode (orange pattern inside the resonator), but also emits photons to external modes with rate γ. The cavity emits photons through its end mirror at rate κ. Strong coupling is met if $g > \kappa, \gamma$.

mode inside the cavity, $\hat{a}^\dagger$ and $\hat{a}$ are the creation and annihilation operators for photons of that frequency. The two-level system is equivalent to a spin-half system whose state can be described using a three-dimensional Bloch vector. The energy separation between the two states $|0\rangle$ and $|1\rangle$ is given by $\hbar\omega_a$, where ω_a is referred to as atomic transition frequency. The Pauli-σ-operators can be written as

$$\hat{\sigma}_z = |1\rangle\langle 1| - |0\rangle\langle 0|, \qquad \hat{\sigma}_+ = |1\rangle\langle 0|, \qquad \hat{\sigma}_- = |0\rangle\langle 1| \tag{A.14}$$

and are called atomic inversion operator and raising and lowering operators, respectively. $\hat{\sigma}_+$ and $\hat{\sigma}_-$ generate the coupling of the two-level system to the electromagnetic field of the cavity mode. Figure A.5 visualizes the interactions inside a CQED-system.

The coupling constant g is called *single photon Rabi frequency* ($2g$ is the *vaccum Rabi splitting*) and has a spatial dependence

$$g(\vec{r}) = \left(\frac{\mu^2\omega_r}{2\hbar\epsilon_0 V}\right)^{1/2} U(\vec{r}) = g_0 U(\vec{r}). \tag{A.15}$$

In this equation $U(\vec{r})$ is a cavity standing wave mode function, μ the dipole moment of the two-level system and $V = \int |U(\vec{r})|^2 \, \mathrm{d}^3 r$ the modal volume of the cavity (compare to Walls and Milburn 2008). Neglecting the spatial dependence, one directly recognizes the relation between the modal volume V and the Rabi frequency g: smaller modal volume leads to larger values of g.

Since the strong coupling regime is met if

$$g > \kappa, \gamma, \quad \text{(strong coupling regime)} \tag{A.16}$$

one has to decrease the losses and increase g. Here, γ is the rate with which the two-level system emits photons to external modes and κ is the rate with which photons leak through the end mirror. As has been shown, a large g corresponds to a small modal volume and so photonic crystal cavities – due to their very small modal volume – are in fact a prominent candidate for the production of strongly coupled CQED-systems. A suitable choice for the dipole would be a single atom, but its placement inside the cavity is a rather complicated task. The positioning of quantum dots or NV centers is easier to manage and they are more stable at their location. Consequently, the combination of photonic crystal cavities and quantum dots or NV centers is a good choice to build such systems.

A.4 Thickness Determination by X-Ray Reflectivity Measurements

For the numerical modeling of photonic crystals as a comparison for real measurements, it is important to know as much fixed parameters as possible. Since for the production ready-to-use wafers composed of three layers are utilized, an investigation of their actual layer thicknesses appeared reasonable (section 4.1.1, figure 4.2). Additionally, during the underetching process the hydrofluoric acid affects the overall thickness of the Si_3N_4-layer and thus the thickness of the photonic crystal slab.

For the thickness determination the method of X-ray reflectivity measurements was used, kindly carried into execution by C. Weber and Professor S. Kowarik (HU Berlin) at the facilities of the ESRF in Grenoble. In this method, X-rays are directed onto the surface of interest under a number of angles. The intensity of the reflected rays in the specular direction is detected, providing information about the thicknesses, surface roughnesses and electron densities of the involved layers. For the computational analysis the Parratt

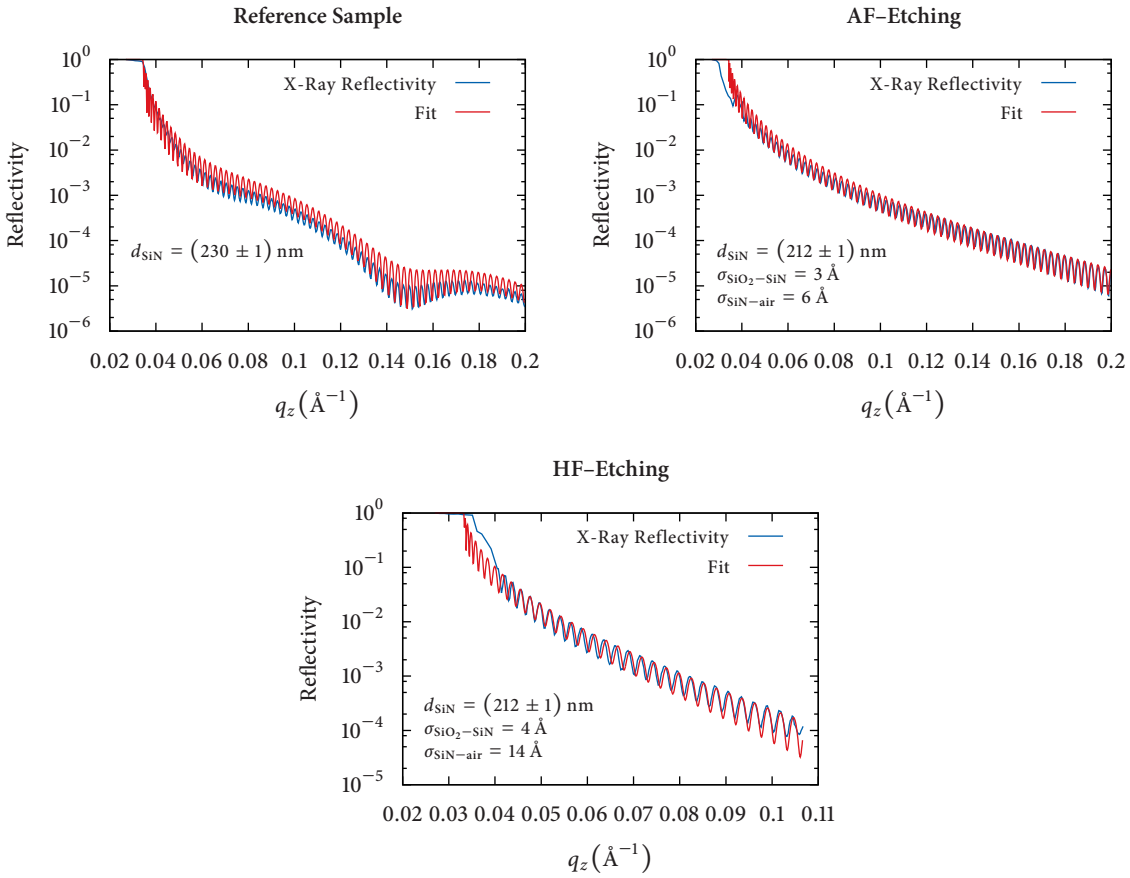

Figure A.6 | Results of the X-ray reflectivity measurements. Measurement (blue) and fit curves (red) for the X-ray investigation. Computed layer thickness d and surface roughnesses σ are given in the plots. The AF process produces better results for the roughness of the SiN-air interface. *Thanks to C. Weber and Prof. S. Kowarik (HU Berlin) for performing the measurements at the synchrotron of ESRF (Grenoble).*

algorithm (Parratt 1954) is used, for which a layer model has to be provided.

Three different samples have been studied this way: (i) a reference sample, which is a wafer composed as in figure 4.2(a) without resist; (ii) an identical wafer after etching with diluted hydrofluoric acid (AF) and (iii) another one etched using hydrofluoric acid (HF). The evaluated data, as well provided by C. Weber et al., is depicted in figure A.6. The three plots show a great agreement between measurement (blue) and fit model (red). For the reference sample a SiN layer thickness of $d_{\mathrm{SiN}} = 230 \pm 1\,\mathrm{nm}$ was found, equaling the manufacturer information. The two different etching processes both produce a final layer thickness of $d_{\mathrm{SiN}} = 212 \pm 1\,\mathrm{nm}$ – accordingly this value was used for the FDTD simulations. Additionally, using the known etching times the etching rates can be computed from these results. The AF-process produces a smoother surface, represented by the more than doubled roughness $\sigma_{\mathrm{SiN-air}}$ of the SiN–air interface for the HF case. Consequently, the AF-process is preferable.

Acknowledgements

It is a fact, that scientific work can never be assessed without the knowledge about its *background*. Unfortunately, the word background in this case is most often interpreted as *historical* background. Einstein would not have been able to find the theory of relativity in the middle ages, understandably. But what is mostly forgotten is, that he possibly would also not have been able without the support of his family or people of his surroundings. In fact, it is even still controversial how much his first wife Mileva Marić contributed to his success.

Besides philosophical considerations, many people contributed to this thesis as well. Primarily, I would like to thank my supervisor Professor Dr. Oliver Benson for leaving me the freedom to work in my own way and my tutor Janik Wolters, of which's knowledge and advice this thesis largely benefited. Of course – not to forget – I want to thank Professor Dr. Kurt Busch for being willing to act as the second referee.

Moreover, I would like to express my gratitude to all members of my family – including the family of my beloved girlfriend Yvonne – which showed tremendous patience and gave constant support in all possible ways. Most important, I want to thank Yvonne who assisted me over the entire time with all of her power, time, love and cookies.

Lastly, many people supported me with discussions or instructions at the Humboldt Universität zu Berlin or at BESSY. I would like to emphasize the contribution of Jürgen Probst, who inducted me to the production of photonic crystals and gave a lot of his personal time to work on simulations or other programs important for this work. To name just a few more, I want to thank Max Schöngen, Andreas Schell, Günter Kewes, Nikola Sadzak, Sten Wenzel, Martin Handwerg, Daniel Wetzel and Steven Wilson.

References

Aharonovich, I., Castelletto, S., Simpson, D. A., Su, C.-H., Greentree, A. D. and Prawer, S.: 2011, Diamond-based single-photon emitters, *Reports on Progress in Physics* **74**(7), 076501.

Akahane, Y., Asano, T. and Song, B.: 2003, High-Q photonic nanocavity in a two-dimensional photonic crystal, *Nature* **425**(October), 4–7.

Arcari, M., Javadi, A., Hansen, S. L., Mahmoodian, S., Liu, J., Thyrrestrup, H., Lee, E. H., Song, J. D. and Lodahl, P.: 2014, Near-unity coupling efficiency of a quantum emitter to a photonic-crystal waveguide, *Arxiv preprint arXiv:1402.2081v1* pp. 1–13.

Arnoldi, W. E.: 1951, The principle of minimized iterations in the solution of the matrix eigenvalue problem, *Quart. Appl. Math* **9**(1), 17–29.

Asakawa, K., Sugimoto, Y., Watanabe, Y., Ozaki, N., Mizutani, A., Takata, Y., Kitagawa, Y., Ishikawa, H., Ikeda, N., Awazu, K., Wang, X., Watanabe, A., Nakamura, S., Ohkouchi, S., Inoue, K., Kristensen, M., Sigmund, O., Borel, P. I. and Baets, R.: 2006, Photonic crystal and quantum dot technologies for all-optical switch and logic device, *New Journal of Physics* **8**(9), 208–208.

Ashcroft, N. W. and Mermin, N. D.: 1976, *Solid State Physics*, college edn, Harcourt College Publishers.

Barth, M.: 2010, *Hybrid nanophotonic elements and sensing devices based on photonic crystal structures*, Phd thesis, Humboldt-Universitaet zu Berlin.

Benson, O.: 2011, Assembly of hybrid photonic architectures from nanophotonic constituents., *Nature* **480**(7376), 193–9.

Benson, O., Santori, C., Pelton, M. and Yamamoto, Y.: 2000, Regulated and entangled photons from a single quantum Dot, *Physical review letters* **84**(11), 2513–6.

Berenger, J.-P.: 1994, A perfectly matched layer for the absorption of electromagnetic waves, *Journal of Computational Physics* **114**(2), 185–200.

Chalcraft, a. R. a., Lam, S., O'Brien, D., Krauss, T. F., Sahin, M., Szymanski, D., Sanvitto, D., Oulton, R., Skolnick, M. S., Fox, a. M., Others, O'Brien, D., Whittaker, D. M., Liu, H.-Y. and Hopkinson, M.: 2007, Mode structure of the L3 photonic crystal cavity, *Applied Physics Letters* **90**(24), 241117.

Demtröder, W.: 2009, *Experimentalphysik 2*, Springer-Lehrbuch, 5th edn, Springer Berlin Heidelberg, Berlin, Heidelberg.

Dongarra, J.: 2013, Visit to the National University for Defense Technology Changsha, China, *Technical report*, University of Tennessee.

Ehrenfest, P.: 1927, Bemerkung ueber die angenaeherte Gueltigkeit der klassischen Mechanik innerhalb der Quantenmechanik, *Zeitschrift fuer Physik* **45**(7-8), 455–457.

Eisele, H., Lenz, A., Heitz, R., Timm, R., Daehne, M., Temko, Y., Suzuki, T. and Jacobi, K.: 2008, Change of InAs/GaAs quantum dot shape and composition during capping, *Journal of Applied Physics* **104**(12), 124301.

Englund, D., Faraon, A., Fushman, I., Stoltz, N., Petroff, P. and Vuckovic, J.: 2007, Controlling cavity reflectivity with a single quantum dot., *Nature* **450**(7171), 857–61.

Faraon, A., Fushman, I. and Englund, D.: 2008, Dipole induced transparency in waveguide coupled photonic crystal cavities, *IEEE Lasers and* **16**(16), 944–947.

Faraon, A., Majumdar, A., Englund, D., Kim, E., Bajcsy, M. and Vuckovic, J.: 2011, Integrated quantum optical networks based on quantum dots and photonic crystals, *New Journal of Physics* **13**(5), 055025.

Faraon, A., Waks, E., Englund, D., Fushman, I. and Vuckovic, J.: 2007, Efficient photonic crystal cavity-waveguide couplers, *Applied Physics Letters* **90**(7), 073102.

Farjadpour, a., Roundy, D., Rodriguez, A., Ibanescu, M., Bermel, P., Joannopoulos, J. D., Johnson, S. G. and Burr, G. W.: 2006, Improving accuracy by subpixel smoothing in the finite-difference time domain, *Optics Letters* **31**(20), 2972.

García, P., Sapienza, R., Froufe-Pérez, L. and López, C.: 2009, Strong dispersive effects in the light-scattering mean free path in photonic gaps, *Physical Review B* **79**(24), 241109.

Gedney, S. D.: 2011, *Introduction to the Finite-Difference Time-Domain (FDTD) Method for Electromagnetics*, Vol. 6, Morgan and Claypool.

Hecht, E.: 2002, *Optics*, 4th edn, Addison-Wesley.

Hong, C. K., Ou, Z. Y. and Mandel, L.: 1987, Measurement of subpicosecond time intervals between two photons by interference, *Physical Review Letters* **59**(18), 2044–2046.

Hu, J. and Menyuk, C. R.: 2009, Understanding leaky modes: slab waveguide revisited, *Advances in Optics and Photonics* **1**(1), 58.

Jackson, J. D.: 1998, *Classical Electrodynamics*, 3. edn, John Wiley & Sons, New York.

Joannopoulos, J. D., Johnson, S. G., Winn, J. N. and Meade, R. D.: 2008, *Photonic crystals: molding the flow of light*, Vol. 2, 2. edition edn, Princeton University Press.

Joannopoulos, J. D. and Villeneuve, P.: 1997, Photonic crystals: putting a new twist on light, *Nature* .

John, S. and Busch, K.: 1999, Photonic Bandgap Formation and Tunability in Certain Self-Organizing Systems, **17**(11), 1931–1943.

Johnson, S. G. and Joannopoulos, J. D.: 2001, Block-iterative frequency-domain methods for Maxwell's equations in a planewave basis, *Opt. Express* **8**(3), 363–376.

Johnson, S. G., Villeneuve, P. R., Fan, S. and Joannopoulos, J. D.: 2000, Linear waveguides in photonic-crystal slabs, *Phys. Rev. B* **62**(12), 8212–8222.

Kappeler, R., Kaspar, P. and Jäckel, H.: 2011, Propagation loss computation of W1 photonic crystal waveguides using the cutback technique with the 3D-FDTD method, *Photonics and Nanostructures- ...* **9**, 235–247.

Kappeler, R., Kaspar, P., Jaeckel, H. and Hafner, C.: 2012, Record-low propagation losses of 154 dB/cm for substrate-type W1 photonic crystal waveguides by means of hole shape engineering, *Applied Physics Letters* **101**(13), 131108.

Kouba, J.: 2008, *Investigation of silicon nitride based two-dimensional photonic crystals for the visible spectral range*, Phd thesis, Technische Universitaet Berlin.

Kuramochi, E., Notomi, M., Mitsugi, S., Shinya, A., Tanabe, T. and Watanabe, T.: 2006, Ultrahigh-Q photonic crystal nanocavities realized by the local width modulation of a line defect, *Applied Physics Letters* **88**(4), 041112.

Lodahl, P., Floris Van Driel, a., Nikolaev, I. S., Irman, A., Overgaag, K., Vanmaekelbergh, D. and Vos, W. L.: 2004, Controlling the dynamics of spontaneous emission from quantum dots by photonic crystals., *Nature* **430**(7000), 654–7.

Mandelshtam, V. A. and Taylor, H. S.: 1997, Harmonic inversion of time signals and its applications, *The Journal of chemical physics* **107**, 6756.

Moore, G.: 1965, Cramming More Components Onto Integrated Circuits, *Electronics* **38**(8), 114–117.

Novotny, L. and Hecht, B.: 2012, Quantum emitters, *Principles of nano-optics*, 2nd edn, Cambridge University Press, pp. 282–312.

Nüsse, N. C.: 2011, *Hybridstrukturen aus Nanodiamanten, nanoplasmonischen Elementen und photonischen Kristallen*, PhD thesis.

O'Brien, J. L., Furusawa, A. and Vuckovic, J.: 2009, Photonic quantum technologies, *Nature Photonics* **3**(12), 687–695.

Oskooi, A. F., Roundy, D., Ibanescu, M., Bermel, P., Joannopoulos, J. D. and Johnson, S. G.: 2010, Meep: A flexible free-software package for electromagnetic simulations by the FDTD method, *Computer Physics Communications* **181**(3), 687–702.

Parratt, L.: 1954, Surface Studies of Solids by Total Reflection of X-Rays, *Physical Review* **95**(2), 359–369.

Purcell, E. M.: 1946, Spontaneous emission probabilities at radio frequencies, *Physical Review* **69**, 681.

Reithmaier, G., Lichtmannecker, S., Reichert, T., Hasch, P., Müller, K., Bichler, M., Gross, R. and Finley, J. J.: 2013, On-chip time resolved detection of quantum dot emission using integrated superconducting single photon detectors., *Scientific reports* **3**, 1901.

Russell, P.: 2003, Photonic crystal fibers., *Science (New York, N.Y.)* **299**(5605), 358–62.

Sakurai, J. J. and Napolitano, J.: 2011, *Modern Quantum Mechanics*, 2nd edn, Addison-Wesley, San Francisco.

Saleh, B. E. A. and Teich, M. C.: 2007, *Fundamentals of Photonics*, Wiley Series in Pure and Applied Optics, 2nd edn, John Wiley & Sons, Inc., New York, USA.

Sapienza, R., Coenen, T., Renger, J., Kuttge, M., van Hulst, N. F. and Polman, A.: 2012, Deep-subwavelength imaging of the modal dispersion of light., *Nature materials* **11**(9), 781–7.

Schell, A. W., Kewes, G., Schroeder, T., Wolters, J., Aichele, T. and Benson, O.: 2011, A scanning probe-based pick-and-place procedure for assembly of integrated quantum optical hybrid devices., *The Review of scientific instruments* **82**(7), 073709.

Song, B.-S., Noda, S., Asano, T. and Akahane, Y.: 2005, Ultra-high-Q photonic double-heterostructure nanocavity, *Nature Materials* **4**(3), 207–210.

Taflove, A.: 1980, Application of the Finite-Difference Time-Domain Method to Sinusoidal Steady-State Electromagnetic-Penetration Problems, *IEEE Transactions on Electromagnetic Compatibility* **EMC-22**(3), 191–202.

Taflove, A. and Hagness, S. C.: 2005, *Computational electrodynamics: the finite-difference time-domain method.*, 3rd edn, Artech House.

Taflove, A. and Umashankar, K.: 1983, Radar cross section of general three-dimensional scatterers, *Electromagnetic Compatibility, IEEE ...* .

Tong, L., Gattass, R. R., Ashcom, J. B., He, S., Lou, J., Shen, M., Maxwell, I. and Mazur, E.: 2003, Subwavelength-diameter silica wires for low-loss optical wave guiding., *Nature* **426**(6968), 816–9.

Umashankar, K. and Taflove, A.: 1982, A novel method to analyze electromagnetic scattering of complex objects, *Electromagnetic Compatibility, IEEE ...* .

Vahala, K. J.: 2003, Optical microcavities., *Nature* **424**(6950), 839–46.

Walls, D. F. and Milburn, G. J.: 2008, CQED, *Quantum Optics*, 2nd edn, Springer, Berlin Heidelberg, chapter 11, pp. 213–229.

Wolff, C.: 2011, *Band Structure Based Analysis of Certain Photonic Crystal Structures*, Phd thesis, Karlsruher Institut fure Technologie (KIT).

Wolters, J.: 2013, *Quantum Hybrid Systems*, PhD thesis, Humboldt-Universität zu Berlin.

Wolters, J., Sadzak, N., Schell, A., Schroeder, T. and Benson, O.: 2013, Measurement of the Ultrafast Spectral Diffusion of the Optical Transition of Nitrogen Vacancy Centers in Nano-Size Diamond Using Correlation Interferometry, *Physical Review Letters* **110**(2).

Wolters, J., Schell, A. W., Kewes, G., Nuesse, N., Schoengen, M., Doescher, H., Hannappel, T., Loechel, B., Barth, M. and Benson, O.: 2010, Enhancement of the zero phonon line emission from a single nitrogen vacancy center in a nanodiamond via coupling to a photonic crystal cavity, *Applied Physics Letters* **97**(14), 141108.

Yablonovitch, E.: 1987, Inhibited spontaneous emission in solid-state physics and electronics, *Physical review letters* .

Yablonovitch, E.: 1992, *Confined Electrons and Photons*, Vol. 340 of *NATO ASI Series*, Springer US, Boston, MA.

Yee, K.: 1966, Numerical solution of initial boundary value problems involving maxwell's equations in isotropic media, *IEEE Transactions on Antennas and Propagation* **14**(3), 302–307.

Own Contributions

Conference Poster

Barth, C., Adler, M., Probst, J., Schoengen, M., Loechel, B., Wolters, J., Benson, O.: 2013, Design and Optimization and Fabrication of Photonic Crystal Structures for Single Photon Applications, *DPG Spring Meeting*, Regensburg.

Eigenständigkeitserklärung

Hiermit versichere ich, dass ich die vorliegende Arbeit selbständig verfasst und keine anderen als die angegebenen Quellen und Hilfsmittel verwendet habe.

Berlin, den 20. Februar 2014 Carlo Barth